STIMULUS-INDUCED WAVES AND BREATHERS IN SYNAPTICALLY-COUPLED NEURAL NETWORKS

Stefanos Efthymios Folias

A dissertation submitted to the faculty of

The University of Utah
in partial fulfillment of the requirements for the degree of

Doctor of Philosophy

Department of Mathematics The University of Utah

May 2005

ABSTRACT

Traveling waves and stationary bumps are spatiotemporal structures of activity that have been verified experimentally to exist in different cortical regions of the brain. Activity is characterized by the output firing rate of spikes of the neuronal population and is often described mathematically by neural network firing rate models. Neurons are coupled in a nonlocal fashion generating a system of spatially-extended, nonlinear integrodifferential equations, in which the integral kernel represents the spatial distribution of synaptic connections. Such equations, in the absence of an input, support stationary and traveling waves similar to those found in the real cortex. We build upon previous work by analyzing the effect of stationary and traveling persistent inputs on an excitatory neural network model with local inhibition that represents disinhibited cortical tissue slices. For weak local inhibition and a smooth firing rate function, we show that the system supports traveling fronts, exhibiting a front bifurcation analogous to that found in reaction-diffusion equations. Furthermore, a weak, stationary input inhomogeneity can induce a Hopf bifurcation of the front leading to an oscillatory front. Using a Heaviside firing rate function, we study the response of the system to strong inputs. In particular, the activity of the system can lock to a unimodal input to form a localized bump of activity, traveling with the speed of the input. As the strength of the input is reduced, or the velocity varied appropriately, the bump loses stability, undergoing a Hopf bifurcation to a stable, spatially-localized oscillation or breather. If the network supports traveling pulses in the absence of an input, a further reduction of the input induces a secondary instability leading to a breather which periodically emits traveling pulses. These results form testable predictions for disinhibited cortical slice experiments. The theory is also extended to two-dimensional networks for radially symmetric, stationary inputs; while the excitatory weight function parallels the one-dimensional case with radially symmetric pulses and breathers, it is found that a Mexican hat weight function generates asymmetric breathers due to the higher order spatial modes of the linearization that dominate the instability.

For my parents, who taught me to believe in myself.

CONTENTS

NO	OTATION AND SYMBOLS	vii
1.	INTRODUCTION	1
	1.1 Activity Bumps and Waves in Neural Populations	2
	1.1.1 Experimental Background	$\frac{1}{2}$
	1.1.2 Theoretical Background	9
	1.2 Content of Dissertation	15
2.	BIOPHYSICS AND MATHEMATICAL MODELS	23
	2.1 Anatomy and Physiology	23
	2.2 Mathematical Models: Cellular Level	26
	2.2.1 Membrane and Ion Channels	26
	2.2.2 Synapses	30
	2.2.3 Axons and Dendrites	33
	2.3 Mathematical Models: Systems Level	34
	2.3.1 Biophysical Models	34
	2.3.2 Integrate-and-Fire Population Model	38
	2.3.3 Rate Models	39
3.	ON FRONT BIFURCATIONS	
	IN AN EXCITATORY NEURAL NETWORK	43
	3.1 Fronts in a Homogeneous Network	45
	3.2 Front Bifurcation	47
	3.3 The Effect of a Weak Input Inhomogeneity	51
	3.4 Exactly Solvable Model	54
	3.4.1 Traveling Fronts (Homogeneous Case)	55
	3.4.2 Stability Analysis of Stationary Fronts	58
	3.4.3 Hopf Bifurcation to a Breathing Front	59
	3.4.4 Locking to a Moving Input	63
	3.5 Discussion	66

4.	BREATHERS IN ONE-DIMENSIONAL NETWORKS	69
	4.1 Stationary Pulses in an Inhomogeneous Network	70
	4.1.1 Stationary Pulse Existence	70
	4.1.2 Stability Analysis	73
	4.2 Numerical Results	77
	4.2.1 Hopf Bifurcation to a Breather	77
	4.2.2 Breathers in a Biophysical Model	83
	4.3 Discussion	86
5 .	BREATHERS IN TWO-DIMENSIONAL NETWORKS	89
	5.1 Two-dimensional pulses	89
	5.1.1 Stationary Pulse Existence	89
	5.1.2 General, Positive Synaptic Weight Distribution	90
	5.1.3 Exponential Weight Distribution	92
	5.1.4 Positive Modified Bessel Weight Distribution	95
	5.1.5 Mexican Hat Weight Function	96
	5.2 Stability Analysis	98
	5.2.1 Spectral Analysis of the Linearized Operator	98
	, , ,	101
	1 0	104
	8	106
		109
	1	109
		110
	5.4 Discussion	114
6.	STIMULUS-LOCKED TRAVELING WAVES AND	
	BREATHERS IN AN EXCITATORY NETWORK 1	
	6.1 Stimulus-Locked Traveling Fronts in a Scalar Equation	
		118
	6.1.2 Stability of Stimulus-Locked Fronts	
	6.2 Stimulus-Locked Traveling Pulses in a Vector System	
	6.2.1 Existence of Stimulus-Locked Pulses	
	6.2.2 Pulses for an Exponential Weight Distribution	
	į.	133
	1	133
	6.3.2 Evans Function for Stimulus-Locked Traveling Pulses	
	6.3.3 Numerical Simulations	140

	6.4 Discussion	. 142
7.	FUTURE DIRECTIONS	145
AP	PENDICES	
A.	PARAMETERS FOR THE BIOPHYSICAL MODEL	149
В.	AMARI'S ANALYSIS	150
\mathbf{RE}	FERENCES	155

NOTATION AND SYMBOLS

\mathbb{R}^n	<i>n</i> -dimensional Euclidean space
\mathbb{C}^n	n-dimensional complex Euclidean space
$\mathcal{C}^n(\mathbb{R},\mathbb{R})$	Bounded, n-times continuously differentiable functions $f: \mathbb{R} \longrightarrow \mathbb{R}$
$\mathcal{C}^n(\mathbb{R},\mathbb{C})$	Bounded, n-times continuously differentiable functions $f: \mathbb{R} \longrightarrow \mathbb{C}$
$\mathcal{L}^2(\mathbb{R})$	Lebesgue square integrable functions $f: \mathbb{R} \longrightarrow \mathbb{R}$
$\Re e(\lambda)$	Real part of λ
$\Im m(\lambda)$	Imaginary part of λ
Н	Standard Heaviside function
$reve{w}$	Hankel transform of the function w
$J_{ u}$	Bessel function of the first kind of order ν
$I_{ u}$	Modified Bessel function of the first kind of order ν
$K_{ u}$	Modified Bessel function of the second kind of order ν
$\mathbf{L}_{ u}$	Modified Struve function of order ν
exp	Exponential function e^x
erfc	Complementary error function
sgn	Signum function
\mathbf{r}	Two-dimensional spatial vector set in polar coordinates (r,θ)
u * v	Convolution of u and v
$\Upsilon \equiv \Psi$	Y is defined by Y

ACKNOWLEDGMENTS

I deeply thank my advisor Paul C. Bressloff for the guidance and motivation he offered, for the many, often lengthy, impromptu discussions we shared developing the ideas herein and, moreover, for helping me find precisely the type of mathematical neuroscience I had dreamed of studying 10 years earlier. I also thank James P. Keener and Paul C. Fife for many helpful discussions concerning this work, as well as their previous courses, discussions, and group meetings, all of which have greatly shaped my perspective and understanding of mathematics.

CHAPTER 1

INTRODUCTION

The brain is arguably one of the most complicated objects in nature to study and understand. Consequently, one expects any such model, be it a theoretical word model or a mathematical model, to be highly oversimplified and, thus, not representative of the brain itself or any parts thereof. Of course, with this attitude surely no progress would be made. While much is understood biologically and mathematically about the generation of neuronal spikes—large short-term fluctuations of the transmembrane electric potential believed to be the medium of neural communication—it is quite a daunting task to couple neurons together and understand their collective behavior. One of the primary goals of neuroscience is to understand the collective behavior of neurons: how does each neuron contribute to the network, what are the emergent properties of the interconnection, and, ultimately, how do such properties lead to brain function?

One method to accomplish this is to generate mathematical models, describing the biophysics of individual neurons, their connections, and the dynamics they obey, and allow the behavior to unfold by means of approximation and computer simulation. One of the fundamental issues with this method is that the increasing complexity of the model leads to an increasing difficultly in interpretation of the results. Another approach constitutes using mathematical analysis of highly simplified, yet analytically tractable mathematical models to make more definitive statements about the mathematical structure underlying the behavior of the model. Such definitive statements, potentially, can be related to the biology to describe one or more of the dominant features of the system. Contrary to the field of fluid dynamics and its Navier-Stokes equations, the field of mathematical neuroscience, or neurophysics, currently has not agreed upon one or even a small collection of models satisfactory enough to constitute the "brain equations." This is partly due to the immaturity of the field but is largely due to the incredibly complex and diverse types and networks of neurons, which are compounded by intricate connections that can change on fast and slow time-scales. Thus, it is an exciting time to develop

and analyze models and determine testable predictions which, when compared with experimental results, can determine which models are useful, why they are useful, and what they are lacking. Regardless of the final judgment, many of the models that describe networks of neurons generate dynamical systems that exhibit rich behavior and are, thus, interesting purely from a mathematical point of view. In this dissertation we shall study the effect of current inputs into a simplified, spatially-extended, continuum model of one- and two-dimensional, cortical tissue in the form of nonlinear, integrodifferential equations describing the evolution of the average activity of the neurons, coupled synaptically in a manner that is dependent on the distance between neurons. Such equations are infinite-dimensional dynamical systems and are amenable to the use of bifurcation theory, perturbation theory, and other techniques of applied mathematics, in order to characterize the different states of behavior and their associated transitions. In particular, we shall study the existence, stability, and bifurcations of stationary and traveling waves, which are induced by stationary and moving stimulus inputs to the neural medium.

1.1 Activity Bumps and Waves in Neural Populations

1.1.1 Experimental Background

There is increasing experimental evidence supporting the existence of spatiotemporal structures in the brain, specifically in the cortex, as technology overcomes the difficulty in experimentation over spatial domains [96, 35, 25]. Recent experimental work has enabled neuroscientists to look at spatially distributed connections, confirming that spatial structure is an important feature. It is surely reasonable to expect spatial structure to play a role in the processing of visual information that is conducted by many different brain regions. For example, the prefrontal cortex is a cortical region found to be involved in complex problem solving and planning future actions, suggesting that these tasks require short term, or working memory [67]. In delay response tasks, primates are trained to remember the spatial location of a sensory cue, e.g., a food reward. Physiological experiments show that, during the period when the primate is remembering, spatially localized groups of neurons continuously fire, either until the task is finished or until enough time has passed that the activity has degraded [35, 75, 2]. Moreover, there is a correspondence between the spatial location of the visual stimulus and the localized group of active neurons, indicating that a spatial map of the visual field may be encoded in the firing patterns of the network of neurons. Such a map changes in time so that at two different experimental sessions, the same stimulus and location may correspond

to different groups of neurons, yet the result of remembering the correct spatial location is achieved. In the simplest case, one can think of such behavior, mathematically, as a bump, that is, a stable, unimodal stationary solution of a system of equations; an initial localized disturbance of the system, perhaps due to a transient input, initiates the bump, which is subsequently sustained by the system. The next step is to understand multiple bump solutions, as well as suprathreshold solutions with more complicated geometries. As the solution becomes more complex, numerical solutions may be more appropriate for studying the existence of such solutions; however, it seems possible that basic principles, uncovered from studying simpler solutions, may serve to guide one's understanding of the irregularly shaped solutions that are more likely to be seen in the cortex.

Another class of spatiotemporal structures found in the cortex are traveling waves of electrical activity. Such waves have been observed in vivo in the somatosensory cortex of behaving rats [79], turtle and mollusk olfactory bulbs [60, 65], turtle cortex [85] and visuomotor cortices in cat [90]. Often these traveling waves occur during periods without sensory stimulation, with a subsequent presentation of a stimulus inducing a switch to synchronous oscillatory behavior [25]. This suggests that determining the conditions under which cortical wave propagation can occur is important for understanding the normal processing of sensory stimuli. Although there is no extensive evidence for waves thus far, it has been suggested by many investigators that the absence of waves, relative to the common observation of oscillatory behavior, is a result of the experimental objectives and techniques. In the case of the mollusk Limax, for which olfaction is the primary sense, it was found using intracellular recordings and optical imaging that, during intervals without an odor stimulus, approximately plane waves of electrical activity propagate from one end of the lobe to the other in a periodic fashion as shown in Figure 1.1 [60]. Two explanations for the propagation of oscillatory type waves are that (i) there is a subpopulation of intrinsically oscillating neurons, the pacemaker, whose output propagates along a chain of excitable neurons or groups of neurons, and (ii) there is a population of coupled, intrinsically oscillating neurons, and the wave motion originates by stable differences in the phases of the rhythmic output among all of the oscillators [60]. There is strong evidence for the latter, that these neurons intrinsically oscillate with a spatial gradient of frequencies such that when connected, a spatial gradient of phases is observed; the active part of the plane wave corresponds to a group of neurons whose phases are associated with firing. Furthermore, this observation is in agreement with theoretical predictions arising from simplified models of coupled neural oscillators. Conversely, when an odor stimulus is presented, the waves cease and the neuronal behavior becomes synchronous across the lobe, possibly arising from sparse long-range

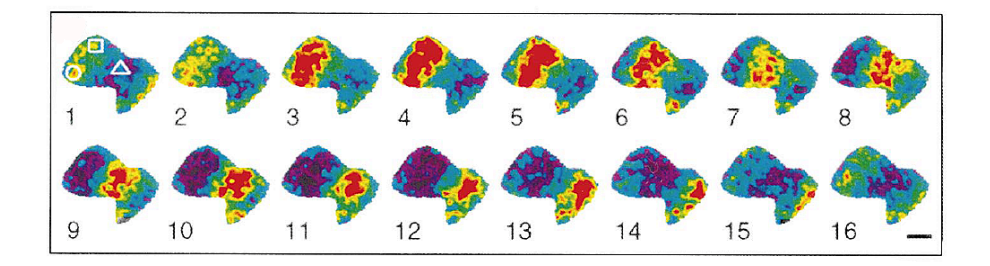


Figure 1.1. Succesive images of the plane wave motion of the membrane potential in the olfactory lobe of the Mollusk Limax over the course of one cycle. Red indicates depolarization and purple indicates hyperpolarization. The time scale is 112 ms/frame and the bar is 100 μ m. Adapted from Ermentrout and Kleinfeld [25, 60].

connections that become active due to the increased activity associated with the presentation of the stimulus. It has been found experimentally that neurons are most sensitive to changes in their input during the half-period preceding the firing of an action potential. One idea explains that the computational role of waves is to ensure that, at any point prior to the introduction of a stimulus, there is a group of neurons that are maximally responsive to the stimulus input, while only a fraction of the neurons are unresponsive [60]. This is related to the "searchlight hypothesis" introduced by Francis Crick [20].

Traveling waves in cortical tissue are also believed to occur in vivo during epilepsy and migraines in humans [17], strongly indicating that such waves can have nontrivial effects on the function of the brain. The two main classes of epileptic seizures are partial seizures, which originate in a localized, or focal, region of the brain, and generalized seizures, which begin simultaneously everywhere within a region of the brain. Partial seizures can generalize very rapidly, obscuring this distinction, since they are observed through electroencephalography (EEG), which measures the dynamics of electric field potentials on the scalp, inferring the activity within the brain. Furthermore, partial seizures can spread to envelop the entire cortex, implying that the activity associated with the seizure is capable of propagating spatially [76]. A few apparent pathways for propagation that should be considered are (i) connections lying within the cortex, (ii) white matter (mylenated axons), which connect adjacent and distant areas of cortex, and (iii) reciprocal connections between cortical and subcortical regions.

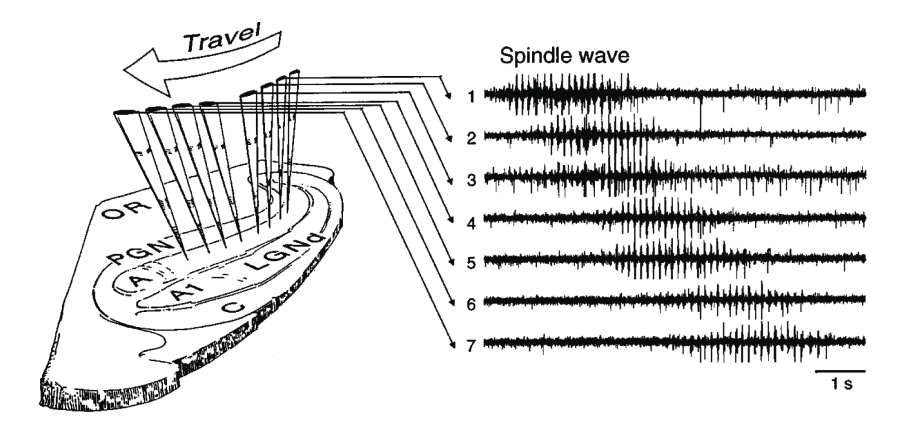


Figure 1.2. Multielectrode recording of neurons in a thalamic slice, illustrating the propagation of a traveling wave of spikes along a line. Adapted from [72].

In the case of intracortical spread of epileptic activity (i), one of the primary experimental paradigms is the generation of traveling waves of activity, also referred to as epileptiform discharges, in disinhibited cortical slice preparations [15, 17, 36, 110, 82, 83]. Such waves can be measured using multielectrode recordings, which are distributed spatially over the tissue as shown in Figure 1.2, or optical imaging using voltage sensitive dyes (see Figure 1.1). The cortex has a layered structure with strong (vertical) connections between layers such that electrical activity travels faster between layers than across layers. Vertical slice preparations that are pharmacologically disinhibited generate discharges, or pulses of activity, which spread horizontally across layers when the slice is electrically stimulated in an appropriate fashion. For example, the drug bicuculline is an antagonist of GABAA, the dominant, fast inhibitory neurotransmitter. The idea is that, when excitatory cells are active, they excite the inhibitory cells, which subsequently regulate the excitation; however, if inhibition is impaired, synchronous excitatory activity overwhelms and can propagate outward from a focal region, entraining other neurons. Note, the propagation velocity of these synaptically generated waves is of the order 0.06 m/s, which is much slower than the typical speed of 0.5 m/s found for action potential propagation along axons. It has been proposed that disinhibition, i.e., the suppression of the effect of inhibitory connections in the network, is a potential mechanism for the spreading waves observed in epilepsy [17].

Recently, Steven Schiff et al. [87] have confirmed a fundamental prediction of a Wilson-Cowan-type firing rate model that was proposed by Pinto and Ermentrout to model traveling waves in disinhibited cortical slices. The model features the simplification of a Heaviside firing rate function, which consequently enforces a hard threshold, see section 1.1.2. The theory predicts that either no traveling wave exists or at most one (numerically) stable traveling wave exists. The velocity of the wave depends on the threshold, increasing the velocity, if the threshold is reduced, and decreasing the velocity, if the threshold is increased, ultimately leading to propagation failure at nonzero speed and width [80, 87]. To modulate neuronal thresholds experimentally, Schiff et al. use electric fields, which have also been shown to modulate activity propagation in cardiac tissue [87]. The effect is due to the polarization of asymmetric neurons, which occurs very quickly (20 ms) and can be maintained for seconds to minutes. Threshold modulation in this case seems to be a change in the relative difference between the membrane potential of the neuron and the threshold for firing; rather than threshold modulation, it should probably be viewed as a change in the resting potential, since a sufficiently strong electric field causes the neuron to fire repetitively, similar to current injection. In any case both views are mathematically equivalent, as far as the model is concerned.

The experiments were performed on rat neocortical slices, which were pharmacologically disinhibited using picrotoxin, a blocker of the inhibitory neurotransmitter GABA_A. Layer 5 neurons, which are necessary to initiate and maintain propagation of traveling waves, have long apical dendrites which facilitate polarization by electric fields. A positive electric field is one that is oriented in the direction from dendrite to cell body, having the effect of increasing the membrane potential; hence a positive (negative) electric field is used to decrease (increase) threshold. A stimulating electrode, placed in layers 5-6 at one end of the slice, generated waves with a 0.15 ms current pulse of 0.1-1.0 mA. As shown in Figure 1.3, spatially localized electric fields, in addition to electric fields applied to the entire slice, were studied revealing that positive electric fields (lowered thresholds) produced increased wave speeds and that negative electric fields (increased thresholds) produced decreased wave speeds, with propagation failure occurring at nonzero speeds. This agreement between theory and experiment is important because it offers support for the use and analysis of firing rate models. However, more predictions of the theory need to be tested to gain full confidence in the ability of the model to describe cortical tissue. One such prediction, lying at the heart of this dissertation, will be discussed later.

Another example of spatiotemporal behavior related to sensory inputs is found in the head direction system of rats, which is located in the hippocampal formation and other closely related areas. It is found that the direction of

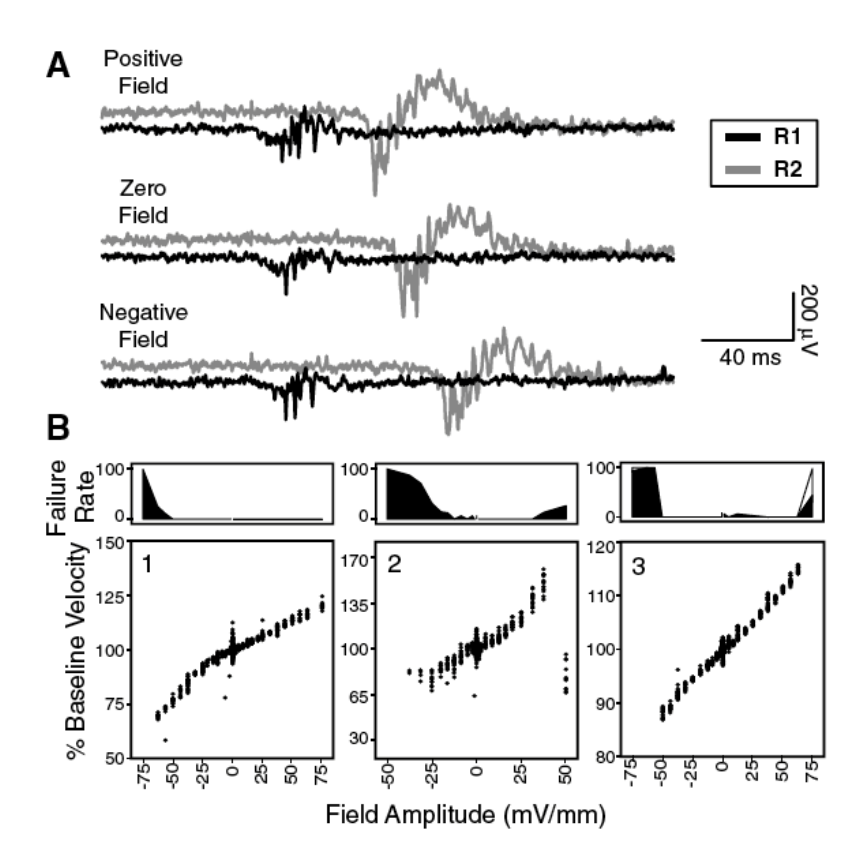


Figure 1.3. Control of wave propagation in cortical slice preparations using electric fields. (a) Extracellular recordings are made during positive (top traces), zero (middle traces), and negative (lower traces) electric field application. The activity wave arrived at R2 earlier during positive field (top) and later during negative field (lower), relative to zero field (middle) application. (b) Wave speed (bottom) normalized by baseline speed and failure rate (top) as a function of field amplitude is shown for three separate experiments. As the field amplitude became more positive (negative), the speed increased (decreased). As the field amplitude became increasingly negative, the propagation failure rate increased to complete failure. Adapted from [87].

the rat's head is encoded into the firing patterns of a special group of cells, referred to as head-direction (HD) cells: regardless of the position of the rat, a unique subset of these HD cells fires in response to the direction of the head, with each cell exhibiting a tuned response about a single preferred direction indicated by the maximum response [94]. While it is clear that the HD network is highly influenced by visual cues for orientation, it is found that HD cells continue to exhibit directional properties in the absence of orienting visual landmarks or upon entering a novel environment. Moreover, the preferred direction seems to be initiated by the placement of the rat at the beginning of the experimental session [94]. This suggests that the HD cells may use information from the angular movement of the head to determine orientation. One source of the information would arise from inputs from the vestibular system which is responsible for maintaining the vertical orientation of the head, with respect to gravity, when the body undergoes movement. Interestingly it was found that lesions of the vestibular system cause the loss of the direction signal in thalamic HD cells [94].

There have been a fair number of studies of the HD system with varying degrees of detail, most of which have employed attractor networks to ensure the sustained firing associated with a particular direction [68, 115, 86, 40, 94, 112, 111, 99]. Most of these networks are firing rate models of excitatory and inhibitory cell populations on a ring, which are reciprocally coupled by connections whose strengths decrease with the difference in preferred orientation. Note, the topology of these connections allows for neurons with similar preference to be strongly connected yet spatially disparate. When the rodent is fixated in a particular direction, the attractor network approaches a stable bump solution representing a group of neurons with preferences about the preferred direction continuously firing, thus establishing the neural correlate of the current direction of the head. Though it is not usually mentioned explicitly, the rotational invariance of the ring is apparently supported by the finding that the HD cells are coupled such that the rotation angles for preferred directions of different HD cells are always the same. That is, if a visual cue is moved or the animal becomes disoriented, causing the preferred direction of each cell to change, the angular difference between the previous direction and the new direction will be roughly the same for all cells [100, 115]. Each study subsequently differs by what brain region(s) are modeled and how the HD system updates to establish the new direction after the head is rotated. However, each study is similar in that it assumes that inputs representing angular velocity information modify the network in some form to cause the bump to move. As the bump moves, the system integrates the information and should precisely determine the angular distance traversed. This introduces an interesting mathematical problem associated with traveling waves: not only

must the HD system have the ability to support stable traveling waves, it also must be able to handle the transient approach to and from the wave, as the input is initiated and terminated.

These examples illustrate that the spatial connectivity of networks of neurons plays an important role in shaping the corresponding activity patterns and their role in brain function. To be able to understand these complicated networks, a basic theory must be developed to establish some of the fundamental principles of spatiotemporal structures. Firing rate models track the activity patterns of neuronal populations and, therefore, will be useful in understanding systems where spatiotemporal activity patterns play a role in neural processing.

1.1.2 Theoretical Background

In this section we review the previous mathematical work related to the formation of stationary pulse or bump solutions and traveling wave solutions in neural network, firing rate models on infinite domains. Although the brain is not infinite in extent, if the majority of the activity occurs on a bounded subdomain, the infinite domain is a reasonable approximation that highly facilitates mathematical analysis. Furthermore, it is mathematically advantageous to consider continuum models when analyzing spatially extended systems. Although neuron cell bodies form a sort of discrete lattice, it is natural to view a sufficiently large population as a neural continuum. In fact, a 1 mm³ patch of cortical tissue contains 10⁵ neurons, and, since neurons collect inputs from a large number of cells, the effect of a single neuronal input on the firing rate of a cell is minor. Implicit in many firing rate models is the assumption that the fields that represent neuronal activity evolve according to first order dynamics. This assumption ascends from the first order dynamics of the RC circuit-type model for the cell body, though the associated time constants are not necessarily the same; see Chapter 2. With some additional assumptions, spatially extended, neural firing rate models offer a surprisingly high degree of analytic tractability, shedding insight into the existence and bifurcation of bumps and waves.

In 1973 Wilson and Cowan [109, 108] derived a set of one-dimensional equations describing the averaged activity of an excitatory-inhibitory pair of populations reciprocally coupled in a nonlocal fashion, projecting within the population, in addition to the opposite population.

$$\tau_e \frac{\partial u_e}{\partial t} = -u_e + w_{ee} * F_{ee}(u_e) - w_{ei} * F_{ei}(u_i),$$

$$\tau_i \frac{\partial u_i}{\partial t} = -u_i + w_{ie} * F_{ie}(u_e) - w_{ii} * F_{ii}(u_i),$$
(1.1)

where

$$\left(w_{ab} * F_{ab}(u_b)\right)(x) = \int_{-\infty}^{\infty} w_{ab}(x, y) F_{ab}(u_b(y, t)) dy.$$

 u_e, u_i represent the activity of the excitatory and inhibitory populations, respectively. w_{ab} are Gaussian-like functions, referred to as synaptic weight functions that represent the connectivity pattern between neurons, often taken, as a first approximation, to weaken with distance w(x,y) = w(|x-y|). F_{ab} are sigmoidal functions representing the firing rates of the neurons, which effectively activate the connections between neurons. A heuristic derivation of (1.1) is presented in Chapter 2. Wilson and Cowan [109] performed numerical simulations on their model, which revealed that, in the absence of an input, an initial, small, local depolarization can give rise to a stationary, localized pulse or bump of activity. Amari [1] considered a scalar version of this model, assuming the weight function to be a Mexican hat, shown in Figure 1.4, to model inhibition as having a peripheral or lateral effect, with excitation dominant locally. One of the implications of this model is that inhibition acts instantaneously, whereupon the excitatory population u evolves according to

$$\tau \frac{\partial u}{\partial t}(x,t) = -u(x,t) + \int_{\mathbb{R}} w(x-y) f(u(y,t)) dy$$

Furthermore, taking the smooth firing rate function, instead, to be a Heaviside function, he provided an analytically tractable way to study this dynamical system. Amari focussed on stationary pulse solutions and found that inhibition was necessary to stabilize such solutions [1]. A brief description of his analysis is included in Appendix B.1.

Pinto and Ermentrout [81] considered similar one-dimensional stationary pulse solutions in (1.1) under the simplification $F_{ee}(u) = F_{ie}(u) = H(U - \kappa)$, $F_{ei}(u) = u$. For a large range of parameter values, Gaussian-like weight functions generate a stationary pulse existence problem with a Mexican hat that is equivalent to that of Amari's, demonstrating that a Mexican hat weight distribution can arise under more general circumstances. According to Amari's stability analysis, when a pair of pulses exists, the larger is stable, and the pair annihilate in a saddle-node bifurcation. Applying a linear stability analysis to their generalization, Pinto and Ermentrout found that a sufficiently large difference in time constants (slow inhibition) can lead to a Hopf bifurcation of the pulse. The bifurcation was determined, numerically, to be subcritical, causing the medium to relax to the rest state rather than to stable periodic solutions [81]. They were also able to extend the existence of stationary pulses to a particular class of smooth sigmoidal functions F_{ee}, F_{ei} using singular perturbation theory. The pulse was constructed from connecting an excited small region about the origin to the surrounding resting medium via a pair of

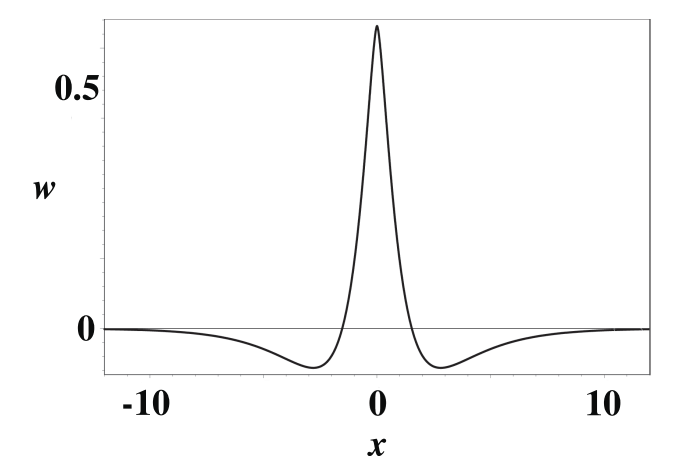


Figure 1.4. General shape of the Mexican hat weight functions, often taken to represent short-range excitation and long-range inhibition, though it can arise under more general circumstances.

symmetric traveling fronts (described below) in the limit $\epsilon \longrightarrow 0$. This result confirms that stationary pulses do persist for smooth firing rate functions, which are more biologically relevant, since averaging tends to smooth out a discontinuous neuronal firing rate. Furthermore, it complements the numerical results of Wilson and Cowan, who have demonstrated that such pulses exist for smooth firing rates away from the singular limit. Most importantly, it indicates that the analytical results obtained using the Heaviside firing rate function are, at the least, characteristic of those for a smooth firing rate.

Others have examined similar models in one and two dimensions, finding multiple bump solutions in one dimension, and single and multiple bump solution in two-dimensions [101, 107, 64, 62, 92]. Taylor [101] considered the existence and stability of two-dimensional pulses in a scalar, lateral inhibition (Mexican hat) network. Curiously, he only considered linear stability with respect to radially symmetric perturbations. It turns out that, in the case of a Mexican hat weight function, this criterion is insufficient to study the stability of such pulses. For particular parameter values it is shown in Chapter 5 of this dissertation [33], as well as in [10], that nonradially symmetric modes can become unstable prior to the radially symmetric mode. To my knowledge, the work of Chapter 5 constitutes the first proper stability analysis of two-dimensional bumps.

Laing and Troy [63] found that, while two-bump solutions exist in a scalar Mexican hat network with Heaviside firing rate, they are numerically unstable. In order to stabilize two-bump solutions, they needed a weight function that resembled a Mexican hat weight function with at least three zeros rather than one. In the case of two dimensions, they find, numerically, the coexistence of solitary and two-bump solutions. To generate two-dimensional multibump solutions for a smooth firing rate, Laing and Troy [62] considered an oscillatory weight function—resembling a Mexican hat, which continually alternates between positive and negative—for which a scalar, Amari-type equation could be transformed into a fourth-order PDE. Using numerical methods to study the existence and stability (AUTO) of solutions composed of one or more concentric rings of activity, they found a single ring destabilized into a three-bump solution, a double ring into a seven-bump solution, and a triple ring into an eleven-bump solution. The symmetry of the spatial eigenmode that dominates the instability determines the number of bumps that emerged.

To contrast the case of stationary pulses and nonlocal inhibition, Amari found that traveling waves existed in a network in which the inhibitory cells at x were activated only by local excitatory cells at x. A brief description of his analysis is given in Appendix B.2. Ermentrout and McLeod [26] take a step back and examine traveling front solutions of the following one-dimensional firing rate model for a purely excitatory scalar network with a smooth firing rate and more general temporal dynamics,

$$u(x,t) = \int_{-\infty}^{t} \alpha(t-\tau) \int_{-\infty}^{\infty} w(|x-y|) F(u(y,\tau)) dy d\tau, \qquad (1.2)$$

under the assumptions that w is a non-negative, even function, that α is a positive, monotonically decreasing function, and that F is monotonically increasing so that f(u) = -v + F(v) has precisely 3 roots, $u_1 < u_2 < u_3$, with $f'(u_1), f'(u_3) < 0$ and $f'(u_2) > 0$. Consequently, the system has two stable spatially homogeneous solutions u_1, u_3 ; a traveling wave is a spatially inhomogeneous, translationally-invariant solution, which approaches u_3 at $-\infty$ and u_1 at $+\infty$, traveling with constant speed. Incidentally, α represents the synaptic time-course and, when taken to be a decaying exponential, leads to first order temporal dynamics. To prove the existence and uniqueness of traveling fronts, they viewed (1.2) as a continuation of the bistable reaction-diffusion equation

$$\frac{\partial v}{\partial t} = \frac{\partial^2 v}{\partial x^2} + f(v),$$

proven by Fife and McLeod [31] to support similar stable, unique traveling front solutions. Furthermore, the speed of the wave has the same sign as

$$\int_{u_1}^{u_3} f(u)du,$$

and, since the function f is cubic-like, wave fronts travel with positive (negative) speed, when the threshold of F is low (high), whereas stationary fronts exist when the negative and positive areas of the cubic exactly balance. It is by using this general result that Pinto and Ermentrout were able to construct singular stationary pulses for smooth firing rate functions [81]. This clearly opens the way to develop analogous perturbation constructions that are ubiquitous in the reaction-diffusion literature [104, 55, 30]. In the case of the Heaviside firing rate, Ermentrout and McLeod also explicitly determined the profile of the front solutions and the dependence of wave speed on the firing rate threshold [26].

To model disinhibited cortical tissue, Pinto and Ermentrout [80] considered a network of purely excitatory neurons u, intrinsically modulated by a negative feedback mechanism, such as spike-rate adaptation or synaptic depression. Spike-rate adaptation is a phenomenon whereby a constant current injection to a neuron elicits an attenuated response of the firing rate over time; it is thought to be produced by slow potassium currents that become active after continual firing and tend to hyperpolarize (reduce excitability) the cell. Since the feedback ϱ is intrinsic, its effect is only local, with the neuronal population evolving according to

$$\tau \frac{\partial u}{\partial t}(x,t) = -u(x,t) + \int_{-\infty}^{\infty} w(x-x')f(u(x',t))dx' - \varrho(x,t)$$

$$\frac{1}{\varepsilon} \frac{\partial \varrho}{\partial t}(x,t) = -\hat{\beta}\varrho(x,t) + u(x,t), \tag{1.3}$$

which can be thought of as an integro differential analogue of the FitzHugh-Nagumo equation. Similarly Pinto and Ermentrout [80] were able to construct a singular traveling pulse solution for a smooth firing rate, using the work of Ermentrout and McLeod [26]. In the case of a Heaviside firing rate away from the singular limit and the seemingly unnecessary simplification of setting $\beta=0$, they demonstrate the existence of a pair of traveling pulses for relatively small ϵ using a shooting argument. Of the pair, the faster and wider pulse is found numerically to be stable, with the pair annihilating in a saddle-node bifurcation. Note in Chapter 6 existence curves are produced for the full model ($\beta\neq0$) which are qualitatively similar, though more restricted within parameter space.

In the case of a Heaviside firing rate function, Zhang [116] has recently confirmed the stability of the traveling front in the scalar equation (1.2) for a Heaviside firing rate, as well as the (faster) pulse of (1.3) in the singular limit $\epsilon \longrightarrow 0$, using Evans functions, a technique used to study the stability of traveling waves in unbounded domains. Arising from the linear stability analysis of a constant speed traveling wave, the Evans function is simply a complex analytic function whose zeros identify with the eigenvalues of the linearization. Once the essential spectrum is shown to be negative, the Evans function may

be used to study the eigenvalues to determine the linear stability of the wave. Such a function was first introduced by John Evans, who rigorously considered the stability of traveling waves in a general class of reaction–diffusion equations which includes the Hodgkin–Huxley and FitzHugh–Nagumo equations and models action-potential conduction along an infinite nerve axon [27, 28, 52]. In contrast with the general class of equations for which the theory of Evans functions applies, the Evans function can be calculated explicitly for neural integrodifferential equations with Heaviside firing rate, greatly facilitating the stability analysis.

The above studies have all considered the connections and inputs in the cortex to be homogeneous and isotropic. The real cortex, however, is more realistically modeled as an inhomogeneous medium. Inhomogeneities in the synaptic weight distribution w may arise due to the patchy nature of long-range horizontal connections in superficial layers of cortex. For example, in primary visual cortex the horizontal connections tend to link cells with similar stimulus feature preferences such as orientation and ocular dominance [70, 113, 4]. The variation of the feature preferences across cortex is approximately periodic and this induces a corresponding periodic modulation in the horizontal connections. It has been shown that an inhomogeneous, periodic modulation in the strength of synaptic interactions induced by long-range patchy connections can lead to wavefront propagation failure of fronts in the scalar, excitatory neural network [8]. If the wavelength of the periodic inhomogeneity is much shorter than the characteristic wavelength of the front, then averaging theory can be used to achieve an effective homogenization of the neural medium along similar lines to those previously developed for a model of calcium waves [58] and for a model of chemical waves in a bistable medium [56]. Another important source of spatial inhomogeneity is the external input I(x). Such inputs would arise naturally from sensory stimuli in the case of the intact cortex and could be introduced by external stimulation in the case of cortical slices. The analysis and effect of such inputs is the subject of this dissertation.

One of the only studies concerning the effect of an inhomogeneous input in a Wilson-Cowan type model was done by Xie and Giese [111] in a scalar network with asymmetric lateral inhibition. Such a network consists of a Mexican hat weight function w_o , which is shifted asymmetrically from the center such that $w(x,x')=w_o(x-x'-s)$ for some fixed displacement s. This displacement introduces a form of directional selectivity, in which the network responds preferentially to stimuli moving in a particular direction, and has thus been suggested as a possible recurrent mechanism for the directional selectivity of neurons in visual cortex [98, 68]. In a sense the shifted weight function causes the stationary bump of Amari's model to travel, instead, with constant speed. In this network Xie and Giese [111] have analyzed the existence and stability

of traveling pulses that are locked to an input moving with constant speed, providing a vague account of the conditions of existence, the associated regions of parameter space supporting such waves, and precisely how such waves lose stability. They effectively construct the associated Evans function, although they do not identify it as such, and show how the pulse can destabilize when the stimulus velocity differs significantly from the natural velocity of unidirectional intrinsic waves; this instability generates a transition to a so-called *lurching wave*, which travels forward in a discontinous, periodic fashion.

From our analysis of their model (not included here), we have found that, although the wave loses stability in a Hopf bifurcation, the bifurcation appears, numerically, to be subcritical exhibiting a sharp jump to lurching waves. Interestingly, we additionally find that, when the strength of the nonlocal inhibition is reduced, the lurching wave undergoes a smooth transition to a pulse-emitting solution; initially, the nascent waves fail to propagate, until the inhibition is sufficiently reduced that they propagate indefinitely. In order for a pulse-emitting solution to exist, it is necessary that the medium, in the absence of the input, support (natural) traveling waves. The pulse-emitter is the response of the system to the input, characterized by its ability to stimulate the surrounding medium, periodically shedding natural traveling pulses.

Yet another neural system in which a traveling pulse can undergo a Hopf bifurcation, leading to the formation of lurching waves, is a synaptically coupled integrate—and—fire network with discrete axonal delays [37, 39]. Here a pulse consists of a single propagating spike, and the instability is due to fluctuations in the sequence of neuronal firing times, which start to grow at a critical value of the delay [7]. This example applies to intrinsic waves in a homogeneous network.

1.2 Content of Dissertation

While it is important to understand the ability of neural networks to self-sustain persistent activity, it is of enormous importance to understand the effect of *inputs*, as they are fundamental to neural processing in the brain. From anatomy alone, it is clear that the seemingly endless number of regions and subregions of the brain are in communication with each other via inputs arising from action potentials transmitted along axonal projections. Of course, the effects of such inputs can be quite complex and subtle. However, it is very surprising that almost no one has examined the effects of simple, sustained, inhomogeneous inputs in neuronal firing rate models, especially in the wake of the work of Amari. As will be demonstrated in this dissertation, localized inputs generate interesting and nontrivial behavior in neural network models, offering experimentally testable predictions to compare with real cortical tissue.

Inputs into and from within the cortex are often highly selective regarding the layer into which they project. For example, inputs from the retina project mainly into layer 4 of the primary visual cortex in the form of a map; thus a small, stationary point stimulus in the visual field results in a small localized sustained input in the layer 4 of the visual cortex. Alternately, inputs in vivo could simply represent a local region of enhanced depolarization or excitability. In vitro such inputs would represent a current injection from electrodes or the effect induced by applying an external electric field to the tissue.

In the neural network models analyzed herein, the effect of localized inputs can be generally classified by three modes of activity viewed either in a stationary or traveling frame: (i) spatially localized stationary solution, (ii) spatially localized periodic solutions, (iii) periodic pulse-emitting solutions. The transition to periodic solutions arises from either super- or subcritical Hopf bifurcations and is the result of a temporal interplay between excitation and local inhibition. However similar results occur in the case of nonlocal inhibition. We often refer to the spatially localized periodic solutions as breathing pulses or breathers, since they resemble pulses inhaling and exhaling.

The emergence of the three types of solutions can be described in a simple senario. Consider an excitatory neuronal population with slow adaptation (local inhibition) subject to a localized current input. For sufficiently large current input, the neural response approaches a stationary pulse solution, which represents a spatially localized group of neurons continuously firing with the surrounding medium quiescent. In this case the effects of excitation and adaptation are in equilibrium. As the strength of the current input is reduced, the stationary pulse undergoes a supercritical Hopf bifurcation, rendering it unstable. Instead a new stable solution emerges, a breather, resembling a pulse whose amplitude is periodically modulated in time. In this case the balance between excitation and adaptation has been lost, and an endless tug-of-war ensues. The amplitude of oscillations grows increasingly large as the input strength is reduced further. Ultimately, reduction of the input leads to a secondary instability leading to a sharp transition to a solution that exhibits breathings and the emission of traveling pulses. However, the inclusion of nonlocal inhibition can serve to preclude the emission of such waves. Finally a sufficient reduction in the input causes the entire medium to relax to a subthreshold state, with a small, subthreshold bump reflecting the input. Interestingly, upon reexamination of the paper of Wilson and Cowan, we found that they also numerically found stable breathers and pulse-emitters induced by localized inputs [109]. Hence the analysis presented herein provides an analytic approach to identifying the emergence of breathing solutions and, furthermore, provides a testable prediction of the effect of adaptation in the response to a persistent localized input in a disinhibited cortical slice.

One application of breathers may be to bind correlated inputs. A fundamental problem in neuroscience, known as the binding problem [41, 95], is to determine how neural circuits manage to realize a contiguous stimulus. Returning to vision for example, throughout the visual cortex neurons possess minute windows to the visual field know as receptive fields. Thus, there is a small fraction of the visual field to which a neuron in the visual cortex responds, yet the brain has the ability to bind the myriad of fragmented features of the visual world into one seamless image. In particular, it is able to perceive the contiguity of an cohesive object. One clue that has been discovered is that the neurons whose receptive fields align with the object share a similar periodic modulation of their firing rates [41, 95]. The current approach to explaining this behavior is using coupled oscillating neurons. However, since inputs from one region of the brain to another are relatively weak, inputs from the stimulus may be in a regime that generates breathing solutions in the visual cortex. It is possible that these breathers interact and synchronize, inducing the synchronous fluctuations in firing rate, and may serve as a rudimentary level for the binding of a stimulus.

As mentioned earlier, it is thought that focal epilepsy has the ability to spread and entrain large regions of the brain, in particular, the cortex. In contrast to the idea that the traveling waves arise from coherent neural oscillators, the pulse-emitter illustrates that a weak input or a local depolarization can entrain a local region of disinhibited tissue to act as a pacemaker, generating the periodic spread of waves through the excitable tissue. Though this is most likely not the entire explanation, it nevertheless may play some role in onset or sustainment of epileptic seizures.

Another application of breathers, suggested by Wilson and Cowan [109], is edge detection. It is well documented that the primate visual system is tuned to detect edges or sharp contrast. In their numerical studies, Wilson and Cowan used a step-like localized input and found that the amplitude of oscillation of the breather was the largest near the edge. They suggested that this strong modulation may be responsible for the enhancement of the feature contrast.

Hereupon we summarize the contents of the dissertation. Chapter 2 provides a brief description of the biological and mathematical basis for the some of the models and ideas central to mathematical neuroscience. Beginning with a short summary of the anatomy and physiology of neurons and neural communication, we proceed by offering heuristic derivations of mathematical models from the cellular level to the population level. The *firing rate models* of section 2.3.3 are the final culmination of a series of mathematical simplifications and define the class of models studied herein.

Each subsequent chapter concentrates on different problems associated with the Pinto and Ermentrout model with the inclusion of an inhomogeneous input function I.

$$\tau \frac{\partial u(x,t)}{\partial t} = -u(x,t) + \int_{-\infty}^{\infty} w(x-x')f(u(x',t))dx' - \beta \varrho(x,t) + I(x,t)$$

$$\frac{1}{\epsilon} \frac{\partial \varrho(x,t)}{\partial t} = -\varrho(x,t) + u(x,t). \tag{1.4}$$

Notice that the parameter β now represents the strength of the local negative feedback, whereas before it related to the decay of local inhibition; see equation (1.3); for positive β , the two systems are qualitatively similar, however, the effects of taking $\beta \longrightarrow 0$ are different.

We begin Chapter 3 by considering traveling front solutions of (1.4) with I=0, which exist for sufficiently weak adaptation strength (small β). Weak adaptation reduces the value of the elevated spatially homogeneous state, thus the profile of the front resembles a shrunken version of the front in the scalar system $(\beta = 0)$. We then carry out a perturbation expansion in powers of the wavespeed c to show that a stationary front can undergo a supercritical pitchfork bifurcation at a critical rate of negative feedback ϵ_c , leading to bidirectional front propagation. In the case of a spatially homogeneous input, the fronts bifurcate according to a codimension 2 cusp bifurcation. Analogous to the case of reaction diffusion systems, the front bifurcation acts as an organizing center for a variety of nontrivial dynamics including the formation of oscillatory fronts or breathers. We show how the latter can occur through a Hopf bifurcation from a stationary front in the presence of a weak stationary input inhomogeneity. The fact that the nonlocal integrodifferential equation (1.4) exhibits behavior similar to a reaction diffusion system might not be surprising, particularly given that for the exponential weight distributions $w(x) = e^{-|x|}$, equation (1.4) can be reduced to a PDE of the reaction-diffusion type. It is important to emphasize, however, that our results hold for a more general class of weight distribution w(x) for which a corresponding (finite-order) PDE cannot be constructed. Hence, the analysis is a nontrivial extension of known results for reaction-diffusion equations.

Finally, we analyze the existence and stability of stationary fronts in an exactly solvable model, which is obtained by taking the high gain limit $\gamma \to \infty$ of the sigmoid function f such that $f(u) = H(u - \kappa)$ where H is the Heaviside function and κ a threshold. The exactly solvable model allows the study of oscillatory fronts beyond the weak input regime. Rather than perturbing about the homogeneous case, we are able to consider a large input amplitude for which wave propagation failure occurs due to the pinning of a stationary front. A subsequent reduction in the amplitude of the input then induces a Hopf

instability leading to the formation of a breather. We conclude our analysis of the exactly solvable model, by deriving conditions for the locking of a traveling front to a moving input, and show how locking depends on both the amplitude and speed of the input. The idea of locking to a moving input will be explored more deeply within the context of pulses in Chapter 6.

This chapter illustrates the primary differences between analyzing the model with a smooth and Heaviside firing rate. The smooth firing rate allows us to apply perturbation theory in a straightforward manner in the case of fronts, which is beneficial since smooth firing rates are more biologically relevant, matching the input-output characteristics of populations of neurons quite well. However, they present great difficulties in finding exact solutions, calculating the dependence of wave speeds on parameters, and addressing stability, and, moreover, present even greater hurdles when considering traveling pulse solutions. On the other hand, while the Heaviside firing rate introduces its own set of problems in the way of carrying perturbation theory to higher orders, it enables us to determine explicitly the existence, stability and bifurcations of stationary and traveling fronts, and more importantly pulses, in the presence of external inputs, without any restrictions on the size of the input. Although it is difficult to carry out a nonlinear analysis to determine the direction of bifurcation, we can use numerical simulations to examine the transition associated with the bifurcation and, moreover, explore the behavior beyond the bifurcation, outside of the applicable regime of the analysis.

In Chapter 4 we develop the analytical theory for the existence and stability of stationary pulse solutions which are induced by a unimodal input. In order to construct exact wave solutions, we consider a Heaviside firing rate, in which case (1.4) becomes

$$\tau \frac{\partial u(x,t)}{\partial t} = -u(x,t) + \int_{-\infty}^{\infty} w(x-x')H(u(x',t)-\kappa)dx' - \beta \varrho(x,t) + I(x)$$

$$\frac{1}{\epsilon} \frac{\partial \varrho(x,t)}{\partial t} = -\varrho(x,t) + u(x,t), \tag{1.5}$$

where κ represents the firing rate threshold. In the absence of an input, a stationary pulse solution, if it exists, is unstable, acting as a separatrix that either generates a pair of counter-propagating pulses or a return to the resting state. However, a stationary pulse is stabilized by a sufficiently large input, leading to wave propagation failure of an approaching wave. The stable pulse disappears in one of two ways, (i) for $(\epsilon > \beta)$ a stable-unstable pair of stationary pulses simply annihilate in a saddle-node bifurcation, and (ii) for $(\epsilon < \beta)$, the stable pulse loses stability in a Hopf bifurcation. Although there are multiple bifurcation senarios, the following illustrates the general idea. Stationary pulses exist for all input strengths above the saddle-node point

and are stable for sufficiently large inputs. A supercritical or subcritical Hopf bifurcation (determined numerically) occurs at some value of input strength above the saddle-node point, leading either to a periodic modulation of the stationary pulse or breather, in the supercritical case, or to a subthreshold bump, in the subcritical case. The breather subsequently undergoes a secondary instability leading to a pulse-emitter, a breather-like solution that periodically emits traveling pulses into the surrounding medium. Interestingly the breather may lose stability due to a subcritical period-doubling bifurcation. The evidence for this is that a cascade of supercritical period-doubling bifurcations occurs for increasingly large input widths, followed by a sharp transition to the pulse-emitter. Furthermore, for a range of inputs after the transition to the emitter, there is mode-locking between the oscillation frequency of the breather and the rate of wave emission, giving way ultimately to regular emission. The pulse-emitter eventually disappears for sufficiently small inputs, and the medium approaches a subthreshold bump, i.e., the rest state. Interestingly, the breather and pulse-emitter can persist at inputs below the saddle-node point, i.e., below the minimum input necessary for the existence of a stationary pulse. Finally, analogous forms of oscillatory waves are also shown to occur in a more biophysically realistic conductance—based model that features a slow potassium current to induce spike-rate adaptation, lending further support for the ability of firing rate models to describe the activity of detailed biophysical models.

In Chapter 5 we extend our analysis to radially symmetric pulses in a two-dimensional network, which is defined by either an excitatory (positive) weight function or a Mexican hat weight function. The Mexican hat weight, in this case, arises from the excitatory-inhibitory model (1.1), with the firing rate assumptions proposed by Pinto and Ermentrout, subject to the additional assumptions that the excitatory population exhibits adaptation and the fast inhibitory population operates in quasi-steady-state. While many of the results from the one-dimensional case carry over, the Mexican hat weight function is capable of producing nonradially symmetric breathers. Furthermore, other spatially-localized solutions seem to coexist, including spatially-localized rotating solutions, or rotors, some of which exhibit a breathing motion. The difference in the effect of the different weight functions is exemplified by the fact that, depending on the strength and width of the input, higher order spatial modes associated with the linearization may dominate the instability, whereas in the excitatory case the lowest order, radially symmetric mode always dominates. Although we do not include it, the two-dimensional excitatory-inhibitory verision of (1.1) under the firing rate assumptions proposed by Pinto and Ermentrout, interestingly, follows the behavior of the excitatory case. However, we expect the full three variable model to have qualitatively similar results to the quasi-steady-state approximation.

In Chapter 6 we consider the effect of localized inputs moving with constant speed, in which case (1.5) becomes

$$\tau \frac{\partial u(x,t)}{\partial t} = -u(x,t) + \int_{-\infty}^{\infty} w(x-x')H(u(x',t)-\kappa)dx' - \beta\varrho(x,t) + I(x-vt)$$

$$\frac{1}{\epsilon} \frac{\partial\varrho(x,t)}{\partial t} = -\varrho(x,t) + u(x,t). \tag{1.6}$$

Working in the moving frame of the input, we use the input strength \mathcal{I} and speed v as bifurcation parameters, to determine the existence of stimulus–locked pulses, and construct existence tongues in the (v,\mathcal{I}) -plane, whose tips at $\mathcal{I}=0$ correspond to the intrinsic waves of the homogeneous network. To illustrate the general approach, we begin by considering the simpler case of zero negative feedback ($\beta=0$), for which equation (1.6) reduces to a scalar equation in u. The corresponding existence tongues for stimulus–locked fronts and their stability are completely determined analytically.

We then consider the existence of stimulus—locked pulses in the full vector system (1.6), numerically solving a set of nonlinear functional equations in order to construct the associated tongues. In the particular case of an exponential weight distribution, we find that there are two tongues in the positive v domain, corresponding to an unstable/stable pair of right—moving intrinsic waves. We determine the stability of the waves within these existence tongues by first constructing the Evans function and then numerically calculating its zeros. We show that, as the input is reduced, a stimulus-locked wave within the tongue of the unstable intrinsic wave can undergo a Hopf bifurcation leading to the emergence of a traveling oscillatory wave. The latter takes the form of either a breather or a pulse-emitter in the moving frame of the stimulus, depending upon the direction of bifurcation. In the limit $v \to 0$ our results reduce to those obtained for stationary inputs (Chapter 4). Finally, we present numerical simulations illustrating the formation of traveling breathers and pulse-emitters.

CHAPTER 2

BIOPHYSICS AND MATHEMATICAL MODELS

2.1 Anatomy and Physiology

The primary function of the nervous system is the communication and processing of information. The nerve cell, or *neuron*, is the fundamental unit of the nervous system, and it is believed that electrochemical signals transmitted from neuron to neuron are the carriers of this information. The human nervous system encompasses a vast network of 10^{12} neurons, and a 1 mm³ patch of cortical tissue contains 10^5 neurons.

A neuron generally is composed of two parts, the cell body (soma) and the neurites. The cell body contains all of the subcellular organelles found in a typical animal cell, and the size of the soma ranges from 5-120 $\mu \rm m$ in diameter. Neurites are long cylindrical projections from the cell body and are classified by two types: dendrites and axons. Dendrites are highly branched extensions of the cell body that can reach 1 mm in length; they are extensions in that they also contain organelles and are capable of protein synthesis, unlike axons. A neuron may have one or more dendrites, collectively referred to as the dendritic tree. Nerve cells typically have a single axon, usually emerging from the cell body at a junction called the axon hillock. Axon diameters range from 0.2 to 20 $\mu \rm m$ in humans and vary in length from a few $\mu \rm m$ to over a meter. Axons often branch, particularly towards their distal end; these branches are called axon collaterals, the ends of which are swollen terminals (boutons) and usually contain mitochondria and vesicles. Axon terminals form the *presynaptic* component of the neuron.

Neurons exhibit great diversity in their functional and morphological characteristics. Some neurons have extensive dendritic trees, whereas others have no dendrites or axons. It is possible that there are more than 10,000 different morphological classes of neurons in the brain. Hence, while the nervous system seems homogeneous in that it is comprised of neurons, the myriad of functions and morphologies of the neurons renders it a highly complex and diverse system.

As a simplifying assumption, we will have a generic neuron in mind, one with a soma, dendritic tree, and axon.

As described later in more detail, the communication and processing of infomation is primarily due to the movement of ions (charged atoms) across the cell membrane of neurons. Ion channels embedded in the membranes of the soma and axons control of the influx and efflux of ions, allowing for changes in the potential inside the cell or axon. Although there are neurons that intrinsically oscillate, in the absence of inputs, the membrane potential of most neurons approaches a constant value, referred to as the resting potential or equilibrium potential. Incidentally, the intracellular potential of the cell at rest is less than the extracellular potential, resulting in a polarization across the membrane of the cell. A cascade of events is possible whereby an increase in potential in the soma triggers an increase in the potential of the axon, and a pulse is propagated along the axon. This is the means by which information from a neuron is initially transmitted, rendered possible by the active properties of the ion channels. Therefore, it is recognized that the potential difference across the cell, or transmembrane potential, is an important physical quantity to describe the communication of information: the fluctuations in the transmembrane potential are signals and embody the information.

Upon entering the terminal bouton, the form of transmission of information undergoes a fundamental change from electrical to chemical in nature. The terminal bouton, essentially the end of the presynaptic neuron, makes a point of contact, or synapse, with the dendrite of the postsynaptic neuron. As the signal reaches the terminal bouton of the presynaptic neuron, vessicles containing chemicals called neurotransmitters are released into the extracellular junction between the two neurons, or synaptic cleft (30 nm wide). These neurotrasmitters bind to receptors on the postsynaptic neuron, which subsequently open ion channels on the postsynaptic neuron, inducing a change in transmembrane potential. This process is known as synaptic transmission and is the fundamental means of neuron-to-neuron communication. Although several neurotransmitters are involved, triggering different synaptic currents with various time courses, we shall, for mathematical reasons, employ a more abstract and generic notion of synaptic transmission. In the firing rate models we consider, synaptic transmission is characterized by the following assumption: there is a functional relationship between the output firing rate of the postsynaptic neuron and the activity of the presynaptic neuron. Synaptic coupling is then determined by the weighted sum of the corresponding firing rates, arising from all presynaptic connections to the postsynaptic neuron.

The transmission process in dendrites, once believed to be entirely passive with electric potential spreading via diffusion, is facilitated by voltage dependent ion channels embedded in the dendritic shaft (primarily sodium)

and in dendritic spines, small mushroom-shaped appendages lining the shaft (primarily calcium). The dendrites integrate the signals received from the neurons to which they are connected and modify the potential of the soma accordingly. Subsequently, there is a threshold or dichotomy of behavior of the soma. If the transmembrane potential of the soma increases by a small amount, eventually it will return to the resting potential; however, if transmembrane potential is increased by a sufficient amount, ion channels open causing a dramatic increase in the transmembrane potential which is followed by a return to rest. This dramatic increase and decrease is known as an action potential, and the cell is said to fire. This induces the pulse, mentioned earlier, in the axon, and the process repeats itself. It is this feature of neurons, i.e., the generation and transmission of signals, that distinguishes neurons from most other cells. Moreover, this property makes neural networks an excitable medium, thought to be an advantageous characteristic that allows signals to be distinguished from background noise [59]. Interestingly, the ion channels associated with the dendrites also facilitate the reverse direction of information transfer in the form of backward propagating spikes, which is thought to modify the action and effect of the synapse.

The patterns of synaptic connections between neurons in the nervous system are extremely complex and are one of the major sources of mathematical difficulty. Some neurons make connections with neurons nearby; others connect to neurons up to a meter away. Neurons have a distinct direction of primary signal propagation (not including back–propagating spikes), as they receive synaptic input at the dendritic end and transmit synaptic output at the axonal end, however there is great diversity in the connectivity patterns between neurons. For example, neurons can make reciprocal synapses onto their presynaptic cells, make lateral syapses with parallel neurons, or make serial synapses forming local loops. Hence, although there is a polarization with respect to transmission within neurons, this does not necessarily imply a polarization of transmission within a population of neurons.

As the word implies, the cerebral cortex is a layered structure, composed primarily of the six-layered neocortex, which is responsible for voluntary movement, sensory perception, and cognitive function. The cortex reveals a high density of neuron cell bodies with each layer containing different proportions of neurons. Two primary types of neurons are pyramidal neurons, which provide the excitatory output signals of the layer, and the stellate cells, which act as inhibitory interneurons. The strong vertical coupling between cortical layers permits, as a first approximation, the treatment of the three-dimensional cortex as a two-dimensional vertical sheet. Moreover, if we are considering patterns of activity to be small relative to the size of the cortex, then it is reasonable to consider the sheet as infinite (\mathbb{R}^2) in order to facilitate mathematical analysis.

2.2 Mathematical Models: Cellular Level

To understand models representing populations of neurons, we develop equations, that describe the *subcellular* behavior of neurons, then proceed to integrate different aspects of this behavior into *systems* of coupled neurons, with the natural extension to a neuronal continuum. The resulting models form the basic classes of equations that we will use to study populations of synaptically coupled neurons, by applying both mathematical analysis and numerical simulation.

We begin by describing the fundamental governing equation of the individual neuron based on the capacitive properties of the membrane and the ion channels within the membrane. Subsequently, we extend this to include *synaptic currents*, the currents due to interneuronal connection. Finally, we briefly discuss axonal and dendritic effects, in a simplified context, suited to the neuronal population framework.

2.2.1 Membrane and Ion Channels

Neurons, like other cells, contain ions and molecules, which carry positive or negative charge. For the most part, the net charge within a neuron is negative, and, due to the fact that the intracellular space is a conductor, free charges, e.g., ions, repel each other and collect on the interior surface of the membrane. The cell membrane, a bilipid layer approximately 3-4 nm thick and impermeable to most ions, acts as a capacitor, separating charges lying on the inner and outer surfaces. However, embedded into this bilipid layer are numerous channels that permit ions to pass from the intracellular space to the extracellular space, or vice versa. These ion-conducting channels usually permit a single type of ion, and the flow of molecules though these channels can be modulated by many factors, including transmembrane potential (voltage-gated ion channels), concentration of intracellular messengers (Ca²⁺-dependent ion channels), and the extracellular concentration of neurotransmitters and neuromodulators (synaptic receptor channels) [21]. In addition there are a number of pumps which, by consuming energy, aid in maintaining concentration gradients of ions across the cell membrane.

Transmembrane potential, the potential difference across the membrane, is

$$V = V_i - V_e,$$

where V_i and V_e denote the intracellular and extracellular potentials, respectively. Due to intracellular resistance to current flow, transmembrane potential can vary substantially depending upon the location of measurement, especially during the course of an action potential. However, in situations where spatial

variation of transmembrane potential is not thought to be important, the neuron can be represented as a *compartment*, whereby a single value, varying in time, defines the potential of the whole neuron. Consider the soma as a compartment with uniform membrane potential V with excess charge Q on the inside surface and equal, but opposite, charge on the outside surface. We can then define membrane capacitance C_m by

$$C_m = \frac{Q}{V}. (2.1)$$

Since capacitance is proportional to the total surface area of the cell, we can define the specific capacitance, or capacitance per unit area, a useful quantity that is approximately the same for all neurons, $c_m \approx 10 \text{ nF/mm}^2$. Differentiating (2.1) with respect to time we obtain

$$C_m \frac{dV}{dt} = \frac{dQ}{dt},\tag{2.2}$$

which describes how a current $\frac{dQ}{dt}$ entering into the cell changes the transmembrane potential of the cell. We can rewrite this equation as

$$C_m \frac{dV}{dt} = I_{\text{ion}}(t), \tag{2.3}$$

where I_{ion} denotes all such ionic currents.

Next we must determine which ionic currents are responsible for dominant changes in membrane potential and how to model these currents. We begin by defining what is known as the Nernst or reversal potential. There are two factors governing the movement of charged particles, electric potential gradient and concentration gradient. Positive (negative) charges flow down (up) potential gradients and down (down) concentration gradients. Consider the situation where we have a species of ion, say Q, with a positive charge and with different concentrations on either side of a membrane. If ion-specific channels, specific to ion Q, open, then Q ions will flow across the membrane, due to the concentration gradient. This will cause an increase in positive charge building on the membrane, resulting in an increase of the transmembrane potential. Consequently this will make it increasingly difficult for more Q charges to traverse the membrane. The flow of ions will stop when the flow due to diffusion exactly balences the flow due to the electric potential gradient. The corresponding potential is referred to as the Nernst potential; the synonym, reversal potential, refers to the fact that a departure from that potential results in either an positive (inward) or negative (outward) current.

The reversal potential is given by

$$V_{\mathbf{Q}} = \frac{RT}{zF} \ln \left(\frac{[\mathbf{Q}]_e}{[\mathbf{Q}]_i} \right),$$

where the $[Q]_i$ and $[Q]_e$ denote the intracellular and extracellular concentrations of the ion Q, R the universal gas constant, F Faraday's constant, T the absolute temperature, and z the charge on the ion Q [59]. The number of ions that cross the membrane is small relative to the total number of ions in either the intra- or extracellular space, which allows us to assume that the concentrations do not change. This maintains electroneurality, disregarding the charge that builds on the interface. It also allows us to assume that the reversal potential is constant, a helpful simplification that spares us from explicitly keeping track of the ion concentrations.

Heuristically, we define the current-voltage relation in Ohmic fashion as

$$I_{\rm Q} \propto g_{\rm Q}(V-V_{\rm Q},)$$

where $g_{\rm Q}>0$ represents the *conductance* or inverse resistance. In this case, if $V-V_{\rm Q}>0$ ($V-V_{\rm Q}<0$), a positive charge will flow out of (into) the cell as the cell approaches the equilibrium value of the reversal potential. Conversely, this situation is reversed in the case of negative ions. Since we wish to define a positive current as positive charge moving into the cell, we take

$$I_{Q} = -g_{Q}(V - V_{Q}),$$

= $g_{Q}(V_{Q} - V)$

with the same form but opposite sign in the case of negative charge. For most ion channels, g_Q is a dynamic quantity, which, for example, depends on transmembrane potential in the case of voltage-dependent ion channels. This is where the excitable properties of neural tissue arise. The conductance g_Q often is written as the product of a constant maximal conductance, \bar{g}_Q , and a function of one or more dynamical variables which describe the opening and closing of gates of the channels. Much experimental and theoretical work has been devoted to understanding these currents. In 1952 Hodgkin and Huxley [47] pioneered a set of experimental methods to determine the functional dependence of the dynamically evolving, ionic permeability of the membrane on transmembrane potential in the squid axon. Their Nobel prize winning work established the most convincing and thorough evidence for the mechanism of neural excitability, by relating the excitability of the membrane and its ionic permeability to an explicit set of nonlinear equations and, furthermore, demonstrating the ability of their equations to generate familiar neuroelectric phenomena, such as action potentials, via, then arduous, numerical simulation.

In the case of the squid giant axon, studied by Hodgkin and Huxley [47, 59], the currents were determined to be

$$\begin{split} I_{\rm ion} &= I_{\rm Na} + I_{\rm K} + I_{\rm L}, \\ I_{\rm Na} &= \bar{g}_{\rm Na} m^3 h(V_{\rm Na} - V), \\ I_{\rm K} &= \bar{g}_{\rm K} n^4 (V_{\rm K} - V), \\ I_{\rm L} &= \bar{g}_{\rm L} (V_{\rm L} - V), \\ \bar{g}_{\rm Na} &= 120; \qquad \bar{g}_{\rm K} = 36; \qquad \bar{g}_{\rm L} = 0.3; \\ V_{\rm Na} &= 115; \qquad V_{\rm K} = -12; \qquad V_{\rm L} = 10.6, \end{split}$$

where $I_{\rm Na}$ and $I_{\rm K}$ represent the inward sodium and outward potassium currents, respectively, and $I_{\rm L}$ is a leak current representing all approximately linear currents. Transmembrane potential and reversal potentials are measured in mV, the conducances \bar{g}_i are in units of mS/cm², and the capacitance C is in μ F/cm². Note, Hodgkin and Huxley chose $V_{\rm L}$ such that the resting transmembrane potential of the cell would be zero, but, in general, it is around -70 mV [47, 59]. This means the cell membrane is polarized, in which case, currents tending to increase the transmembrane potential are termed depolarizing, while currents tending to decrease the transmembrane potential are called hyperpolarizing. In the Hodgkin-Huxley model, the Na⁺-current, initially, depolarizes the cell, thereby exciting it, and, subsequently, the K⁺-current hyperpolarizes the cell, driving it towards its resting negative value.

The gating variables m, n, h, which describe the dynamics of the opening and closing of channel gates, are modeled as voltage-dependent by

$$\frac{dw}{dt} = \alpha_w(V)(1-w) + \beta_w(V)w, \qquad w \in \{m, n, h\}.$$

The important feature of this model is the threshold behavior of the membrane potential. The threshold behavior can be seen in (2.3) and (2.4), by noticing that, since the change in potential is proportional to $I_{\rm ion}$, for small deviations of V above the resting potential, $I_{\rm ion} < 0$ resulting in the membrane potential's return to rest, whereas, for sufficiently large positive deviations, $I_{\rm ion} > 0$ resulting in a dramatic autocatalytic increase before returning to rest. As mentioned earlier, this excursion in the transmembrane potential of the cell is called an action potential and is illustrated in Figure 2.1 for the Hodgkin-Huxley model. Neurons differ widely in their ion channel properties and types. However, many neurons behave in a qualitatively similar way to the Hodgkin-Huxley model, in which case it can be used as an archetype. An example of another type of behavior not supported by the Hodgkin-Huxley model is bursting, whereby the cell periodically alternates between a mode of rapid firing (the burst) and a quiescent interval.

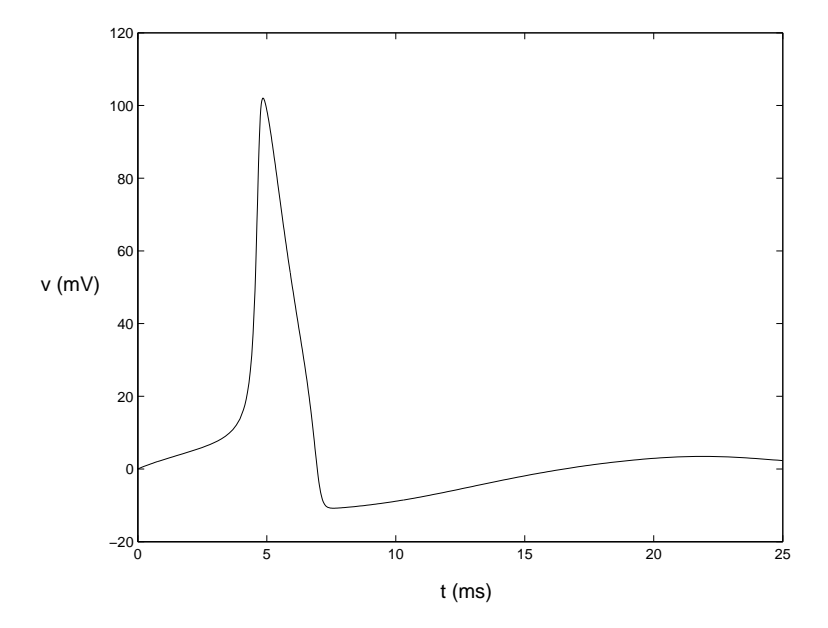


Figure 2.1. Action Potential for the Hodgkin-Huxley model.

2.2.2 Synapses

We model synaptic currents as described in section 2.1.1, i.e.,

$$I_{\text{syn}} = g_{\text{syn}}(t)(V_{\text{syn}} - V),$$

since they too are generated by the opening of ion channels. Synaptic currents form the basis of one of the primary topics of this dissertation—the effect of *synaptic connectivity* of neurons.

Synaptic transmission at a spike-mediated chemical synapse begins when an action potential invades the presynaptic terminal bouton and activates voltage-dependent Ca²⁺ channels, leading to a rise in the concentration of Ca²⁺ within the terminal. This causes vessicles containing neurotransmitter molecules to fuse with the cell membrane and release their contents into the synaptic cleft between the pre- and postsynaptic neurons. Binding of the transmitter molecules leads to the opening of ion channels that modify the conductance of the postsynaptic neuron, completing the transmission. Postsynaptic ion channels can either be directly activated by binding to the transmitter (ionotropic receptors) or indirectly when the transmitter binds to a distinct

receptor that affects ion channels through an intracellular second-messenger signaling pathway (metabotropic receptors). This second class is often referred to as neuromodulation and is associated with neurotrasmitters such as serotonin, dopamine, norepinephrine and acetylcholine, which have a variety of important effects on the functioning of the nervous system [67, 21].

Synaptic connections can either be excitatory or inhibitory: if the effect is to increase (decrease) the probability that the postsynaptic cell fires, it is classified as excitatory (inhibitory). Hence, the effect of a specific neurotransmitter can be either excitatory or inhibitory, depending on which receptors are activated. In addition, synaptic transmission falls into two broad classes based on time-course: fast transmission, which is associated with ionotropic receptors, and slow transmission, which is associated with metabotropic receptors. The time-scale of the synapse will enter as an additional parameter(s) in our models and can be used to distinguish different types of synapses. When associated with AMPA receptors, glutamate is the dominant fast, excitatory neurotransmitter in the central nervous system, though when associated with NMDA receptors its effect is slow. Conversely, GABA_A is the dominant, fast, inhibitory neurotransmitter whereas GABA_B is slow [67, 9, 21].

Single-channel recording techniques have been used to show that voltage-dependent currents arise from populations of individual ion channels undergoing rapid transitions between conducting and nonconducting states. The macroscopic behavior of these currents can be accurately captured by using kinetic models that describe transitions between conformational states of these ion channels. These types of models, of which Hodgkin-Huxley is an example, are called Markov models [61, 22]. Although one can bring great detail into these models by describing many different states, the essential properties of ion channel activation can be captured by simplified kinetic models with two states. This helps to simplify mathematical analysis and numerical computation in models that do not require the detail of multistate models.

The simplest model describing the states for a receptor channel is

$$O \stackrel{k_+(V,[T])}{\rightleftharpoons} C,$$

where O and C represent the open and closed states of the channel, [T] the neurotransmitter concentration, and k_+, k_- the voltage-dependent forward and backward rate constants [61, 22]. If s denotes the fraction of receptors in the open state, then it evolves by the first-order kinetic equation

$$\frac{ds}{dt} = k_{+}[T](1-s) - k_{-}s. \tag{2.5}$$

Letting the system be in the inital state, $s = s_0$ with $V = V_0$ and $[T] = [T]_0$ for $t < t_0$, assume an instantaneous change in [T] and V occurs such that for $t > t_0$, both $[T] = [T]_1$ and $V = V_1$. In this case (2.5) yields

$$s(t - t_0) = s_{\infty} + (s_0 - s_{\infty}) \exp\left(\frac{-(t - t_0)}{\tau}\right)$$
 (2.6)

where

$$s_{\infty} = \frac{k_{+}(V_{1}, [T]_{1})}{k_{+}(V_{1}, [T]_{1}) + k_{-}(V_{1})},$$
$$\tau = \frac{1}{k_{+}(V_{1}, [T]_{1}) + k_{-}(V_{1})}.$$

A synaptic current could then be described by

$$I_{\text{syn}}(t - t_0) = \bar{g}_{\text{syn}}s(t - t_0)(V_{\text{syn}} - V), \tag{2.7}$$

where $I_{\text{syn}} = 0$ for $t < t_0$ and t_0 represents the time at which an action potential in the presynaptic neuron causes the release of neurotransmitter. Another important, slightly more complex scheme is the second order gating scheme:

$$\begin{array}{ccc}
C & \stackrel{r_1([T])}{\rightleftharpoons} & C_1 \\
& \stackrel{r_2}{\swarrow} & \swarrow r_3 \\
& O & & & & & & \\
\end{array}$$

where C, C_1 are closed states, O is the opened state, and r_1 , r_2 , r_3 , r_4 are voltage-independent rate constants. Assume transmitter concentration [T] occurs as a δ -function, with a release event occuring at $t = t_0$, i.e.

$$r_1([T]) = \hat{r}_1 \delta(t - t_0).$$

Also, assume that the state C is always considered to be in excess when compared with C_1 and O. This would occur if very few receptors bind transmitter, so that nearly all receptor molecules remain in form C. The fraction of channels in state C is therefore considered constant and approximately equal to 1. This yields the following system of equations

$$\frac{dc}{dt} = r_1 \delta(t - t_0) - (r_2 + r_3)c, \tag{2.8}$$

$$\frac{ds}{dt} = r_3 c - r_5 s, (2.9)$$

where c, s represent the fraction of receptors in the form C_1 and O, respectively.

The solution of this system is

$$s(t - t_0) = r_1 r_3 \frac{\exp\left(-\frac{(t - t_0)}{\tau_1}\right) - \exp\left(-\frac{(t - t_0)}{\tau_2}\right)}{\frac{1}{\tau_2} - \frac{1}{\tau_1}},$$
 (2.10)

where $\tau_1 = \frac{1}{r_2 + r_3}$ and $\tau_2 = \frac{1}{r_4}$. This function has the feature that the rise time and decay time are independent. However, letting $\tau_2 \longrightarrow \tau_1$ (or $r_4 \longrightarrow r_2 + r_3$) equation (2.7) becomes

$$s(t - t_0) = r_1 r_3(t - t_0) \exp\left(-\frac{(t - t_0)}{\tau_1}\right),$$
 (2.11)

which is the so-called α -function introduced in 1967 by Rall [21]. This function has the nice property of being a smooth function, resembling the time course of the synaptic gating variable, which can replace the synaptic gating variable to simplify mathematical analysis or numerical computation. However, in the scheme described above, it is technically valid for $s \ll 1$.

2.2.3 Axons and Dendrites

To complete the story, one can construct models that include great detail in the branching structure of dendrites and the gating dynamics of the ion channels responsible for action potential generation along axons. However, our goal is to construct models that describe the behavior of populations of neurons and facilitate mathematical analysis; hence we must restrict the level of detail. The Hodgkin-Huxley ODE model represents a patch of membrane in the squid axon [47, 59]. In a spatial Hodgkin-Huxley continuum PDE model, which would describe conduction along an infinite axon, there exists a constant speed traveling pulse, or action potential [59]. We can incorporate this information into the α -function (2.11), or any other function representing the synaptic time course, as an axonal delay τ_a . Axonal delay should depend on the distance the signal travels to reach the postsynaptic neuron, e.g.

$$\tau_a = \tau_d + \frac{x - y}{c_a},\tag{2.12}$$

where τ_d is a constant delay and c_a is the axonal conductance velocity [38]. As a first approximation, we can neglect the axonal delay in the case of traveling waves, which are slow relative to the axonal conduction velocity. Experimentally, action-potential propagation along a cortical axon is roughly 2-4 m/s [80], which is two orders of magnitude faster than the wave speed measured in cortical tissue, 20-100 mm/s [15]. However, we should mention that axonal delay does have nontrivial consequences for traveling waves.

In the case of dendrites, we consider the diffusive spreading of potential, and, to first approximation, we take dendritic conduction to be instantaneous. However, as mentioned earlier, some dendritic trees possess active ion channels and, furthermore, can be quite extensive, indicating that time delays due to synapses on distal branches may be important. Bressloff derived a factor to include the passive dendritic effects in terms of the spacetime Greens function. If y is the location of synaptic current input on the dendrite at time t, then the effective synaptic current entering the soma is given by

$$G(y,t) = \frac{e^{-t/\tau_d}}{\sqrt{\pi Dt}} e^{-y^2/4Dt} H(t), \qquad (2.13)$$

where τ_d is the membrane time constant of the cable, D is the diffusivity, and H is the Heaviside function [5, 7].

2.3 Mathematical Models: Systems Level

We move now to a description of models at the systems level, since we wish to analyze the behavior of populations of neurons rather than individual cells. We have discussed the many modes of transmission for a neural signal and incorporated these into mathematical models. The following subsections offer heuristic derivations of three different classes of models that are studied when considering spatiotemporal structures of neural activity. We begin with models that incorporate the most biophysical detail and follow with two simplifications that capture different aspects of the first class. The *integrate-and-fire* models assume that the shape and time course of the action potentials of a cell are not as important as the timing of these events and the dynamics between them; consequently, the action potential is replaced by an *instantaneous* spike, which, in appropriate cases, can be represented by a δ -function. The *rate models*, on the other hand, assume that the individual spikes of a neuron can be replaced by smooth neuronal firing rate. Rate models will be the focus of this dissertation.

2.3.1 Biophysical Models

When considering a population of neurons, we couple individual neurons synaptically to construct a *network*. Assume we have N neurons synaptically coupled together, each of which is represented by a single compartment. The transmembrane potential V_i of the i^{th} cell evolves according to

$$C_m \frac{dV_i}{dt} = I_i^{\text{ion}}(t) + I_i^{\text{syn}}(t), \qquad (2.14)$$

where $I_i^{\rm syn}$ denotes the total synaptic current entering into cell i, and $I_i^{\rm ion}$ denotes the voltage-dependent membrane currents entering cell i. We shall assume that the form of the current can be described by a relation of the form

$$I = g(t)(V_r - V), \tag{2.15}$$

where g represents a time-dependent conductance and V_r is the reversal potential associated with the channels. In particular, we use the Hodgkin-Huxley model, discussed in section 2.2.1, to describe the neuronal membrane dynamics as a four-dimensional dynamical system; implicit in this assumption is that the membrane properties of the neurons in the population are identical. At this point different currents and dynamics can be included to represent different types of neurons, though we do not consider this here.

The synaptic current into cell i from the firing of cell j is modeled by

$$I_{ij} = \bar{g}_{ij} s_{ij} (V_{ij}^{\text{syn}} - V),$$

where \bar{g}_{ij} denotes the total synaptic conductance from cell j to cell i, s_{ij} denotes the synaptic gating variable associated with the synapsing of the cell j onto cell i, and $V_{ij}^{\rm syn}$ is the corresponding reversal potential. The structure of the connection strength between any two cells is determined by g_{ij} and is zero, if two cells are not connected. The full model is then:

$$C_{m} \frac{dV_{i}}{dt} = I^{\text{HH}}(m_{i}, n_{i}, h_{i}, t) + \sum_{k=1}^{N} \bar{g}_{ik} s_{ik} (V_{ik}^{\text{syn}} - V),$$

$$\frac{dw_{i}}{dt} = \alpha_{w}(V_{i})(1 - w_{i}) - \beta_{w}(V_{i})w_{i}; \qquad w \in \{m, n, h\} \qquad (2.16)$$

$$\frac{ds_{ij}}{dt} = \alpha_{s_{ij}}(1 - s_{ij}) - \beta_{s_{ij}} s_{ij},$$

where $i, j \in \{1, ..., N\}$, $I_i^{\text{HH}}(m, n, h, t)$ denotes the membrane current for the Hodgkin-Huxley model, α_w, β_w represent the opening and closing rates for the ion channels associated with the Hodgkin-Huxley dynamics, and $\alpha_{s_{ij}}, \beta_{s_{ij}}$ represent the opening and closing rates associated with the synapse made from cell j to cell i.

To reduce this model to a lower order dynamical system, we make a number of preliminary simplifications. We assume the synaptic gating dynamics from cell j to any cell i are completely described by a single gating variable associated with cell j, i.e.,

$$s_{ij} = s_j$$
.

Second we assume that the synaptic reversal potential associated with the synapse from cell j to cell i is independent of the presynaptic cell,

$$V_{ik}^{\text{syn}} = V_{i}^{\text{syn}}$$
.

This reduces (2.16) to the simplified model

$$C_{m} \frac{dV_{i}}{dt} = I^{\text{HH}}(m_{i}, n_{i}, h_{i}, t) + \sum_{k=1}^{N} \bar{g}_{ik} s_{k} (V_{i}^{\text{syn}} - V),$$

$$\frac{dw_{i}}{dt} = \alpha_{w}(V_{i})(1 - w_{i}) - \beta_{w}(V_{i})w_{i}; \qquad w \in \{m, n, h\} \qquad (2.17)$$

$$\frac{ds_{i}}{dt} = \alpha_{s_{i}}(1 - s_{i}) - \beta_{s_{i}} s_{i}; \qquad i \in \{1, ..., N\},$$

where, for example, we take the opening and closing rates of the synaptic ion channels to be

$$\alpha_{s_i} = K(V_i) = \frac{K_0}{1 + \exp\left(\frac{V_i - V_T}{V_s}\right)},$$

$$\beta_{s_i} = \beta.$$

In this case as V_i crosses threshold V_T , $K(V_i)$ is large and s_i rises almost to 1 at a rate proportional to K_0 . After the action potential concludes, s_i decays to 0 with time constant β^{-1} . This was first introduced by Wang and Rinzel [105] and theoretically justified by Destexhe et al. [22, 24]. This model has been used elsewhere by Golomb et al. [36] and constitutes a variation of the biophysical model used in numerical simulations in Chapter 4.

Next, we introduce spatial dependence into the model in order to investigate the types of spatial patterns of activity generated by such systems of equations. At this point we have been ambiguous about the location of neurons in space and very general about the synaptic conductances that define the strength of synaptic connection between neurons. Though in general we are thinking of neurons in \mathbb{R}^3 , as mentioned at the end of section 2.1, most mathematical treatments consider two-dimensional ordered populations of neurons on a sheet, due to the strong vertical coupling between cortical layers. In the case of thin vertical cortical slices, which are studied in vitro, this can further be reduced to a one-dimensional line of neurons. Though most of the horizontal connections are lost in such slices, it is believed that much of the vertical connectivity is preserved. The strong coupling of the vertical connections between the cortical layers causes the neurons along a vertical line to fire together. The vertical line can be collapsed to a point, reducing the domain to a one-dimensional line. Now we can define some sort of structure for \bar{g}_{ij} . It is reasonable to assume, as a first approximating assumption, that the strength of connection between two neurons depends only on the distance between those neurons, i.e.,

$$\bar{g}_{ij} = g(|i-j|),$$

in particular, that g decreases with distance. Although there is evidence to support this assumption in local neighborhoods of neurons within the cortex and

other brain regions, it is not necessarily valid outside of these neighborhoods. Note, we use the terms *homogeneous* and *isotropic* to describe the synaptic connectivity functions. These are defined in one dimension as

$$w(x,y) = \mathcal{W}(x-y)$$
 (homogeneous)
 $w(x,y) = \mathcal{W}(|x-y|)$ (homogeneous, isotropic)

where homogeneous is synonymous with translationally invariant.

As mentioned earlier, we are interested in continuum models of neuronal populations: assuming that we can define smooth functions V, s, w satisfying (2.18) and assuming that g scales proportionally to the distance between neurons, we can approximate (2.17) by the continuum equations:

$$C_{m} \frac{\partial V}{\partial t}(x,t) = I^{\text{HH}}(m,n,h,t) + \int_{-\infty}^{\infty} g(|x-y|)s(x,t)(V_{\text{syn}} - V(x,t)),$$

$$\frac{\partial w}{\partial t}(x,t) = \alpha_{w}(V)(1 - w(x,t)) - \beta_{w}(V)w(x,t); \qquad w \in \{m,n,h\},$$

$$\frac{\partial s}{\partial t}(x,t) = \alpha_{s}(1 - s(x,t)) - \beta_{s}s(x,t), \qquad (2.18)$$

where we have made the additional simplifications that the synaptic reversal potential and the channel opening and closing rates are identical for all neurons,

$$V_i^{\text{syn}} = V_{\text{syn}}, \qquad \alpha_{s_i} = \alpha_s, \qquad \beta_{s_i} = \beta_s,$$

and that g(z) is a positive function, symmetric in z, and monotonically decreasing for z>0, e.g., $\mathrm{e}^{-|z|/\sigma}$ or $\mathrm{e}^{-(z/\sigma)^2}$. Even with the numerous simplifications we have made, this biophysical model is still very difficult to study analytically; instead it will be one of the primary models that will be simulated numerically to compare with the analytical and numerical results of the rate models.

Another common simplification is to assume that the time-course of the synaptic variable is specified by a function

$$s_i = \alpha ((t - t_i)^+),$$

where

$$(\tau)^{+} = \begin{cases} \tau & \tau > 0, \\ 0 & \text{otherwise,} \end{cases}$$
 (2.19)

rather than evolving according to a differential equation. Here t_j is the firing time of cell j, and $\alpha(t)$ is some type of α -function, e.g., $\beta e^{-\beta t}$, $\beta^2 t e^{-\beta t}$, or $\frac{e^{-t/\tau_1} - e^{-t/\tau_2}}{\tau_1 - \tau_2}$ [24]. This simplification has been used in many numerical and analytical treatments of neuronal network models [7, 38, 37, 24], and we shall apply it both to the integrate-and-fire and rate models. From this point on, the symbol α will be used to denote any such function that explicitly describes the synaptic time course.

2.3.2 Integrate-and-Fire Population Model

The integrate-and-fire class of models arises from the assumption that the actual shape and time course of the action-potential are not important and, consequently, can be disregarded, allowing us to discard the membrane ionic currents. Before the mechanisms that generate action-potentials were understood, Lapicque first introduced this type of model in 1907 in order to generate spikes [21]. We retain the linear leakage current term to model the membrane conductance, a good approximation for subthreshold transmembrane potential in some neurons [21]. We define a threshold value of transmembrane potential V_{th} such that, if the transmembrane potential reaches the threshold from below, the neuron fires an instantaneous spike and the transmembrane potential is reset to some value $V_{\rm reset}$. With this in mind, it is reasonable to assume that

$$V_{\text{syn}} - V(x, t) \approx V_0^{\text{syn}},$$

where V_0^{syn} is a constant since it varies substantially only during the action-potential, which has been collapsed into an instant of time. For simplicity, define the constant g_{syn} and weight function w such that

$$g(z) = g_{\text{syn}} w(|z|),$$

where w is positive and symmetric, monotonically decreasing in |z|, and normalized in some sense such that the parameter g_{syn} measures the full weight of the strength of synaptic connection. If we also allow the time course of the synaptic gating variable to be described as the α -function, and let T(x) denote the time at which $V(x, T(x)^-) = V_{th}$, the model becomes

$$C_{m} \frac{\partial V}{\partial t}(x,t) = \bar{g}_{L}(V_{L} - V(x,t)) + \bar{g}_{\text{syn}}V_{0} \int_{-\infty}^{\infty} w(|x-y|)\alpha(t-T(y))dy,$$

$$\mathbf{if} \quad V(x,t^{-}) = V_{th} \quad \mathbf{then} \quad V(x,t^{+}) = V_{\text{reset}}. \tag{2.20}$$

We can nondimensionalize this equation by defining the following

$$v = rac{V_L - V}{V_0},$$
 $v_{th} = rac{V_L - V_{th}}{V_0},$ $v_{ ext{reset}} = rac{V_L - V_{ ext{reset}}}{V_0},$ $g_{ ext{syn}} = rac{ar{g}_{ ext{syn}}}{ar{g}_L},$ $au = g_L C_m,$

to obtain the integrate-and-fire model:

$$\begin{cases}
\tau \frac{\partial v}{\partial t}(x,t) = -v(x,t) + g_{\text{syn}} \int_{-\infty}^{\infty} w(|x-y|)\alpha(t-T(y))dy, \\
\text{if} \quad v(x,t^{-}) = v_{th} \quad \text{then} \quad v(x,t^{+}) = v_{\text{reset}}.
\end{cases}$$
(2.21)

2.3.3 Rate Models

Rate models contrast the integrate-and-fire neuron by representing the output of a neuron in terms of a smooth firing rate function rather than a spike train which contains the precise firing times of the neuron. Suppose the total synaptic current entering cell i is given by

$$u_i(t) = \sum_k g_{ik} \alpha(t - T_k^m) (V_{ik}^{\text{syn}} - V_k),$$
 (2.22)

where g_{ik} is the synaptic conductance from cell k to cell i, T_k^m is the m^{th} firing time of cell k, α is any α -function, V^{syn} is the reversal potential associated with the synaptic ion channels, and V_k is the membrane potential of cell k. This sum can be defined over finitely or infinitely many neurons. However, in the infinite case we restrict the functions g such that this sum is finite for all i. Since we are considering a time-scale much greater than the duration of an action-potential, we make the approximation that

$$V_{ik}^{\text{syn}} - V_k \approx V_{ik}^0$$

where V_{ik}^0 is a constant. We can then define function

$$w_{ik} = g_{ik}V_{ik}^0$$

which can generate excitatory or inhibitory connections between neurons, as V^0 can be positive or negative. Moreover, supposing the firing times of neuron j can be written as a sequence of δ -function spikes

$$\rho_j(\tau) = \sum_{m \in \mathbb{Z}} \delta(\tau - T_j^m),$$

we can rewrite (2.22) as

$$u_i(t) = \sum_k w_{ik} \int_{-\infty}^t \alpha(t - \tau) \rho_k(\tau) d\tau.$$
 (2.23)

At this point, we wish to replace the sequence of spikes by a smooth firing rate function, $a_k(t)$, which is justified only if relevant network quantities are relatively insensitive to trial-to-trial fluctuations in spike-trains. Experiments depict that the trial-to-trial variability in neuronal spiking is often large, suggesting that the replacing of the exact spike train by a firing rate in this context would be invalid. However, if a neuron receives uncorrelated inputs from a large number of cells, the mean of the total input grows linearly with the total number of synapses, whereas the standard deviation grows as the square

root of the total number of synapses; this suggests that the replacement by a firing rate becomes more accurate as the number of synapses increases. This is not true if the inputs are indeed correlated, which occurs, for example, if presynaptic neurons fire synchronously. In addition temporal averaging, due to slow synapses and membrane and dendritic effects, can reduce the spike-train variability, lending support for the replacement by firing rate [21, 9]. With these considerations in mind, we let $\alpha(\tau) = (\frac{1}{\tau_s} e^{-\tau/\tau_s})^+$ and replace the exact spike train ρ_k by a smooth firing rate a_k ; subsequently, differentiating

$$u_i(t) = \sum_k w_{ik} \int_{-\infty}^t \alpha(t - \tau) a_k(\tau) d\tau.$$
 (2.24)

with respect to t, yields

$$\tau_s \frac{du_i}{dt}(t) = -u_i(t) + \sum_k w_{ik} a_k(t).$$
(2.25)

In order to close the system, we must determine a relationship between the firing rate a_i of a neuron and the total current input u_i into that neuron. Neurons fire at a steady rate given a constant current injection, a property found both in experiments with real neurons as well as in numerical experiments with biophysical or integrate-and-fire neurons. Moreover, the firing rate is ideally a monotonically increasing, bounded function, as neuronal firing tends to saturate with increasing current injection. Let F(u) denote the *steady-state* firing rate in terms of input curent u where F is a bounded, smooth, monotonically increasing, positive function, e.g., logistic function or hyperbolic tangent. If a neuron is firing in steady-state, we take

$$a_i = F(u_i). (2.26)$$

However, the firing rate is directly related to the intrinsic membrane properties of the neuron and, in general, evolves dynamically with respect to fluctuations in the membrane potential and synaptic current. Often the firing rate dynamics are taken to evolve according to a first-order differential equation in time, assuming that it evolves in a fashion similar to the cell membrane. Some venture as far to say that the time constants are the same; however, there is no reason to expect this since the dynamics are not the same [21]. Supposing the first-order dynamics are appropriate, then we allow the firing rate to approach the steady-state firing rate, with time constant τ_m , yielding the system,

$$\begin{cases}
\tau_s \frac{du_i}{dt}(t) = -u_i(t) + \sum_k w_{ik} a_k(\tau), \\
\tau_m \frac{da_i}{dt}(t) = -a_i(t) + F(u_i(t)).
\end{cases}$$
(2.27)

Two limits allow us to simplify this system further: $\tau_s \gg \tau_m$ and $\tau_m \gg \tau_s$.

Suppose $\tau_s \gg \tau_m$, then if we scale time by

$$\tau = \frac{t}{\tau_s},$$

the system becomes

$$\begin{cases}
\frac{du_i}{d\tau}(\tau) = -u_i(\tau) + \sum_k w_{ik} a_k(\tau), \\
\epsilon \frac{da_i}{d\tau}(\tau) = -a_i(\tau) + F(u_i\tau),
\end{cases} (2.28)$$

where $\epsilon = \frac{\tau_m}{\tau_s} \ll 1$. Since we have a small parameter, we can take the second equation in (2.28) to be in quasi-steady state, i.e.,

$$a_i(\tau) = F(u_i(\tau)).$$

Substituting this into the first equation of (2.28), we obtain

$$\frac{du_i}{d\tau}(\tau) = -u_i(\tau) + \sum_k w_{ik} F(u_k(\tau)), \qquad \tau_s \gg \tau_m.$$
 (2.29)

Conversely, if $\tau_m \gg \tau_s$, the analogous argument yields

$$\frac{da_i}{d\tau}(\tau) = -a_i(\tau) + F\left(\sum_k w_{ik} a_k(\tau)\right), \qquad \tau_m \gg \tau_s.$$
 (2.30)

The assumption $\tau_s \gg \tau_m$ means the firing rates instantaneously follow time-varying inputs, while $\tau_m \gg \tau_s$ implies that the synaptic time course is negligible and synaptic current dynamics are instantaneous. One method to determine when the first assumption is valid is to consider the firing rate in an integrate-and-fire model subject to a time-varying current injection. Chance [14, 21] did this experiment with $I(t) = I_0 + I_1 \cos(\omega t)$ as an input current and found that, if the time-independent portion of the current I_0 was sufficiently large that it maintained fairly rapid firing of the cell, the steady-state $a_i(\tau)$ $F(u_i(\tau))$ successfully describes the behavior of the time-dependent firing rate for many different frequencies ω . However, if during the oscillation cycle, the input current is significantly below the threshold, the firing rate dynamics are delayed and attenuated at high frequencies. This discussion pertains to a single cell, whereas we have input from many cells converging on a single cell. Suppose a wave of activity is passing across a line of neurons, neurons ahead of the wave will receive input, since the range of synaptic inputs is non-local; one could imagine that this total input might be large enough that (2.26) is valid.

Another argument in support of (2.26) is that, if the rate of change of the total synaptic input

$$\sum_{k} w_{ik} F(u_k(\tau))$$

is slow, then $\frac{da_i}{dt}$ is small and the firing rate is approximately at steady-state. One could also imagine that an approaching wave could increase the synaptic input into cells ahead of the wave slow enough that (2.26) is valid. It would be interesting to examine the validity of this assumtion in the case of traveling waves by comparing, numerically, the full system (2.28) with the reduced system (2.29) for different parameter values, in particular ϵ .

By the same continuum approximation described previously, we obtain the continuum version of these equations:

$$\frac{\partial u}{\partial \tau}(x,\tau) = -u(x,\tau) + \int_{-\infty}^{\infty} w(x,y) F(u(y,\tau)) dy, \qquad \tau_s \gg \tau_m. \quad (2.31)$$

Conversely, if $\tau_m \gg \tau_s$, we would have

$$\frac{\partial a}{\partial \tau}(x,\tau) = -a(x,\tau) + F\left(\int_{-\infty}^{\infty} w(x,y)a(y,\tau)dy\right), \qquad \tau_m \gg \tau_s. \quad (2.32)$$

For convenience we have only considered one type of neuron, but, as mentioned earlier, we are interested in considering populations of excitatory and inhibitory neurons. The difference arises in the sign of the term involving the reversal potential. In either case, excitation will have a positive effect by increasing the net synaptic input to a cell while inhibition will have a negative effect by decreasing the net synaptic input to a cell. If we take a rate model of the form (2.31), we can introduce individual excitatory and inhibitory populations as

$$\tau_e \frac{\partial u_e}{\partial t} = -u_e + w_{ee} * F_{ee}(u_e) - w_{ei} * F_{ei}(u_i), \qquad (2.33)$$

$$\tau_i \frac{\partial u_i}{\partial t} = -u_i + w_{ie} * F_{ie}(u_e) - w_{ii} * F_{ii}(u_i), \qquad (2.34)$$

where

$$\Big(w_{ab} * F_{ab}(u_b)\Big)(x) = \int_{-\infty}^{\infty} w_{ab}(x, y) F_{ab}\big(u_b(y, t)\big) dy,$$

e, i denote the excitatory and inhibitory populations respectively, and w_{mn} are positive synaptic weight functions from population n to population m. Since excitatory and inhibitory populations are different, we allow synaptic time constants, firing rates, and weight functions to be different. These two equations and variations thereof form a primary class of firing rate models for neuronal populations, and are essentially the Wilson-Cowan equations introduced in 1973 [108, 109].

CHAPTER 3

ON FRONT BIFURCATIONS IN AN EXCITATORY NEURAL NETWORK

Consider the system of integrodifferential equations

$$\tau_s \frac{\partial u}{\partial t}(x,t) = -u(x,t) + \int_{-\infty}^{\infty} w(x-x') f(u(x',t)) dx' - \beta v(x,t) + I(x)$$

$$\frac{1}{\epsilon} \frac{\partial v}{\partial t}(x,t) = -v(x,t) + u(x,t), \tag{3.1}$$

representing a continuum model of one-dimensional cortical tissue, in which u(x,t) is a neural field that represents the local activity of a population of excitatory neurons at position $x \in \mathbb{R}$, I(x) is an external input current, τ_s is a synaptic time constant (assuming first-order synapses), f(u) denotes the neuronal output firing rate function and w(x-x') is the strength of connections from neurons at x' to neurons at x. The synaptic weight distribution w(x) is taken to be a positive, even function of x, such that $\int_{\mathbb{R}} w(x) dx < \infty$. The neural field v(x,t) represents some form of local negative feedback mechanism such as spike frequency adaptation or synaptic depression, with β , ϵ determining the relative strength and rate of feedback. The nonlinear function f is usually taken to be a smooth sigmoid function, i.e. a bounded, smooth, monotonically increasing function, e.g.,

$$f(u) = \frac{1}{1 + e^{-\gamma(u - \kappa)}} \tag{3.2}$$

with gain γ and threshold κ . The units of time are fixed by setting $\tau_s = 1$; a typical value of τ_s is 10 ms.

A number of previous studies have considered the existence and stability of traveling wave solutions of equation (3.1) in the case of a uniform input I, which is equivalent to a shift in the threshold κ . In particular, it has been shown that in the absence of any feedback ($\beta = 0$), the resulting scalar network

can support the propagation of traveling fronts [26, 49], whereas traveling pulses tend to occur when there is significant negative feedback [109, 1, 80]. In this chapter, we show that such feedback can also have a nontrivial effect on the propagation of traveling fronts, due to the occurrence of a symmetry breaking front bifurcation analogous to that found in reaction-diffusion systems [89, 43, 93, 44, 3, 91, 84, 66]. We begin by deriving conditions for the existence of traveling wavefronts in the case of a homogeneous network (section 3.1). We then carry out a perturbation expansion in powers of the wavespeed c to show that a stationary front can undergo a supercritical pitchfork bifurcation at a critical rate of negative feedback, leading to bidirectional front propagation (section 3.2). As in reaction-diffusion systems, the front bifurcation acts as an organizing center for a variety of nontrivial dynamics including the formation of oscillatory fronts or breathers. We show how the latter can occur through a Hopf bifurcation from a stationary front in the presence of a weak stationary input inhomogeneity (section 3.3). Finally, we analyze the existence and stability of stationary fronts in an exactly solvable model, obtained by taking the high gain limit $\gamma \to \infty$ of the sigmoid function f such that $f(u) = H(u - \kappa)$ where H is the Heaviside function (section 3.4). The exactly solvable model allows us to study oscillatory fronts beyond the weak input regime. Rather than perturbing about the homogeneous case, we now consider a large input amplitude for which wave propagation failure occurs, due to the pinning of a stationary front. A subsequent reduction in the amplitude of the input then induces a Hopf instability leading to the formation of a breather. We conclude our analysis of the exactly solvable model, by deriving conditions for the locking of a traveling front to a moving input and showing the dependence of locking on both the amplitude and speed of the input.

The major advantage of the exactly solvable model is that it allows us to determine explicitly the existence and stability of stationary and traveling fronts in the presence of external inputs, without any restrictions on the size of the input. Though, it has the disadvantage of restricting the nonlinear function f to a step function, which is less realistic than the smooth nonlinearity (3.2), matching quite well the input—output characteristics of populations of neurons. As we show in this chapter, such an analysis can be carried out for smooth f provided that the input amplitude is sufficiently weak. That the nonlocal integrodifferential equation (3.1) exhibits behavior similar to a reaction-diffusion system might not be surprising, particularly given that, for the exponential weight $w(x) = e^{-|x|}$, equation (3.1) can be reduced to a PDE of the reaction—diffusion type. It is important to emphasize, however, that our results hold for a more general class of weight distributions w(x) for which a corresponding (finite—order) PDE cannot be constructed. Hence, the analysis is a nontrivial extension of known results for reaction—diffusion equations.

3.1 Fronts in a Homogeneous Network

In this section we investigate the existence of traveling front solutions of equation (3.1) for homogeneous inputs, by combining results on scalar networks [26] with an extension of the analysis of front bifurcations in nonscalar reaction—diffusion equations [43, 3].

The scalar case. The existence of traveling front solutions in scalar, homogeneous networks was previously analyzed by Ermentrout and Mcleod [26]. Their analysis can be applied to a scalar version of equation (3.1) obtained by taking $\epsilon \to \infty$, so that v = u, and setting I(x) = -h with h a constant input. This leads to the scalar integrodifferential equation

$$\frac{\partial u}{\partial t}(x,t) = -(1+\beta)u(x,t) + \int_{-\infty}^{\infty} w(x-x')f(u(x',t))dx' - h. \tag{3.3}$$

Without loss of generality, we choose h such that $\kappa=0$ in the sigmoid function (3.2). The weight distribution w is assumed to be a positive, even, continuously differentiable function of x with unit normalization $\int_{\mathbb{R}} w(y)dy = 1$. Suppose that the function

$$F_{h,\beta}(u) = f(u) - (1+\beta)u - h \tag{3.4}$$

has precisely three zeros $u = U_{\pm}(h,\beta), U_0(h,\beta)$ with $U_{-} < U_0 < U_{+}$ and $F'_{h,\beta}(U_{\pm}) < 0$. It can then be shown that (modulo uniform translations) there exists a unique traveling front solution of (3.3) such that $u(x,t) = U(\xi), \xi = x - ct$, with $U(\xi) \to U_{\pm}$ as $\xi \to \mp \infty$ [26]. The speed of the wave satisfies

$$c = c(h, \beta) = \frac{\Gamma_{h, \beta}}{\int_{-\infty}^{\infty} u'^2 f'(u) d\xi},$$
(3.5)

where

$$\Gamma_{h,\beta} = \int_{U_{-}}^{U_{+}} F_{h,\beta}(u) du. \tag{3.6}$$

Since the denominator of equation (3.5) is positive definite, the sign of c is determined by the sign of the coefficient $\Gamma_{h,\beta}$; see Figure 3.1. In particular, suppose that h=0.5 and f is given by the sigmoid function (3.2) so that $f(u)-h=\tanh(u/2\gamma)/2$. It follows that, for $0<1+\beta<\gamma/4$, there exists a pair of stable homogeneous fixed points with $U_-=-U_+$, which in turn implies that $\Gamma_{h,\beta}=0$ and the front solution is stationary, see Figure 3.1. The corresponding function $F_{h,\beta}(u)$ has the inflection symmetry $F_{h,\beta}(-u)=-F_{h,\beta}(u)$. Note, the stationary solution of (3.3) is also an ϵ -independent solution of the full system (3.1) with I(x)=-h but is not necessarily the only solution (see below).

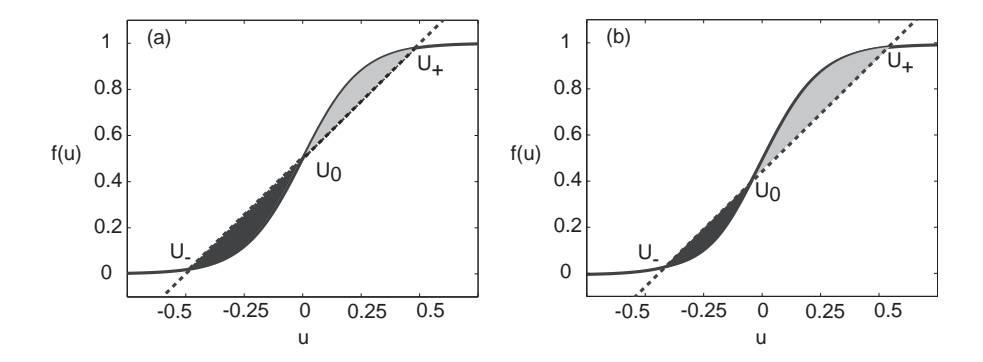


Figure 3.1. Balance condition for the speed of a traveling wave front in a scalar excitatory network with u(x,t) = U(x-ct) such that $U(\mp \infty) = U_{\pm}$. The solid curve is $f(u) = 1/(1 + e^{-\gamma u})$ with $\gamma = 8$ and the dashed line is $g(u) = (1+\beta)u + h$. The wavespeed c is positive (negative) if the grey shaded area is larger (smaller) than the black shaded area. (a) h = 0.5, $\beta = 0.5$ such that c = 0. (b) h = 0.4, $\beta = 0.5$ such that c > 0.

The regime $\epsilon \gg 1$. In the large ϵ regime, the neural field v varies on a much faster time scale than u. Introducing the stretched time coordinate $\tau = t/\delta$ with $\delta = \epsilon^{-1} \ll 1$, we have

$$\frac{\partial u}{\partial \tau}(x,\tau) = \delta \left(-u(x,\tau) + \int_{-\infty}^{\infty} w(x-x') f(u(x',\tau)) dx' - \beta v(x,\tau) - h \right)
\frac{\partial v}{\partial \tau}(x,\tau) = -v(x,\tau) + u(x,\tau).$$
(3.7)

To leading order in δ , u is independent of τ so we can explicitly solve for v

$$v(x,t) = v_0(x)e^{-\epsilon t} + u(x,t)(1 - e^{-\epsilon t}).$$
 (3.8)

Thus, after an initial transient of duration $t \sim \mathcal{O}(\epsilon^{-1})$, the field v adiabatically follows the field u, with the latter evolving according to the scalar equation (3.3). It follows that in the large ϵ regime there exists a unique traveling wave solution of the full system with (u(x,t),v(x,t))=(U(x-ct),V(x-ct)) such that $(U,V)\to (U_\pm,U_\pm)$ as $\xi\to \mp\infty$ and $c=c(h,\beta)$, $U_\pm=U_\pm(h,\beta)$. The front is stable in the large ϵ regime provided that the solution of the corresponding scalar equation is stable, which is found to be the case numerically. If $\Gamma_{h,\beta}=0$, the front is stationary, persisting for all ϵ , but may destabilize as ϵ is reduced.

The regime $0 < \epsilon \ll 1$. In the small ϵ regime, additional front solutions can be constructed that connect the two fixed points $(u,v) = (U_{\pm}(h,\beta), U_{\pm}(h,\beta))$. This follows from the observation that the neural field v remains approximately constant on the length scale over which u varies, that is, within the transition layer of the front. Suppose that the system is prepared in the down state (U_{-}, U_{-}) and is perturbed on its left-hand side to induce a transition to the upper state (U_{+}, U_{+}) . In this case $v \approx U_{-}$ within the transition layer and this generates a front propagating to the right whose speed is approximately given by equation (3.5) with $h \to h + \beta U_{-}$, that is, $c = c(h + \beta U_{-}, 0)$. If, on the other hand, the system is prepared in the up state (U_{+}, U_{+}) and is perturbed on its right-hand side to induce a transition to the down state (U_{-}, U_{-}) , then a left-propagating front is generated with $c = c(h + \beta U_{+}, 0)$. Note from (3.6)

$$\Gamma_{h+\beta U_{-},0} > \Gamma_{h,\beta} + \beta \int_{U_{-}}^{U_{+}} (u - U_{-}) du, \quad \Gamma_{h+\beta U_{+},0} < \Gamma_{h,\beta} + \beta \int_{U_{-}}^{U_{+}} (u - U_{+}) du$$

so $\Gamma_{h+\beta U_-,0} > \Gamma_{h,\beta} > \Gamma_{h+\beta U_+,0}$. Hence, the existence of fronts propagating in opposite directions clearly holds when h,β are chosen such that $\Gamma_{h,\beta} = 0$.

3.2 Front Bifurcation

The above analysis suggests that, if $\Gamma_{h,\beta}=0$, then at some critical rate of feedback $\epsilon=\epsilon_c$, a pair of counter-propagating fronts bifurcate from a stationary front. Moreover, all of the front solutions exhibit the same asymptotic behavior $(U(\xi),V(\xi))\to (U_\pm,U_\pm)$ as $\xi\to\mp\infty$. Following along analogous lines to Hagberg and Meron [43], we carry out a perturbation expansion, in powers of the speed c about this critical point, and show that the stationary solution undergoes a pitchfork bifurcation.

Setting
$$I(x) = -\hat{h}$$
 and $(u(x,t), v(x,t)) = (U(\xi), V(\xi))$ in (3.1) yields
$$-cU' = -U + w * f(U) - \beta V - h$$

$$-cV' = \epsilon(-V + U)$$
(3.9)

where $U' = dU/d\xi$, $\xi = x - ct$, and * denotes the convolution operator,

$$w * U = \int_{-\infty}^{\infty} w(\xi - \xi') U(\xi') d\xi'.$$
 (3.10)

Suppose β and h are fixed such that $\Gamma_{h,\beta} = 0$, and denote the corresponding stationary solution by $(\overline{U}, \overline{V})$. Expand the fields U, V as power series in c:

$$U(\xi) = \overline{U}(\xi) + cU_1(\xi) + c^2 U_2(\xi) + \cdots$$

$$V(\xi) = \overline{V}(\xi) + cV_1(\xi) + c^2 V_2(\xi) + \cdots$$
(3.11)

Note that the higher order terms $U_n(\xi), V_n(\xi), n \geq 1$, should all decay to zero as $\xi \to \pm \infty$, since the stationary solution already has the correct asymptotic behavior. Also expand ϵ according to

$$\epsilon = \epsilon_c + c\epsilon_1 + c^2\epsilon_2 + \cdots \tag{3.12}$$

Substitute these expansions into (3.52) and Taylor expand f(U) about \overline{U} :

$$f(U) = f(\overline{U}) + \sum_{n \ge 1} \overline{f}_n (U - \overline{U})^n, \quad \overline{f}_n = \frac{1}{n!} \frac{d^n f}{dU^n} \Big|_{U = \overline{U}}.$$
 (3.13)

Collecting all terms at successive orders of c then generates a hierarchy of equations for the perturbative corrections U_n, V_n . The lowest order equation recovers the conditions for a stationary solution:

$$(1+\beta)\overline{U} + h = w * f(\overline{U})$$

$$\overline{V} = \overline{U}.$$
(3.14)

At order c we have

$$-\overline{U}' = -U_1 + w * [\overline{f}_1 U_1] - \beta V_1 \tag{3.15}$$

$$-\overline{V}' = \epsilon_c(-V_1 + U_1) + \epsilon_c(-\overline{V} + \overline{U}). \tag{3.16}$$

The term $-\beta V_1$ in (3.15) can be eliminated using (3.16). Since $\overline{V} = \overline{U}$, we find

$$\mathcal{M}U_1 = \left(\frac{\beta}{\epsilon_c} - 1\right)\overline{U}', \quad V_1 = U_1 + \frac{\overline{U}'}{\epsilon_c}$$
 (3.17)

where \mathcal{M} is the linear operator

$$\mathcal{M}U = -(1+\beta)U + w * [\overline{f}_1 U]. \tag{3.18}$$

Since the functions $U_n(\xi)$, $V_n(\xi)$ decay to zero as $\xi \to \pm \infty$, we will assume that \mathcal{M} acts on the space $\mathcal{L}^2(\mathbb{R})$ and introduce the generalized inner product

$$\langle U|V\rangle = \int_{-\infty}^{\infty} f'(\overline{U}(\xi))U(\xi)V(\xi)d\xi \tag{3.19}$$

for all $U, V \in \mathcal{L}^2(\mathbb{R})$. With respect to this space, \mathcal{M} is self-adjoint and has the null vector $\overline{U}^{'1}$:

$$\mathcal{M}\overline{U}' = \mathcal{M}^{\dagger}\overline{U}' = 0. \tag{3.20}$$

¹We could equally well proceed by taking the standard inner product $\langle U|V\rangle = \int_{-\infty}^{\infty} U(\xi)V(\xi)d\xi$. The adjoint of \mathcal{M} is then given by $\mathcal{M}^{\dagger}U = -(1+\beta)U + \overline{f}_1w*U$, which has the null vector $\overline{f}_1\overline{U}'$ where $\overline{f}_1 = f'(\overline{U})$.

Applying the Fredholm alternative to (3.17) then gives the solvability condition

$$\langle \overline{U}' | \overline{U}' \rangle \left(\frac{\beta}{\epsilon_c} - 1 \right) = 0.$$
 (3.21)

Since $f'(\overline{U}(\xi)) > 0$ for all ξ , it follows that $\langle \overline{U}' | \overline{U}' \rangle > 0$ and thus $\epsilon_c = \beta$. This in turn means that $\mathcal{M}U_1 = 0$, and hence $U_1 = A\overline{U}'$ for some constant A. Since \overline{U}' is the generator of uniform translations, we are free to choose the origin such that A = 0. Under this choice,

$$U_1 = 0, \quad V_1 = \frac{\overline{U}'}{\epsilon_c}.$$
 (3.22)

At order c^2 we obtain

$$-U_1' = \mathcal{M}U_2 + \beta(-V_2 + U_2) + w * [\overline{f}_2 U_1^2]$$
(3.23)

$$-V_1' = \epsilon_c(-V_2 + U_2) + \epsilon_1(-V_1 + U_1) + \epsilon_2(-\overline{V} + \overline{U}). \tag{3.24}$$

Substituting for $-V_2 + U_2$ in (3.23), and using (3.22), $\overline{V} = \overline{U}$, $\beta = \epsilon_c$ yields

$$\mathcal{M}U_2 = \frac{1}{\epsilon_c} \left(\overline{U}'' - \epsilon_1 \overline{U}' \right), \quad V_2 = U_2 + \frac{1}{\epsilon_c^2} \left(\overline{U}'' - \epsilon_1 \overline{U}' \right). \tag{3.25}$$

Applying the Fredholm alternative to (3.25) yields the solvability condition

$$\langle \overline{U}' | \overline{U}'' \rangle = \epsilon_1 \langle \overline{U}' | \overline{U}' \rangle. \tag{3.26}$$

In order to evalute the inner product $\langle \overline{U}' | \overline{U}'' \rangle$, we use the result

$$(1+\beta)\frac{d^2\overline{U}}{d\xi^2} = \int_{-\infty}^{\infty} w(\xi - \xi') \frac{d^2 f(\overline{U}(\xi'))}{d\xi'^2} d\xi', \qquad (3.27)$$

which follows from differentiating equation (3.14) with respect to ξ and using the asymptotic properties of w. Then, since $w'(\xi)$ is an odd function of ξ ,

$$\langle \overline{U}' | \overline{U}'' \rangle = \int_{-\infty}^{\infty} f'(\overline{U}(\xi)) \overline{U}'(\xi) \overline{U}''(\xi) d\xi$$

$$= \int_{-\infty}^{\infty} \frac{df(\overline{U}(\xi))}{d\xi} \overline{U}''(\xi) d\xi$$

$$= \frac{1}{1+\beta} \int_{-\infty}^{\infty} \int_{-\infty}^{\infty} \frac{df(\overline{U}(\xi))}{d\xi} w(\xi - \xi') \frac{d^2 f(\overline{U}(\xi'))}{d\xi'^2} d\xi' d\xi$$

$$= \frac{1}{1+\beta} \int_{-\infty}^{\infty} \int_{-\infty}^{\infty} \frac{df(\overline{U}(\xi))}{d\xi} w'(\xi - \xi') \frac{df(\overline{U}(\xi'))}{d\xi'} d\xi' d\xi$$

$$= 0. \tag{3.28}$$

This last step follows from the fact that, if h(x) is an odd function,

$$\mathcal{K} \equiv \int_{\mathbb{R}} \int_{\mathbb{R}} h(x-y)\varphi(x)\varphi(y)dxdy = -\int_{\mathbb{R}} \int_{\mathbb{R}} h(y-x)\varphi(y)\varphi(x)dydx \equiv -\mathcal{K},$$

implying that $\mathcal{K} = 0$. Hence, $\epsilon_1 = 0$ and

$$\mathcal{M}U_2 = \frac{\overline{U}''}{\epsilon_c}, \quad V_2 = U_2 + \frac{\overline{U}''}{\epsilon_c^2}.$$
 (3.29)

At order c^3 we obtain

$$-U_2' = \mathcal{M}U_3 + \beta(-V_3 + U_3) + 2w * [\overline{f}_2 U_1 U_2] + w * [\overline{f}_3 U_1^3]$$
(3.30)

$$-V_2' = \epsilon_c(-V_3 + U_3) + \epsilon_1(-V_2 + U_2) + \epsilon_2(-V_1 + U_1) + \epsilon_3(-\overline{V} + \overline{U}). \quad (3.31)$$

Substituting for $-V_2 + U_2$ in (3.30) and using (3.22), (3.29), $\overline{V} = \overline{U}$, $\beta = \epsilon_c$, $\epsilon_1 = 0$ gives

$$\mathcal{M}U_3 = \frac{1}{\epsilon_c^2} \left(\overline{U}^{"'} - \epsilon_2 \epsilon_c \overline{U}' \right), \quad V_3 = U_3 + \frac{1}{\epsilon_c^3} (\overline{U}^{"'} + \epsilon_c^2 U_2' - \epsilon_2 \epsilon_c \overline{U}'). \quad (3.32)$$

Applying the Fredholm alternative to (3.32) yields the solvability condition

$$\epsilon_2 = \frac{\langle \overline{U}' | \overline{U}''' \rangle}{\epsilon_c \langle \overline{U}' | \overline{U}' \rangle} < 0. \tag{3.33}$$

The sign of ϵ_2 is determined using (3.27) and that $w(\xi)$ is positive and even:

$$\begin{split} \langle \overline{U}' | \overline{U}''' \rangle &= \int_{-\infty}^{\infty} f'(\overline{U}(\xi)) \overline{U}'(\xi) \overline{U}'''(\xi) d\xi \\ &= \int_{-\infty}^{\infty} \frac{df(\overline{U}(\xi))}{d\xi} \overline{U}'''(\xi) d\xi \\ &= -\int_{-\infty}^{\infty} \frac{d^2 f(\overline{U}(\xi))}{d\xi^2} \overline{U}''(\xi) d\xi \\ &= -\frac{1}{1+\beta} \int_{-\infty}^{\infty} \int_{-\infty}^{\infty} \frac{d^2 f(\overline{U}(\xi))}{d\xi^2} w(\xi - \xi') \frac{d^2 f(\overline{U}(\xi'))}{d\xi'^2} d\xi' d\xi \\ &< 0. \end{split}$$

$$(3.34)$$

Hence $\epsilon_2 < 0$.

Combining these various results, we find that

$$U(\xi) = \overline{U}(\xi) + \mathcal{O}(c^2)$$

$$V(\xi) = \overline{U}(\xi) + \frac{c}{\epsilon_c}\overline{U}'(\xi) + \mathcal{O}(c^2)$$
(3.35)

and

$$\epsilon = \epsilon_c + c^2 \epsilon_2 + \mathcal{O}(c^3). \tag{3.36}$$

Equation (3.36) implies that the stationary front undergoes a pitchfork bifurcation, which is supercritical since $\epsilon_2 < 0$. (This assumes of course that the stationary front is stable for $\epsilon > \epsilon_c$. This can be confirmed numerically, and also proven analytically in the high gain limit, see section 3.4). Close to the bifurcation point the shape of the propagating fronts is approximately the same as the stationary front, except that the recovery variable V is shifted relative to U by an amount proportional to the speed c, that is

$$U(\xi) \approx \overline{U}(\xi), \quad V(\xi) \approx \overline{U}(\xi + c/\epsilon_c).$$
 (3.37)

An analogous result was previously obtained for reaction—diffusion equations [43]. It is important to emphasize that the occurrence of a pitchfork bifurcation from a stationary front does not require any underlying inflection symmetries of the nonlinear function f (see also [3]). We only require that the scalar equation (3.3) supports a stationary front for appropriate choices of h, β . The fact that the weight distribution w(x) is even means that there must be a pitchfork bifurcation from a stationary solution rather than a transcritical bifurcation as in the case of a nonsymmetric w.

3.3 The Effect of a Weak Input Inhomogeneity

Now suppose that both ϵ and h are allowed to vary. We then expect a codimension 2 cusp bifurcation in which the pitchfork bifurcation unfolds into a saddle–node bifurcation, with the stationary front replaced by a traveling front in the large ϵ regime. More interestingly, as in the case of reaction–diffusion systems [93, 44, 3], the pitchfork bifurcation acts as an organizing center for a variety of dynamical phemomena, including the formation of breathers due to the presence of a weak input inhomogeneity. These breathers consist of periodic reversals in propagation that can be understood in terms of a dynamic transition between the pair of counter–propagating fronts that is induced by the weak intrinsic perturbation. Such a transition involves an interaction between a translational degree of freedom and an order parameter that determines the

direction of propagation. In order to unravel this interaction, it is necessary to extend the perturbation analysis of section 3.2 along analogous lines to previous treatments of reaction—diffusion systems [93, 44, 3].

Suppose that the system (3.1) undergoes a pitchfork bifurcation from a stationary state when $\epsilon = \epsilon_c = \beta$ and I(x) = -h. Introduce the small parameter δ according to $\epsilon - \epsilon_c = \delta^2 \chi$ and introduce a weak input inhomogenity by taking $I(x) = -h + \delta^3 \eta(x)$. Since any fronts are slowly propagating, we rescale time according to $\tau = \delta t$ so that equation (3.1) becomes

$$\delta \frac{\partial u(x,\tau)}{\partial \tau} = -u(x,t) + \int_{-\infty}^{\infty} w(x-x') f(u(x',\tau)) dx' - \beta v(x,\tau) - h + \delta^{3} \eta(x)$$

$$\delta \frac{\partial v(x,\tau)}{\partial \tau} = (\epsilon_{c} + \delta^{2} \chi) \left[-v(x,\tau) + u(x,\tau) \right]. \tag{3.38}$$

Motivated by equation (3.35), we introduce the ansatz that sufficiently close to the pitchfork bifurcation, the solutions of equation (3.38) can be expanded in the form

$$u(x,\tau) = \overline{U}(x-p(\tau)) + \delta^2 u_2(x,\tau) + \delta^3 u_3(x,\tau) + \cdots$$

$$v(x,\tau) = \overline{U}(x-p(\tau)) + \delta \frac{a(\delta\tau)}{\epsilon_c} \overline{U}'(x-p(\tau)) + \delta^2 v_2(x,\tau) + \delta^3 v_3(x,\tau) + \cdots$$
(3.39)

Here p is identified with the translational degree of freedom, whereas a represents the order parameter associated with changes in propagation direction. Note that a is assumed to evolve on a slower timescale than p. We now substitute the ansatz (3.39) into equation (3.38) and expand in powers of δ along similar lines to the perturbation calculation of section 3.2.

At order δ we find that

$$p_{\tau} = a, \tag{3.40}$$

where $p_{\tau} = dp/d\tau$. At order δ^2 we obtain the pair of equations

$$\mathcal{M}u_2 = a^2 \frac{\overline{U}''}{\epsilon_c}, \qquad v_2 = u_2 + a^2 \frac{\overline{U}''}{\epsilon_c^2},$$
 (3.41)

after setting $p_{\tau} = a$. The solvability condition for equation (3.41) is automatically satisfied. At order δ^3 we have

$$\frac{\partial u_2}{\partial \tau} = \mathcal{M}u_3 + \beta[-v_3 + u_3] + \eta$$

$$\frac{\partial v_2}{\partial \tau} + \frac{\overline{U}'a_{\hat{\tau}}}{\epsilon_c} = \epsilon_c[-v_3 + u_3] - a\chi \frac{\overline{U}'}{\epsilon_c}$$
(3.42)

with $\hat{\tau} = \delta \tau$. Using equation (3.41), the following equation for u_3 is obtained:

$$\mathcal{M}u_3 = \frac{1}{\epsilon_c^2} \left(a^3 \overline{U}^{"'} - a\chi \epsilon_c \overline{U}' - a_{\hat{\tau}} \epsilon_c \overline{U}' \right) - \eta. \tag{3.43}$$

Applying the Fredholm alternative to equation (3.43) yields an amplitude equation for a:

$$a_{\hat{\tau}} = -\chi a + a^3 \frac{\langle \overline{U}' | \overline{U}''' \rangle}{\epsilon_c \langle \overline{U}' | \overline{U}' \rangle} - \epsilon_c \frac{\langle \overline{U}' | \eta \rangle}{\langle \overline{U}' | \overline{U}' \rangle}. \tag{3.44}$$

Finally, rescaling p, a and η we obtain the pair of equations

$$=a$$

$$a_{t} = (\epsilon_{c} - \epsilon)a + \frac{\langle \overline{U}' | \overline{U}''' \rangle}{\epsilon_{c} \langle \overline{U}' | \overline{U}' \rangle} a^{3} - \epsilon_{c} \frac{\langle \overline{U}' | \eta \rangle}{\langle \overline{U}' | \overline{U}' \rangle}.$$
(3.45)

Note that $\overline{U} = \overline{U}(x-p)$ so that the final coefficient on the right-hand side of equation (3.45) will be p-dependent in the case of an inhomogeneous input $\eta = \eta(x)$.

Cusp bifurcation for homogeneous inputs. It is clear from equation (3.45) that, when $\eta=0$, we recover the pitchfork bifurcation of a stationary front as found in section 3.2. In particular, for $\epsilon<\epsilon_c$ there are three constant speed solutions of equation (3.45) such that $a_t=0, p_t=a=c$, corresponding to an unstable stationary front and a pair of stable counter–propagating fronts with speeds

$$c = \pm \sqrt{(\epsilon_c - \epsilon)\epsilon_c \frac{\langle \overline{U}' | \overline{U}' \rangle}{|\langle \overline{U}' | \overline{U}''' \rangle|}}.$$
 (3.46)

If η is nonzero but constant, on the other hand, the final term on the right-hand side of (3.45) reduces to the constant coefficient $\epsilon_c \eta(f(U_+) - f(U_-))/\langle \overline{U}'|\overline{U}'\rangle$, and the pitchfork bifurcation unfolds to a saddle–node bifurcation. There are two saddle–node lines in the (η,ϵ) –plane corresponding to the condition dG(a)/da=0 where $a_t=G(a)$:

$$\eta_{sn} = \pm \frac{2}{3\sqrt{3}} \frac{(\epsilon_c - \epsilon)^{3/2}}{\epsilon_c^{1/2}} \frac{\langle \overline{U}' | \overline{U}' \rangle^{3/2}}{(f(U_+) - f(U_-))|\langle \overline{U}' | \overline{U}''' \rangle|^{1/2}}$$
(3.47)

and the corresponding speed along these lines is

$$c_{sn} = \pm \sqrt{(\epsilon_c - \epsilon)\epsilon_c \frac{\langle \overline{U}' | \overline{U}' \rangle}{3|\langle \overline{U}' | \overline{U}''' \rangle|}}.$$
 (3.48)

Hopf bifurcation for a weak inhomogeneity. The introduction of a weak input inhomogeneity can lead to a Hopf instability of the stationary front. We shall illustrate this by considering the particular example of the step inhomogeneity

$$\eta(x) = \begin{cases}
s/2 & \text{if } x \le 0 \\
-s/2 & \text{if } x > 0
\end{cases}$$
(3.49)

with s > 0. For such an input we find that

$$\langle \overline{U}'|\eta\rangle = \frac{s}{2} \Big[2f(\overline{U}(-p)) - f(U_+) - f(U_-) \Big]. \tag{3.50}$$

Recall from section 3.1 that when h=0.5 the homogeneous network with f given by equation (3.2) supports a stationary front solution for which $U_{\pm}=\pm 0.5/(1+\beta)$, and $\overline{U}(0)=0$ such that $f(U_{+})+f(U_{-})=2f(0)$. Hence, equation (3.45) has a fixed point at p=0, a=0. Linearization about this fixed point shows that there is a Hopf bifurcation of the stationary front at $\epsilon=\epsilon_c$ with Hopf frequency

$$\omega_H = \sqrt{\frac{s\epsilon_c f'(0)|\overline{U}'(0)|}{\langle \overline{U}'|\overline{U}'\rangle}}.$$
(3.51)

The supercritical or subcritical nature of the Hopf bifurcation can then be determined by evaluating higher–order terms in a, p. However, this is complicated by the fact that we do not have an analytical expression for the stationary front solution \overline{U} , in contrast to the case of a reaction–diffusion equation with a cubic nonlinearity [3]. (Note that as in the case of reaction-diffusion equations [3], one can develop a more intricate perturbation analysis that takes into account $\mathcal{O}(\delta^2)$ inhomogeneities and corresponding shifts in the Hopf bifurcation point. Here we have followed a simpler approach in order to illustrate the basic ideas underlying the perturbative treatment of the integrodifferential equation (3.1)).

3.4 Exactly Solvable Model

We now consider the high gain limit $\gamma \to \infty$, for which equation (3.2) reduces to $f(u) = H(u - \kappa)$ where H is the Heaviside function H(u) = 1 if u > 0 and H(u) = 0 if $u \le 0$. The advantage of using a threshold nonlinearity is that explicit analytical expressions for front solutions can be obtained, which allows us to derive conditions for the Hopf instability of a stationary front without any restrictions on the size of the input inhomogeneity. Numerical simulations of the full system establish that the bifurcation is supercritical and that it generates an oscillatory modulation of the stationary front in the form of a breather.

3.4.1 Traveling Fronts (Homogeneous Case)

We begin by deriving exact traveling front solutions of equation (3.1) for $f(u) = H(u - \kappa)$ and a homogeneous input I(x) = 0. That is, we seek a solution of the form $u(x,t) = U(\xi)$, $\xi = x - ct$, c > 0, such that

$$U(x) > \kappa,$$
 $x \in (-\infty, 0);$ $U(0) = \kappa,$ $U(x) < \kappa,$ $x \in (0, +\infty);$ $U(\mp \infty) = U_{\pm}.$

Setting $v(x,t) = V(\xi)$, we then have

$$-cU'(\xi) + U(\xi) = \int_{-\infty}^{0} w(\xi - \xi')d\xi' - \beta V(\xi)$$
 (3.52)

$$-\frac{c}{\epsilon}V'(\xi) = -V(\xi) + U(\xi). \tag{3.53}$$

Differentiating the first equation and substituting into the second, we obtain a second order ODE with boundary conditions at $\xi = 0$ and $\pm \infty$:

$$-c^{2}U''(\xi) + c[1+\epsilon]U'(\xi) - \epsilon[1+\beta]U(\xi) = -cw(\xi) - \epsilon W(\xi)$$

$$U(0) = \kappa$$

$$U(\mp \infty) = U_{\pm}$$
(3.54)

where

$$W(\xi) = \int_{\xi}^{\infty} w(y)dy. \tag{3.55}$$

Here U_{\pm} are the homogeneous fixed point solutions

$$U_{+} = \frac{1}{1+\beta}, \quad U_{-} = 0.$$
 (3.56)

We have used the fact that w has unit normalization, $W(-\infty) \equiv \int_{\mathbb{R}} w(y) dy = 1$. It follows that a necessary condition for the existence of a front solution is $\kappa < U_+$.

In order to establish the existence of a traveling front, we solve the boundary value problem on the domains $\xi \leq 0$ and $\xi \geq 0$ and match the solutions at $\xi = 0$. For further mathematical convenience, we take the weight distribution to be an exponential function

$$w(x) = \frac{1}{2d} e^{-|x|/d}$$
 (3.57)

where d determines the range of the synaptic interactions. We fix the spatial scale by setting d = 1; a typical value of d is 1 mm. We first consider the case

of right-moving waves (c > 0). On the domain $\xi \ge 0$, the particular solution is $U_>(\xi) = \kappa e^{-\xi}$ with κ related to the speed c according to the self-consistency condition

$$\kappa = \frac{c + \epsilon}{2(c^2 + c[1 + \epsilon] + \epsilon[1 + \beta])}, \qquad c \ge 0.$$
(3.58)

In the domain $\xi \leq 0$ the solution consists of complementary and particular parts:

$$U_{<}(\xi) = \mathcal{A}_{+}e^{\mu_{+}\xi} + \mathcal{A}_{-}e^{\mu_{-}\xi} + \mathcal{A}e^{\xi} + U_{+}, \tag{3.59}$$

where

$$\mu_{\pm} = \frac{1}{2c} \left[1 + \epsilon \pm \sqrt{(1+\epsilon)^2 - 4\epsilon(1+\beta)} \right]. \tag{3.60}$$

The coefficient \mathcal{A} is obtained by direct substitution into the differential equation for U, whereas the coefficients \mathcal{A}_{\pm} are determined by matching solutions at the boundary $\xi = 0$, that is, $U_{<}(0) = \kappa$ and $U'_{<}(0) = -\kappa$. Thus we find

$$\mathcal{A} = \frac{c - \epsilon}{2(c^2 - c[1 + \epsilon] + \epsilon[1 + \beta])},\tag{3.61}$$

$$A_{+} = \frac{\mu_{-}U_{+} + (\mu_{-} - 1)A - (1 + \mu_{-})\kappa}{\mu_{+} - \mu_{-}},$$
(3.62)

$$\mathcal{A}_{-} = \frac{-\mu_{+}U_{+} + (1 - \mu_{+})\mathcal{A} + (1 + \mu_{+})\kappa}{\mu_{+} - \mu_{-}}.$$
 (3.63)

In the limit $\beta \to 0$ we recover the standard result for an excitatory network without feedback [26]:

$$U(\xi) = \begin{cases} \frac{1}{2(c+1)} e^{-\xi} & \text{for } \xi > 0\\ 1 + (\kappa - 1)e^{\xi/c} + \frac{1}{2(c-1)} \left[e^{\xi} - e^{\xi/c} \right] & \text{for } \xi < 0 \end{cases}$$
(3.64)

with

$$\kappa = \frac{1}{2(c+1)}, \qquad c \ge 0.$$
(3.65)

A similar analysis can be carried out for left-moving waves. Now the speed c is determined by the particular solution in the domain $\xi \leq 0$, which takes the form $U_{\leq}(\xi) = -\hat{\kappa}e^{\xi} + U_{+}$ with $\hat{\kappa} = (1 + \beta)^{-1} - \kappa$. This leads to the self-consistency condition

$$\hat{\kappa} = -\frac{c - \epsilon}{2(c^2 - c[1 + \epsilon] + \epsilon[1 + \beta])}, \qquad c \le 0.$$
(3.66)

The existence of traveling front solutions can now be established by finding positive real solutions of equation (3.58) and negative real solutions of equation

(3.66). For concreteness, we will assume that the threshold κ is fixed and determine the solution branches as a function of the feedback parameters ϵ , β with $1/\kappa - 1 > \beta > 0$. The roots of equation (3.58) and (3.66) can be written explicitly as

$$c = \frac{1}{2} \left[-\left(1 + \epsilon - \frac{1}{2\kappa}\right) \pm \sqrt{\left(1 + \epsilon - \frac{1}{2\kappa}\right)^2 - 4\epsilon \left(1 + \beta - \frac{1}{2\kappa}\right)} \right]$$
 (3.67)

and

$$c = \frac{1}{2} \left[+ \left(1 + \epsilon - \frac{1}{2\hat{\kappa}} \right) \pm \sqrt{\left(1 + \epsilon - \frac{1}{2\hat{\kappa}} \right)^2 - 4\epsilon \left(1 + \beta - \frac{1}{2\hat{\kappa}} \right)} \right]. \quad (3.68)$$

Using the fact that $\operatorname{sgn}\left(1+\beta-\frac{1}{2\kappa}\right)=-\operatorname{sgn}\left(1+\beta-\frac{1}{2k}\right)$, we find that there are three bifurcation scenarios as shown in Figure 3.2:

- (i) If $2\kappa(1+\beta) = 1$ then there exists a stationary front for all ϵ . At a critical value of ϵ the stationary front undergoes a pitchfork bifurcation leading to the formation of a left and a right-moving wave. This is the high-gain limit of the front bifurcation analyzed in section 3.2 for smooth f.
- (ii) If $2\kappa(1+\beta) > 1$ then there is a single left-moving wave for all ϵ . There also exists a pair of right-moving waves that annihilate in a saddle-node bifurcation at a critical value of ϵ that approaches zero as $\beta \to 0$.
- (iii) If $2\kappa(1+\beta) < 1$ then there is a single right-moving wave for all ϵ . There also exists a pair of left-moving waves that annihilate in a saddle-node bifurcation at a critical value of ϵ that approaches zero as $\beta \to 0$.

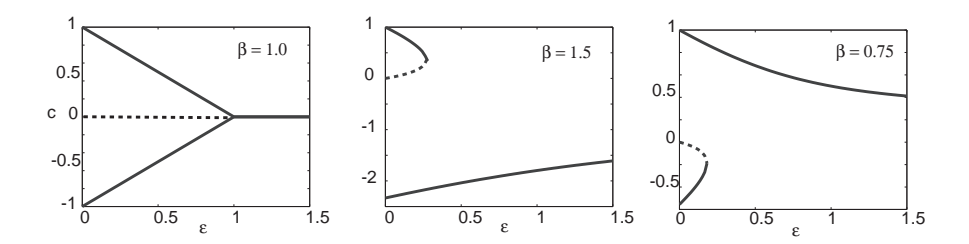


Figure 3.2. Plot of wavefront speed c as a function of ϵ for various values of β and a fixed threshold $\kappa = 0.25$: (i) $2\kappa(1+\beta) = 1$, (ii) $2\kappa(1+\beta) > 1$, (iii) $2\kappa(1+\beta) < 1$. Stable (unstable) branches are shown as solid (dashed) curves.

3.4.2 Stability Analysis of Stationary Fronts

Stationary front solutions of (3.1) with $f(u) = H(u - \kappa)$ in the case of an inhomogeneous input I(x) satisfy the equation

$$(1+\beta)U(x) = \int_{-\infty}^{x_0} w(x-x')dx' + I(x).$$
 (3.69)

Suppose that I(x) is a monotonically decreasing function of x. Since the system is no longer translation invariant, the position of the front is pinned to a particular location x_0 where $U(x_0) = \kappa$. Monotonicity of I(x) ensures that $U(x) > \kappa$ for $x < x_0$ and $U(x) < \kappa$ for $x > x_0$. The center x_0 satisfies

$$(1+\beta)\kappa = \frac{1}{2} + I(x_0) \tag{3.70}$$

under the normalization $\int_0^\infty w(y)dy = 1/2$. Equation (3.70) implies that in contrast to the homogeneous case, there exists a stationary front over a range of threshold values (for fixed β); changing the threshold κ simply shifts the position of the center x_0 . In the particular case of the exponential weight distribution (3.57), we have

$$(1+\beta)U(x) = \begin{cases} \frac{e^{x_0 - x}}{2} + I(x), & x > x_0 \\ 1 - \frac{e^{x - x_0}}{2} + I(x), & x < x_0. \end{cases}$$
(3.71)

If the stationary front is stable then it will prevent wave propagation. Stability is determined by writing u(x,t) = U(x) + p(x,t) and v(x,t) = V(x) + q(x,t), with V(x) = U(x), and expanding equation (3.1) to first-order in (p, q):

$$\frac{\partial p(x,t)}{\partial t} = -p(x,t) + \int_{-\infty}^{\infty} w(x-x')H'(U(x'))p(x',t)dx' - \beta q(x,t)
\frac{1}{\epsilon} \frac{\partial q(x,t)}{\partial t} = -q(x,t) + p(x,t).$$
(3.72)

We assume that $p, q \in \mathcal{L}^2(\mathbb{R})$. The spectrum of the associated linear operator is found by taking $p(x,t) = e^{\lambda t} p(x)$ and $q(x,t) = e^{\lambda t} q(x)$. Using the identity

$$\frac{dH(U(x))}{dU} = \frac{\delta(x - x_0)}{|U'(x_0)|}$$
(3.73)

we obtain the equation

$$\left(\lambda + 1 + \frac{\epsilon \beta}{\lambda + \epsilon}\right) p(x) = \frac{w(x - x_0)}{|U'(x_0)|} p(x_0). \tag{3.74}$$

Equation (3.74) has two classes of solution. The first consists of any function p(x) such that $p(x_0) = 0$, for which $\lambda = \lambda_{\pm}^{\circ}$ where

$$\lambda_{\pm}^{\circ} = \frac{-(1+\epsilon) \pm \sqrt{(1+\epsilon)^2 - 4\epsilon(1+\beta)}}{2}.$$
 (3.75)

Note that λ_{\pm}° belong to the essential spectrum since they have infinite multiplicity. The second class of solution is of the form $p(x) = Aw(x - x_0)$, $A \neq 0$, for which λ is given by the roots of the equation

$$\lambda + 1 + \frac{\epsilon \beta}{\lambda + \epsilon} = \frac{1}{2|U'(x_0)|}. (3.76)$$

Since

$$U'(x_0) = \frac{1}{1+\beta} \left[I'(x_0) - \frac{1}{2} \right], \tag{3.77}$$

it follows that $\lambda = \lambda_{\pm}$, where

$$\lambda_{\pm} = \frac{-\Lambda \pm \sqrt{\Lambda^2 - 4(1 - \Gamma)\epsilon(1 + \beta)}}{2} \tag{3.78}$$

with

$$\Lambda = 1 + \epsilon - (1 + \beta)\Gamma \tag{3.79}$$

and

$$\Gamma = \frac{1}{1+2D}, \quad D = |I'(x_0)|.$$
 (3.80)

We have used the fact that $I'(x_0) \leq 0$. The eigenvalues λ_{\pm} determine the discrete spectrum.

3.4.3 Hopf Bifurcation to a Breathing Front

Equation (3.78) implies that the stationary front is locally stable provided that $\Lambda > 0$ or, equivalently, the gradient of the inhomogeneous input at x_0 satisfies

$$D > D_c \equiv \frac{1}{2} \frac{\beta - \epsilon}{1 + \epsilon}.\tag{3.81}$$

Since $D \geq 0$, it follows that the front is stable when $\beta < \epsilon$, that is, when the feedback is sufficiently weak or fast. On the other hand, if $\beta > \epsilon$ then there is a Hopf bifurcation at the critical gradient $D = D_c$. The corresponding critical Hopf frequency is

$$\omega_H = \sqrt{\frac{2D_c \epsilon (1+\beta)}{2D_c + 1}} = \sqrt{\epsilon (\beta - \epsilon)}.$$
 (3.82)

Note that the frequency only depends on the size and rate of the negative feedback, but is independent of the details of the synaptic weight distribution

and the size of the input. This should be contrasted with the corresponding Hopf frequency in the case of a smooth nonlinearity f and a weak step-inhomogeneity; see equation (3.51). The latter depends on the input amplitude and the form of the stationary solution \overline{U} , which itself depends on the weight distribution w.

In order to investigate the nature of solutions around the Hopf bifurcation point, we consider the particular example of a smooth ramp inhomogeneity

$$I(x) = -\frac{s}{2}\tanh(\gamma x),\tag{3.83}$$

where s is the size of the step and γ determines its steepness. A stationary front will exist provided that

$$s > \bar{s} \equiv |1 - 2\kappa(1 + \beta)|. \tag{3.84}$$

The gradient $D = s\gamma \operatorname{sech}^2(\gamma x_0)/2$ depends on x_0 , which is itself dependent on β and κ through equation (3.70). Using the identity $\operatorname{sech}^2 x = 1 - \tanh^2 x$, it follows that

$$D = \frac{\gamma}{2s} \left(s^2 - \bar{s}^2 \right). \tag{3.85}$$

Substituting into the expression for the critical slope D_c , equation (3.81), yields an expression for the critical value of s that determines the Hopf bifurcation points:

$$s_c = \frac{1}{2\gamma} \left[\frac{\beta - \epsilon}{1 + \epsilon} + \sqrt{\left(\frac{\beta - \epsilon}{1 + \epsilon}\right)^2 + 4\bar{s}^2 \gamma^2} \right]. \tag{3.86}$$

The critical height s_c is plotted as a function of β for various values of ϵ and fixed κ, γ in Figure 3.3. Note that in the homogeneous case (s=0) a stationary solution only exists at the particular value of β given by $\beta=1/(2\kappa)-1$. This solution is stable for $\epsilon>\beta$ and unstable for $\epsilon<\beta$, consistent with the pitchhfork bifurcation shown in Figure 3.2. Close to the front bifurcation $\epsilon=\beta$, the Hopf bifurcation occurs in the presence of a weak input inhomogeneity, which is the case considered in section 3.1. Now, however, it is possible to determine the bifurcation curve without any restrictions on the size of the input.

Numerically solving the full system of equations (3.1) for a step input I(x), exponential weights w(x) and threshold nonlinearity $f(u) = H(u - \kappa)$ shows that the Hopf bifurcation is supercritical, in which there is a transition to a small amplitude breather whose frequency of oscillation is approximately equal to the Hopf frequency ω_H . As the input amplitude s is reduced beyond the Hopf bifurcation point, the amplitude of the oscillation increases until the breather itself becomes unstable and there is a secondary bifurcation to a traveling front.

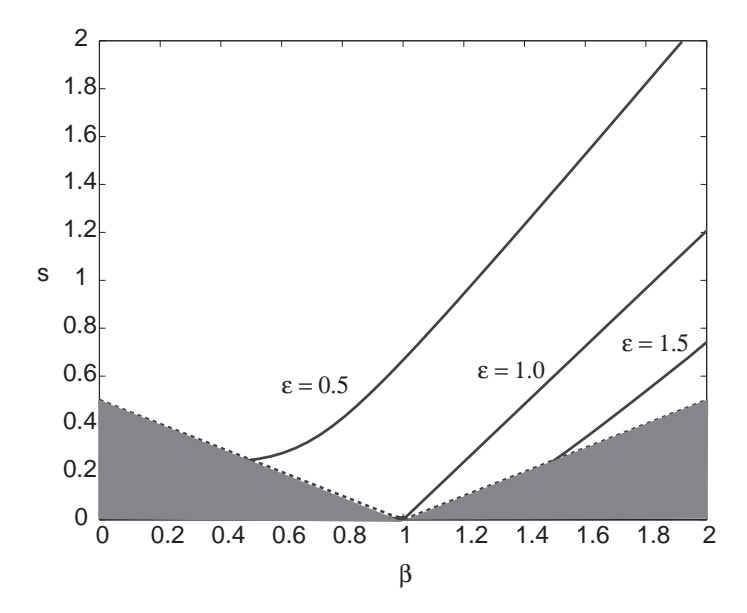


Figure 3.3. Stability phase diagram for a stationary front in the case of a step input $I(x) = -s \tanh(\gamma x)/2$ where γ is the steepness of the step and s its height. Hopf bifurcation lines (solid curves) in (β, s) -parameter space are shown for various values of ϵ . In each case the stationary front is stable above the line and unstable below it. The shaded area denotes the region of parameter space where a stationary front solution does not exist. The threshold $\kappa = 0.25$ and $\gamma = 0.5$.

This is illustrated in Fig. 3.4, which shows a space-time plot of the developing breather as the input amplitude is slowly reduced. As we shall see in Chapter 4, analogous results occur for pulses in the presence of stationary Gaussian inputs, where a reduction in the input amplitude induces a Hopf bifurcation to a pulse–like breather. Interestingly, the localized breather can itself undergo a secondary instability leading to the periodic emission of traveling waves.

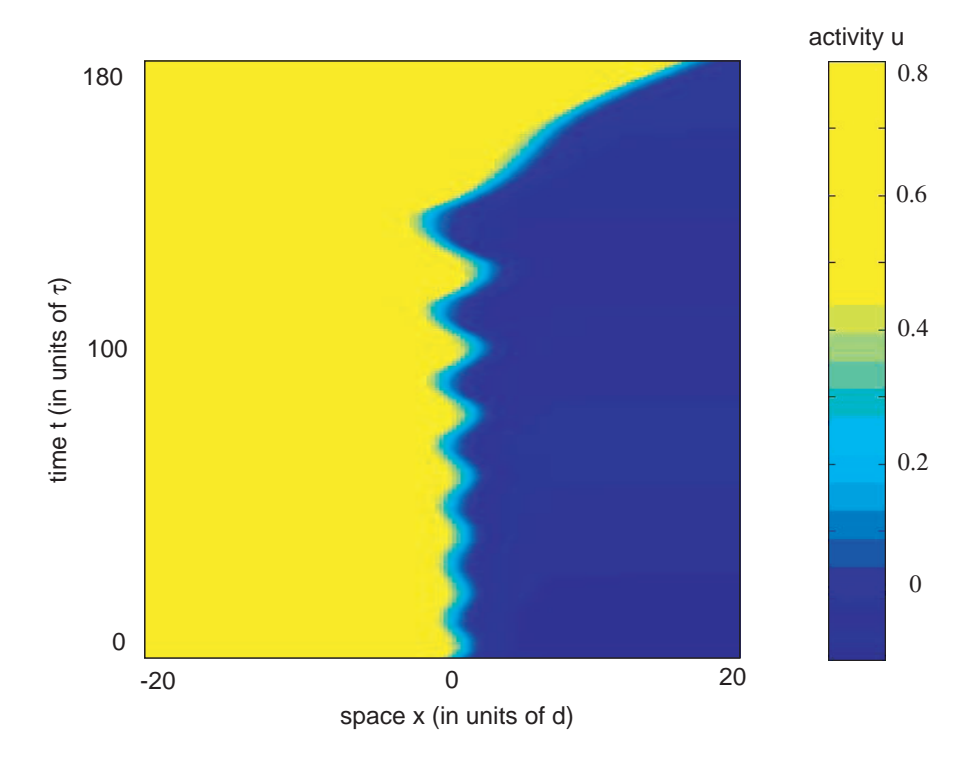


Figure 3.4. Breather-like solution arising from a Hopf instability of a stationary front due to a slow reduction in the size s of the step input inhomogeneity (3.83). Here $\epsilon = 0.5, \gamma = 0.5, \beta = 1, \kappa = 0.25$. The input amplitude s = 2 at t = 0 and s = 0 at t = 180. The amplitude of the oscillation steadily grows until it destabilizes at $s \approx 0.05$, leading to the generation of a traveling front.

3.4.4 Locking to a Moving Input

We conclude our analysis of the exactly solvable model by considering the effects of a moving input stimulus. This is interesting from a number of viewpoints. First, introducing a persistent stationary input into an *in vitro* cortical slice can damage the tissue, whereas a moving input (at least if it is localized) will not. Second, *in vivo* inputs into the intact cortex are typically nonstationary, as exemplified by inputs to the visual cortex induced by moving visual stimuli. We consider the particular problem of whether or not a traveling front can lock to a step-like input $I(x) = I_0\chi(x - vt)$ traveling with constant speed v, where

$$\chi(x) = \begin{cases} -1, & x > 0 \\ 0, & x = 0 \\ +1, & x < 0. \end{cases}$$

Such a front moves at the same speed as the input but may be shifted in space relative to the input.

We proceed by introducing the traveling wave coordinate $\xi = x - vt$ and deriving existence conditions for a front solution $U(\xi)$ satisfying $U(\xi_0) = \kappa$, $U(\xi) \to 0$ as $\xi \to \infty$, and $U(\xi) \to (1+\beta)^{-1}$ as $\xi \to -\infty$. Substituting into equation (3.1) gives

$$-vU'(\xi) = -U(\xi) + \int_{-\infty}^{\xi_0} w(\xi - \eta) d\eta - \beta V(\xi) + I_0 \chi(\xi)$$
$$-vV'(\xi) = \epsilon(-V(\xi) + U(\xi)). \tag{3.87}$$

Setting $W(\xi) = \int_{\xi}^{\infty} w(\eta) d\eta$, we rewrite this set of equations in the matrix form

$$\mathbf{LS} \equiv \begin{pmatrix} vU' - U - \beta V \\ vV' + \epsilon U - \epsilon V \end{pmatrix} = - \begin{pmatrix} N_{\mathrm{E}} \\ 0 \end{pmatrix}, \tag{3.88}$$

where

$$\mathbf{S} = (U, V)^T, \qquad N_{\text{E}}(\xi) = W(\xi - \xi_0) + I_0 \chi(\xi).$$
 (3.89)

We use variation of parameters to solve this linear equation. The homogeneous problem $\mathbf{L}S = 0$ has the two linearly independent solutions,

$$\mathbf{S}_{+}(\xi) = \begin{pmatrix} \beta \\ m_{+} - 1 \end{pmatrix} \exp(\mu_{+}\xi) \tag{3.90}$$

$$\mathbf{S}_{-}(\xi) = \begin{pmatrix} \beta \\ m_{-} - 1 \end{pmatrix} \exp(\mu_{-}\xi) \tag{3.91}$$

where

$$\mu_{\pm} = \frac{m_{\pm}}{v},$$
 $m_{\pm} = \frac{1}{2} \left(1 + \epsilon \pm \sqrt{(1 - \epsilon)^2 - 4\epsilon\beta} \right)$

By variation of parameters we define

$$\mathbf{S}(\xi) = \begin{bmatrix} \mathbf{S}_{+} | \mathbf{S}_{-} \end{bmatrix} \begin{pmatrix} a(\xi) \\ b(\xi) \end{pmatrix},$$

where [A|B] denotes the matrix whose first column is defined by the vector **A** and whose second column is defined by the vector **B**. Then

$$\mathbf{LS} = v \frac{\partial}{\partial \xi} \left(\begin{bmatrix} \mathbf{S}_{+} | \mathbf{S}_{-} \end{bmatrix} \begin{pmatrix} a(\xi) \\ b(\xi) \end{pmatrix} \right) - \begin{pmatrix} 1 & \beta \\ -\epsilon & \epsilon \end{pmatrix} \left(\begin{bmatrix} \mathbf{S}_{+} | \mathbf{S}_{-} \end{bmatrix} \begin{pmatrix} a(\xi) \\ b(\xi) \end{pmatrix} \right)$$

$$= v \begin{bmatrix} \mathbf{S}_{+} | \mathbf{S}_{-} \end{bmatrix} \frac{\partial}{\partial \xi} \begin{pmatrix} a(\xi) \\ b(\xi) \end{pmatrix}, \tag{3.92}$$

since $\mathbf{LS}_{\pm} = 0$. Thus equation (3.88) reduces to

$$\left[\mathbf{S}_{+}\middle|\mathbf{S}_{-}\right]\frac{\partial}{\partial\xi}\begin{pmatrix}a(\xi)\\b(\xi)\end{pmatrix} = -\frac{1}{v}\begin{pmatrix}N_{\mathrm{E}}\\0\end{pmatrix}. \tag{3.93}$$

The matrix $\left[\mathbf{S}_{+}\middle|\mathbf{S}_{-}\right]$ is invertible. Introducing the vector–valued functions

$$\mathbf{Z}_{+}(\xi) = \begin{pmatrix} 1 - m_{-} \\ \beta \end{pmatrix} \exp(-\mu_{+}\xi) \tag{3.94}$$

$$\mathbf{Z}_{-}(\xi) = -\begin{pmatrix} 1 - m_{+} \\ \beta \end{pmatrix} \exp(-\mu_{-}\xi)$$
 (3.95)

we have

$$\begin{bmatrix} \mathbf{S}_{+} | \mathbf{S}_{-} \end{bmatrix} \begin{bmatrix} \mathbf{Z}_{+} | \mathbf{Z}_{-} \end{bmatrix}^{\mathrm{T}} = \begin{bmatrix} \mathbf{Z}_{+} | \mathbf{Z}_{-} \end{bmatrix}^{\mathrm{T}} \begin{bmatrix} \mathbf{S}_{+} | \mathbf{S}_{-} \end{bmatrix} = \beta (m_{+} - m_{-}) \mathbf{I},$$

where I denotes the identity matrix. Multiplying equation (3.93) by $\begin{bmatrix} \mathbf{Z}_{+} | \mathbf{Z}_{-} \end{bmatrix}^{\mathrm{T}}$ finally yields the first-order equation

$$\frac{\partial}{\partial \xi} \begin{pmatrix} a(\xi) \\ b(\xi) \end{pmatrix} = -\frac{1}{v\beta(m_{+} - m_{-})} \left[\mathbf{Z}_{+} \middle| \mathbf{Z}_{-} \right]^{\mathrm{T}} \begin{pmatrix} N_{\mathrm{E}}(\xi) \\ 0 \end{pmatrix}. \tag{3.96}$$

In order to solve equation (3.96) we need to specify the sign of v. First, suppose that v > 0, which corresponds to a right-moving front. Integrating over the interval $[\xi, \infty)$ gives

$$\begin{pmatrix} a(\xi) \\ b(\xi) \end{pmatrix} = \begin{pmatrix} a_{\infty} \\ b_{\infty} \end{pmatrix} + \frac{1}{v\beta(m_{+} - m_{-})} \int_{\xi}^{\infty} \left[\mathbf{Z}_{+} \middle| \mathbf{Z}_{-} \right]^{\mathrm{T}} \begin{pmatrix} N_{\mathrm{E}}(\eta) \\ 0 \end{pmatrix} d\eta$$

where a_{∞}, b_{∞} denote the values of a, b at ∞ . Since we seek a bounded solution $\mathbf{S}(\xi)$, we must require that $a_{\infty} = b_{\infty} = 0$. Hence the solution is

$$\begin{pmatrix} a(\xi) \\ b(\xi) \end{pmatrix} = \frac{1}{v\beta(m_{+} - m_{-})} \int_{\xi}^{\infty} \left[\mathbf{Z}_{+} \middle| \mathbf{Z}_{-} \middle|^{\mathrm{T}} \begin{pmatrix} N_{\mathrm{E}}(\eta) \\ 0 \end{pmatrix} d\eta,$$

so that

$$\mathbf{S}(\xi) = \frac{1}{v\beta(m_{+} - m_{-})} \left[\mathbf{S}_{+} | \mathbf{S}_{-} \right] \int_{\xi}^{\infty} \left[\mathbf{Z}_{+} | \mathbf{Z}_{-} \right]^{\mathrm{T}} \begin{pmatrix} N_{\mathrm{E}}(\eta) \\ 0 \end{pmatrix} d\eta.$$
 (3.97)

Further simplification occurs by introducing the functions

$$\mathcal{M}_{\pm}(\xi) = \frac{1}{v} \left(\frac{1}{m_{+} - m_{-}} \right) \int_{\xi}^{\infty} e^{\mu_{\pm}(\xi - \eta)} N_{E}(\eta) d\eta.$$

We can then express the solution $(U(\xi), V(\xi))$ as follows:

$$U(\xi) = (1 - m_{-})\mathcal{M}_{+}(\xi) - (1 - m_{+})\mathcal{M}_{-}(\xi),$$

$$V(\xi) = \beta^{-1}(m_{+} - 1)(1 - m_{-})\left[\mathcal{M}_{+}(\xi) - \mathcal{M}_{-}(\xi)\right].$$
(3.98)

To ensure that such a front exists we require that $U(\xi_0) = \kappa$, i.e.,

$$\kappa = (1 - m_{-})\mathcal{M}_{+}(\xi_{0}) - (1 - m_{+})\mathcal{M}_{-}(\xi_{0}). \tag{3.99}$$

Taking $w(x) = e^{-|x|}/2$ so that

$$W(\xi) = \begin{cases} 1 - \frac{1}{2} e^{\xi}, & \xi < 0 \\ \frac{1}{2} e^{-\xi}, & \xi \ge 0 \end{cases}$$

we can calculate $\mathcal{M}_{\pm}(\xi_0)$ explicitly as

$$\mathcal{M}_{\pm}(\xi_0) = \frac{1}{(m_+ - m_-)} \left(\frac{1}{2(v + m_{\pm})} - \frac{1}{m_{\pm}} F(\xi_0) \right)$$

where

$$F(\xi_0) = \begin{cases} I_0(2e^{\mu_{\pm}\xi_0} - 1), & \xi_0 < 0 \\ I_0, & \xi_0 \ge 0. \end{cases}$$

The case of a left–moving front, for which v < 0, follows along similar lines by integrating equation (3.96) over $(-\infty, \xi_0]$:

$$U(\xi) = (m_{-} - 1)\widetilde{\mathcal{M}}_{+}(\xi) - (m_{+} - 1)\widetilde{\mathcal{M}}_{-}(\xi)$$
(3.100)

$$V(\xi) = \beta^{-1}(m_{+} - 1)(1 - m_{-}) \left[\widetilde{\mathcal{M}}_{+}(\xi) - \widetilde{\mathcal{M}}_{-}(\xi) \right], \qquad (3.101)$$

where

$$\widetilde{\mathcal{M}}_{\pm}(\xi_0) = \frac{1}{(m_+ - m_-)} \left(\frac{1}{2} \frac{m_{\pm} - 2v}{m_+(v - m_+)} - \frac{1}{m_+} G(\xi_0) \right)$$

and

$$G(\xi_0) = \begin{cases} -I_0, & \xi_0 < 0 \\ I_0(1 - 2e^{\mu \pm \xi_0}), & \xi_0 \ge 0 \end{cases}$$

This leads to the following threshold condition for v < 0:

$$\kappa = (m_{-} - 1)\widetilde{\mathcal{M}}_{+}(\xi_{0}) - (m_{+} - 1)\widetilde{\mathcal{M}}_{-}(\xi_{0}). \tag{3.102}$$

We can now numerically solve equations (3.99) and (3.102) to determine the range of input velocities v and input amplitudes I_0 for which locking occurs. For the sake of illustration, we assume the threshold condition $2\kappa(1+\beta)=1$ and take $\epsilon<\beta$. This ensures that, in the absence of any input, there exists an unstable stationary front and a pair of stable counter–propagating waves (see Figure 3.2). The continuation of these stationary and traveling fronts as I_0 increases from zero is shown in Figure 3.5. Since $2\kappa(1+\beta)=1$, equations (3.99) and (3.102) are equivalent under the interchange $v\longmapsto -v$ and $\xi_0\longmapsto -\xi_0$. This implies that the locking regions are symmetric with respect to v. For nonzero v the traveling front is shifted relative to the input such that $\xi_0<0$ when v>0 and $\xi_0>0$ when v<0. In other words, the wave is dragged by the input. Figure 3.5 determines where locking can occur but not whether the resulting traveling wave is stable or unstable.

3.5 Discussion

This chapter serves a four-fold purpose. First, it has demonstrated that the Pinto-Ermentrout model supports forward and backward traveling front solutions, generated by a front bifurcation similar to that for reaction-diffusion equations. Strangely, Pinto and Ermentrout [80] did not consider traveling fronts in their analysis, possibly due to their placement of the parameter β . Furthermore, as in the case of reaction-diffusion, a weak input inhomogeneity can induce a Hopf instability, giving rise to an oscillatory wave front. Second, the analysis of section 3.2 and 3.3 is applicable for general excitatory (positive) weight functions and, more importantly, a smooth firing rate. Although the smooth firing rate function is more biologically realistic, it presents great challenges for mathematical analysis, especially in the case of pulses. Third, it sets up the general approach, as well as the fundamental ideas, of Chapters 4, 5, and 6, by using a Heaviside firing rate function to compute exact solutions and study the effects of input inhomogeneities without the restriction to weak

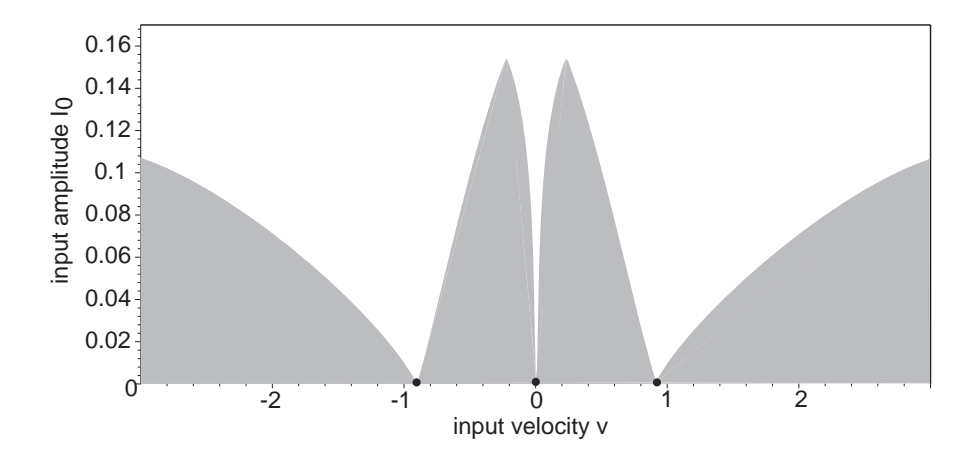


Figure 3.5. Locking of a traveling front to a moving step input with velocity v and amplitude I_0 . Other parameter values are $\beta = 1, \epsilon = 0.1, \kappa = 0.25$. Unshaded regions show where locking can occur in the (v, I_0) -plane. When $I_0 = 0$ there are three front solutions corresponding to a stationary front (v = 0) and two counter-propagating fronts, which is consistent with the front bifurcation shown in Figure 3.2. Each of these solutions forms the vertex of a distinct locking region whose width increases monotonically with I_0 so that ultimately the locking regions merge.

inputs. In this approach exact solutions are necessary to study the stability and bifurcation of stationary and traveling wave solutions, and, although we carry out some calculations only for particular weight functions, we expect the results to be more generally applicable. Fourth, comparison of the front bifurcation for smooth firing rates and Heaviside firing rate, as well as the effect of a weak input inhomogeneity, demonstrates that the Heaviside firing rate exhibits qualitatively similar results to the smooth firing rate, lending support for its use.

The stability analysis of traveling fronts is considerably more involved than that of stationary fronts but follows analogously to that shown for stimulus-locked traveling pulses analyzed in Chapter 6. Such pulses exist for sufficiently large β and lock to Gaussian-like inputs. Nevertheless, in the case of stimulus-locked fronts, we expect that for sufficiently small I_0 the locking regions around the counter–propagating fronts are stable, whereas the central region containing the stationary front is unstable. On the other hand, since $\epsilon < \beta$, we know

that the stationary front is stable for large inputs I_0 and undergoes a Hopf bifurcation as I_0 is reduced. This suggests that the Hopf bifurcation point at v=0 lies on a Hopf curve within the locking region so that a traveling front locked to a moving input can also be destabilized, as the strength of the input is reduced (or as the input velocity changes relative to the intrinsic velocity of waves in the homogeneous network).

CHAPTER 4

BREATHERS IN ONE-DIMENSIONAL NEURAL NETWORKS

In this chapter we extend our work on stationary fronts by analyzing the effects of input inhomogeneities on the stability of stationary pulses, since these better reflect the types of neural activity patterns observed in cortex. In order to construct exact solutions, we follow previous treatments [1, 80] and consider the high gain limit $\gamma \to \infty$ of the sigmoid function f such that $f(u) = H(u - \kappa)$ where H is the Heaviside step function. To define an excitatory network we take the weight function w to be positive and monotonically decreasing on \mathbb{R}^+ , such that $\int_{\mathbb{R}} w(x) dx < \infty$. This yields the model Pinto and Ermentrout considered to describe a disinhibited cortical slice, i.e., effectively a one-dimensional medium of excitatory neurons subject to spike-rate adaptation:

$$\frac{\partial u(x,t)}{\partial t} = -u(x,t) + \int_{-\infty}^{\infty} w(x-x')H(u(x',t)-\kappa)dx' - \beta\varrho(x,t) + I(x)$$

$$\frac{1}{\epsilon} \frac{\partial\varrho(x,t)}{\partial t} = -\varrho(x,t) + u(x,t). \tag{4.1}$$

In section 4.1 we analyze the existence and stability of stationary pulses in the presence of a unimodal input. In particular, we show that (i) a sufficiently large input inhomogeneity can stabilize a stationary pulse and (ii) a subsequent reduction in the level of inhomogeneity can induce a Hopf instability of the stationary pulse leading to the formation of a breather-like oscillatory wave. Numerically we find that a secondary instability can occur beyond which the breather periodically emits pairs of traveling pulses (section 4.2.1). Thus, while the input causes a local pinning of activity, the surrounding medium supports wave propagation, since the effect of the input there is weak. Interestingly, depending on the spatial extent σ of the input , the periodic orbit can undergo a sequence of period doubling bifurcations prior to the sharp transition to pulse-emitting: the transition to the pulse-emitter may, in fact, be due to a subcritical period-doubling bifurcation. Moreover, there is mode-locking

between the oscillation frequency of the breather and the rate of wave emission. Analogous forms of oscillatory waves are also shown to occur in a more biophysically realistic conductance—based model (section 4.2.2). In Chapter 5 we extend these results to two-dimensional networks in the presence of a radially-symmetric input.

4.1 Stationary Pulses in an Inhomogeneous Network

We begin by investigating the existence and stability of one–dimensional stationary pulses in the presence of a unimodal input I(x) which, for concreteness, is taken to be a Gaussian of width σ centered at the origin

$$I(x) = \mathcal{I}e^{-x^2/2\sigma^2}. (4.2)$$

We take w to be a positive, even function, monotonically decreasing in |x|, and choose the normalization $\int_{\mathbb{R}} w(x)dx = 1$. For illustrative purposes, the exponential weight distribution (3.57) will be used as a specific example.

4.1.1 Stationary Pulse Existence

From symmetry arguments there exists a stationary pulse solution $(u(x,t), \varrho(x,t)) = (U(x), Q(x))$ of equation (4.1) centered at x = 0, satisfying

$$U(x) > \kappa,$$
 $x \in (-a, a);$ $U(\pm a) = \kappa,$ $U(x) < \kappa,$ $x \in (-\infty, -a) \cup (a, \infty);$ $U(\pm \infty) = 0.$

In particular,

$$(1+\beta)U(x) = \int_{-a}^{a} w(x-x')dx' + I(x), \tag{4.3}$$

$$Q(x) = U(x), (4.4)$$

with $U, Q \in \mathcal{C}^0(\mathbb{R}, \mathbb{R})$, where $\mathcal{C}^n(\mathbb{R}, \mathbb{R})$ denotes the set of all bounded, *n*-times continuously differentiable functions $f : \mathbb{R} \longrightarrow \mathbb{R}$. The threshold κ and width a are related according to the self-consistency condition

$$\hat{\kappa} = [I(a) + W(2a)] \equiv G(a), \tag{4.5}$$

where $\hat{\kappa} = (1 + \beta)\kappa$ and $W(2a) = \int_0^{2a} w(x)dx$. The existence or otherwise of a stationary pulse solution can then be established by finding solutions to

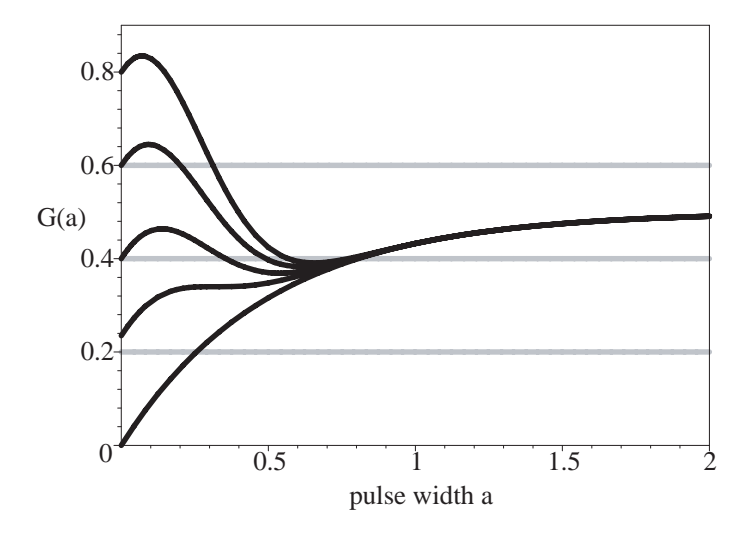


Figure 4.1. Plot of G(a) in (4.5) as a function of pulse width a, for an exponential weight w and various values of input amplitude \mathcal{I} with $\sigma = 0.25$. Horizontal lines represent different values of $\hat{\kappa} = \kappa(1 + \beta)$. Intersections of black and gray curves indicate the existence of stationary pulses.

equation (4.5). Consider, for example, the exponential weight distribution $w(x) = \frac{1}{2}e^{-|x|/d}$ with d = 1 so that $W(2a) = (1 - e^{-2a})/2$. Furthermore, suppose that the amplitude \mathcal{I} of the Gaussian input (4.2) is treated as a bifurcation parameter with the range σ kept fixed. (The effect of varying σ will be discussed below). It is straightforward to show that there always exists a critical amplitude \mathcal{I}_c , below which G(a) is strictly monotonically increasing and above which G(a) has two stationary points. Consequently, as $\hat{\kappa}$ varies, we have the possibility of zero, one, two, or three stationary pulse solutions. The function G(a) is plotted in Figure 4.1 for a range of input amplitudes \mathcal{I} , with horizontal lines indicating different values of $\hat{\kappa}$: intersection points determine the existence of stationary pulse solutions. Let κ_c denote the value of G(a)for which G'(a) has a double zero. Anticipating the stability results of section 4.1.2, we obtain the following. If $\hat{\kappa} < \kappa_c$ then there is only a single pulse solution branch which is always unstable. On the other hand, if $\hat{\kappa} > \kappa_c$, then there are two distinct bifurcation scenarios (see Figure 4.2) both of which can support a stable pulse solution.

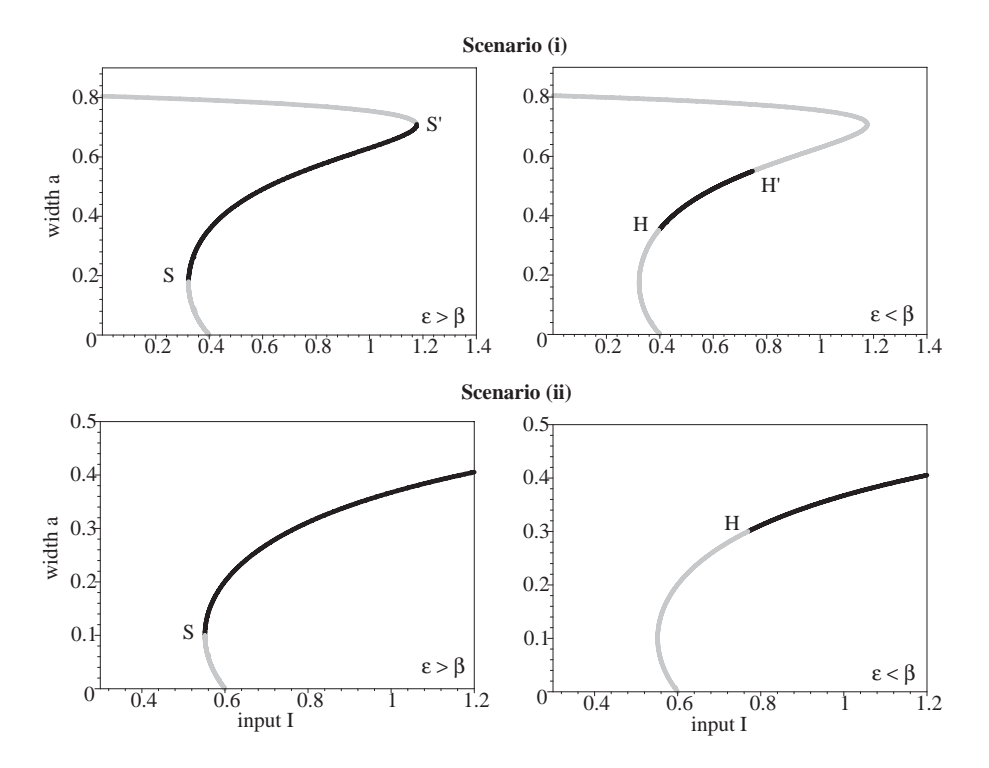


Figure 4.2. One-dimensional stationary pulse existence curves for an exponential weight distribution and (i) $\kappa_c < \hat{\kappa} < \frac{1}{2}$, (ii) $\hat{\kappa} > \frac{1}{2}$. Other parameters are $\beta = 1, \sigma = 0.25$. Black indicates stability, whereas gray indicates instability of the stationary pulse. Saddle–node bifurcation points are indicated by S, S' and Hopf bifurcation points by H, H'.

Scenario (i): $\kappa_c < \hat{\kappa} < 1/2$. There exist three solution branches with the lower (narrow pulse) and upper (wide pulse) branches unstable. If $\epsilon > \beta$, then the middle (intermediate pulse) branch is stable along its entire length, annihilating in a saddle–node bifurcation at the endpoints S, S'. On the other hand, if $\epsilon < \beta$, then only a central portion of the middle branch is stable due to the existence of two Hopf bifurcation points H, H'. In the limit $\epsilon \to \beta$ we have $H \to S$ and $H' \to S'$ leading to some form of degenerate bifurcation. Note that as $\hat{\kappa} \to 1/2$, $a_{S'} \to \infty$ thus causing the upper branch to collapse.

Scenario (ii): $\hat{\kappa} > 1/2$. There exist two solution branches with the lower branch unstable and the upper branch stable for sufficiently large \mathcal{I} . If $\epsilon > \beta$ the upper branch is stable along its entire length, annihilating in a saddle-node bifurcation at its endpoint S. On the other hand, if $\epsilon < \beta$ then the upper branch loses stability via a Hopf bifurcation at the point H with $H \to S$ as $\epsilon \to \beta$.

In both of the above scenarios there also exists a stable subthreshold solution $U(x) = I(x)/(1+\beta)$ when $\mathcal{I} < \hat{\kappa}$. This is coexistent with the lower suprathreshold pulse and the pair annihilate at $\mathcal{I} = \hat{\kappa}$. To address the effect of varying the input σ , consider the case where $\hat{\kappa} < \frac{1}{2}$. As σ decreases, κ_c decreases, widening the $\hat{\kappa}$ -interval for which there exists three stationary pulse solutions: in particular $\kappa_c \to 0$ as $\sigma \to 0$. Conversely, as σ increases, κ_c increases towards $\frac{1}{2}$, thus decreasing the size of the three-pulse regime. For $\hat{\kappa} > \frac{1}{2}$, qualitatively, the bifurcation scenario remains unchanged; the effect of increasing σ is simply to widen the pulse width a. Finally, note that the qualitative behavior of the function G(a), which determines the existence of stationary pulse solutions, follows from the fact that both w(x) and I(x) are monotonically decreasing functions of |x| and are symmetric about x = 0.

4.1.2 Stability Analysis

The stability of a stationary pulse of width a is determined by writing $u(x,t) = U(x) + \bar{\varphi}(x,t)$ and $\varrho(x,t) = Q(x) + \bar{\psi}(x,t)$, with Q(x) = U(x), and expanding equation (4.1) to first-order in $(\bar{\varphi}, \bar{\psi})$. This leads to the linear equation

$$\frac{\partial \bar{\varphi}}{\partial t}(x,t) = -\bar{\varphi}(x,t) + \int_{-\infty}^{\infty} w(x-x')H'(U(x')-\kappa)\bar{\varphi}(x',t)dx' - \beta\bar{\psi}(x,t)$$

$$\frac{1}{\epsilon} \frac{\partial \bar{\psi}}{\partial t}(x,t) = -\bar{\psi}(x,t) + \bar{\varphi}(x,t). \tag{4.6}$$

The spectrum of the associated linear operator is determined by taking $\bar{\varphi}(x,t) = e^{\lambda t} \varphi(x)$ and $\bar{\psi}(x,t) = e^{\lambda t} \psi(x)$, with $\varphi, \psi \in \mathcal{C}^0(\mathbb{R}, \mathbb{C})$, and using the identity

$$\frac{dH(U(x) - \kappa)}{dU} = \frac{\delta(x - a)}{|U'(a)|} + \frac{\delta(x + a)}{|U'(-a)|}$$
(4.7)

where

$$U'(x) = \frac{1}{1+\beta} \left[I'(a) + w(x+a) - w(x-a) \right]$$
 (4.8)

and U'(-a) = -U'(a) > 0. We then obtain the spectral problem

$$\left(\lambda + 1 + \frac{\epsilon \beta}{\lambda + \epsilon}\right) \varphi(x) = \frac{w(x+a)}{|U'(-a)|} \varphi(-a) + \frac{w(x-a)}{|U'(a)|} \varphi(a). \tag{4.9}$$

Note that we have formally differentiated the Heaviside function, which is permissible since it arises inside a convolution. One could also develop the linear stability analysis by considering perturbations of the threshold crossing points along the lines of Amari [1]. Since we are linearizing about a stationary rather than a traveling pulse, we can analyze the spectrum of the linear operator without the recourse to Evans functions.

There exist three types of solutions to equation (4.9). The first consists of functions $\varphi(x)$ that vanish at $x = \pm a$ and $\lambda = \lambda_{\pm}^{\circ}$ with λ_{\pm}° given by

$$\lambda_{\pm}^{\circ} = \frac{-(1+\epsilon) \pm \sqrt{(1+\epsilon)^2 - 4\epsilon(1+\beta)}}{2}.$$
 (4.10)

Note that λ_{\pm}° belong to the essential spectrum, since they have infinite multiplicity; they are always negative and, thus, do not contribute to instabilities. The second consists of solutions of the form $\varphi(x) = A(w(x+a) - w(x-a))$ with λ given by the roots of the equation

$$\lambda + 1 + \frac{\epsilon \beta}{\lambda + \epsilon} = \frac{w(0) - w(2a)}{|U'(a)|}.$$
(4.11)

It follows that $\lambda = \lambda_{\pm}$, where

$$\lambda_{\pm} = \frac{-\Lambda \pm \sqrt{\Lambda^2 - 4(1 - \Gamma)\epsilon(1 + \beta)}}{2},\tag{4.12}$$

with

$$\Lambda = 1 + \epsilon - (1 + \beta)\Gamma,$$
 $\Gamma = \frac{w(0) - w(2a)}{w(0) - w(2a) + D},$ (4.13)

and D = |I'(a)|. Finally, the third type of solution is $\varphi(x) = A(w(x+a) + w(x-a))$ with λ given by the roots of the equation

$$\lambda + 1 + \frac{\epsilon \beta}{\lambda + \epsilon} = \frac{w(0) + w(2a)}{|U'(a)|}.$$
(4.14)

This yields $\lambda = \hat{\lambda}_{\pm}$ where

$$\widehat{\lambda}_{\pm} = \frac{-\widehat{\Lambda} \pm \sqrt{\widehat{\Lambda}^2 - 4(1 - \widehat{\Gamma})\epsilon(1 + \beta)}}{2} \tag{4.15}$$

with

$$\widehat{\Lambda} = 1 + \epsilon - (1 + \beta)\widehat{\Gamma}, \qquad \widehat{\Gamma} = \frac{w(0) + w(2a)}{w(0) - w(2a) + D}. \tag{4.16}$$

A stationary pulse solution will be stable provided that $\Re(\lambda_{\pm})$, $\Re(\widehat{\lambda}_{\pm}) < 0$.

In the limiting case of a homogeneous input, for which D=0, equations (4.12) and (4.15) become

$$\lambda_{-} = 0, \quad \lambda_{+} = \beta - \epsilon \tag{4.17}$$

and

$$\widehat{\lambda}_{\pm} = \frac{-\widehat{\Lambda}_0 \pm \sqrt{\widehat{\Lambda}_0^2 + 4\epsilon(1+\beta)(\widehat{\Gamma}_0 - 1)}}{2}$$
(4.18)

with

$$\widehat{\Lambda}_0 = \epsilon + 1 - (1+\beta)\widehat{\Gamma}_0$$
 $\widehat{\Gamma}_0 = \frac{w(0) + w(2a)}{w(0) - w(2a)}.$ (4.19)

Since $\widehat{\Gamma}_0 > 1$ for finite pulse width a, it follows that $\widehat{\lambda}_+ > 0$ for all parameter values and, hence, a stationary pulse (if it exists) is unstable in the case of the homogeneous network described by equation (4.1). This result is consistent with Amari's previous analysis [1]. He showed that in order to stabilize a stationary pulse within a homogeneous network, it is necessary to include some form of lateral inhibition. If a weak input inhomogeneity is subsequently introduced into the network, then the peak of the activity profile moves to a local maximum of the input where it is pinned.

For a nonzero Gaussian input, the gradient of a stationary pulse is given by D(a) where

$$D(a) = \frac{a\mathcal{I}}{\sigma^2} e^{-a^2/2\sigma^2}.$$
 (4.20)

Using the gradient, we wish to determine the stability of the pulse in terms of the pulse width a, with $a = a(\mathcal{I})$ given by one of the solutions of (4.5) for fixed κ, β . Stability of the stationary pulse corresponds to the following conditions

$$\Gamma, \hat{\Gamma} < 1, \qquad \Lambda, \hat{\Lambda} > 0.$$

However, there are redundancies. By inspection of (4.13), the condition $\Gamma < 1$ is automatically satisfied. The conditions $\Lambda, \hat{\Lambda} > 0$ are equivalent to

$$\Gamma, \widehat{\Gamma} < \frac{1+\epsilon}{1+\beta}$$

and, since $\Gamma < \widehat{\Gamma}$, it follows that the condition on Γ is redundant. Hence, stability of the stationary pulse reduces to the conditions

$$\widehat{\Gamma} < 1,$$
 $\widehat{\Gamma} < \frac{1+\epsilon}{1+\beta},$

in which the latter is redundant for $\epsilon > \beta$, while the former is redundant for $\epsilon < \beta$. These conditions translate in terms of the gradient D as follows

$$\epsilon > \beta$$
: $D(a) > 2w(2a) \equiv D_{SN}(a)$ (4.21)

$$\epsilon < \beta : \qquad D(a) > D_c(a) \tag{4.22}$$

where

$$D_c(a) = 2w(2a) + \left(\frac{\beta - \epsilon}{1 + \epsilon}\right)(w(0) + w(2a)).$$
 (4.23)

We now relate stability of the stationary pulse to the gradient D on different branches of the existence curves shown in Figure 4.2 for w(x) given by the exponential distribution (3.57).

Stability for $\epsilon > \beta$. Equation (4.5) implies that D(a) = 2w(2a) - G'(a). Thus, stability condition (4.21) is satisfied when G'(a) < 0 and not satisfied when G'(a) > 0. Saddle-node bifurcation points occur when G'(a) = 0, i.e., when D(a) passes through D_{SN} , due to the vanishing of a single real eigenvalue $\widehat{\lambda}_+$. We can make the following conclusions about the solution branches. In scenario (i) there are three solution branches. On the lower and upper solution branches, G'(a) > 0, while G'(a) < 0 on the middle branch, indicating that the former are always unstable and that the latter is stable for $\epsilon > \beta$. In scenario (ii) there are two solution branches; using the same arguments, the lower branch is always unstable, while, for $\epsilon > \beta$, the upper branch is stable.

Hopf curves for $\epsilon < \beta$. If $\epsilon < \beta$ then a Hopf bifurcation can occur due to a complex pair of eigenvalues $\widehat{\lambda}_{\pm}$ crossing into the right half complex plane. The Hopf bifurcation point is determined by the condition $\widehat{\Gamma} = (1+\varepsilon)/(1+\beta) < 1$, which is equivalent to the gradient condition $D(a) = D_c(a) > D_{\rm sn}(a)$. It follows that only branches determined to be stable for $\epsilon > \beta$ can undergo a Hopf bifurcation when $\epsilon < \beta$. Moreover, the Hopf bifurcation points coincide with saddle-node bifurcation points precisely at the point $\beta = \epsilon$, where there is a pair of zero eigenvalues suggestive of a codimension 2 Takens-Bogdanov bifurcation. As ϵ decreases from β , we expect the Hopf bifurcation point(s) to traverse these previously stable branches from the saddle-node point(s). In order to illustrate this, we find a relationship for D(a) which does not depend explicitly on \mathcal{I} . Using equation (4.5), the input gradient D can be related as

$$D(a) = |I'(a)|$$

$$= \frac{a}{\sigma^2} I(a)$$

$$= \frac{a}{\sigma^2} \left(\kappa (1+\beta) - W(2a) \right). \tag{4.24}$$

We restrict a here depending on which branch of the existence curve we are considering. In each of the scenarios discussed in section 4.1.1, we examine graphically the crossings of the curves $D(a), D_c(a)$; stability corresponds to $D(a) > D_c(a)$ with Hopf points at $D(a) = D_c(a)$. Figure 4.3 illustrates the generic behavior in these scenarios. The left column presents the graphs of Dand of D_c for different values of ϵ spanning the interval $[0, \beta]$; intersection points indicate Hopf bifurcation points. The right column graphs the corresponding Hopf curves in (a, ϵ) -parameter space. Note that the upper branch in scenario (ii) is always stable for sufficiently large input \mathcal{I} , that is, for large pulse width a. For equation (4.5) implies that $I(a) \sim (1+\beta)\kappa - 1/2$ and hence $D \sim [(1+\beta)\kappa 1/2[(a/\sigma^2) \text{ as } a \to \infty. \text{ Since } \widehat{D}_c(a) \to (\beta - \epsilon)/(1 + \epsilon) \text{ and } e^{-2a} \to 0 \text{ as } a \to \infty,$ it follows that both stability conditions (4.21) and (4.22) are satisfied in this limit. Varying σ does not effect the qualitative behavior of the Hopf bifurcation curves. Since σ only appears in equation (4.24), the effect of increasing σ is to shrink the graph of D by a factor $1/\sigma^2$, causing the Hopf curves in the right column of Figure 4.3 to be stretched downwards, thus increasing the size of the stability region in the (a, ϵ) -plane.

4.2 Numerical Results

In our numerical simulations we use a Runge-Kutta (RK4) scheme with 4000-10000 spatial grid points and time step dt = 0.02, evaluating the integral term by quadrature. Boundary points freely evolve according to the scheme rather than by prescription, and the size of the domain is chosen so that the activity is unaffected by the boundaries. Finer timestep sizes were taken to ensure proper temporal resolution of the period doubling.

4.2.1 Hopf Bifurcation to a Breather

Numerically solving the one-dimensional rate equation (4.1), we find that the Hopf instability of the upper solution branch in bifurcation scenario (ii) induces a breather-like oscillatory pulse solution; see Figure 4.4. Two snapshots of the profile of the breather are shown in Figure 4.5. As the input amplitude \mathcal{I} is slowly reduced below \mathcal{I}_{HB} , the oscillations steadily grow until a new instability point is reached. Interestingly, the breather persists over a range of inputs beyond this secondary instability, except that it now periodically emits pairs of traveling pulses. In fact, such a solution is capable of persisting even when the input is below threshold, that is, for $\mathcal{I} < (1+\beta)\kappa$. One possible explanation of this secondary instability is a subcritical bifurcation causing both the breather and the doubled breather to be unstable. Note that although the homogeneous

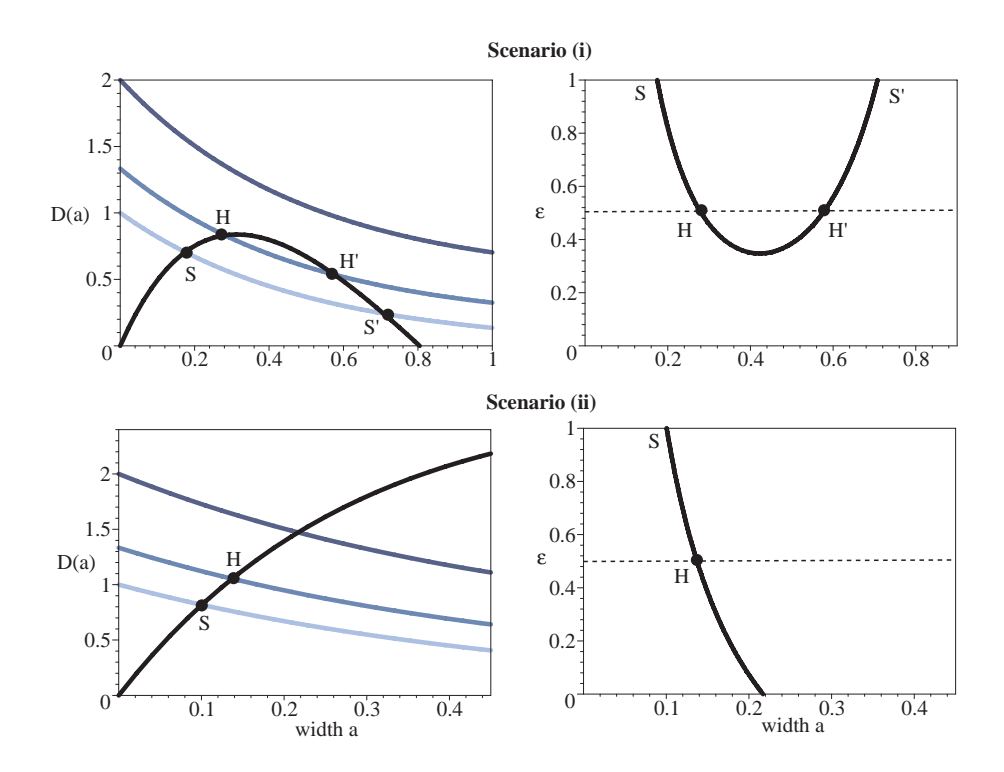


Figure 4.3. Curves describing the relationship between the stability of the stationary pulse and the gradient of the input D. LEFT COLUMN: Gradient curves for the two bifurcation scenarios shown in Figure 4.2: (i) $\kappa_c < \hat{\kappa} < \frac{1}{2}$ and (ii) $\hat{\kappa} > \frac{1}{2}$. The thick solid curve shows the input gradient D(a) as a function of pulse width a. The increasingly lighter curves show the critical gradient $D_c(a)$ as function of a for $\epsilon = 0.0, 0.5, 1.0$ and $\beta = 1$. For a given value of $\epsilon < \beta$, a stationary pulse of width a is stable provided that $D(a) > D_c(a)$. A pulse loses stability via a Hopf bifurcation at any intersection point $D(a) = D_c(a)$. The Hopf bifurcation point(s) for $\epsilon = 0.5$ are indicated by H, H'. In the limit $\epsilon \to \beta$, we have $H, H' \to S, S'$. RIGHT COLUMN: Corresponding Hopf stability curves in the (a, ϵ) -plane.

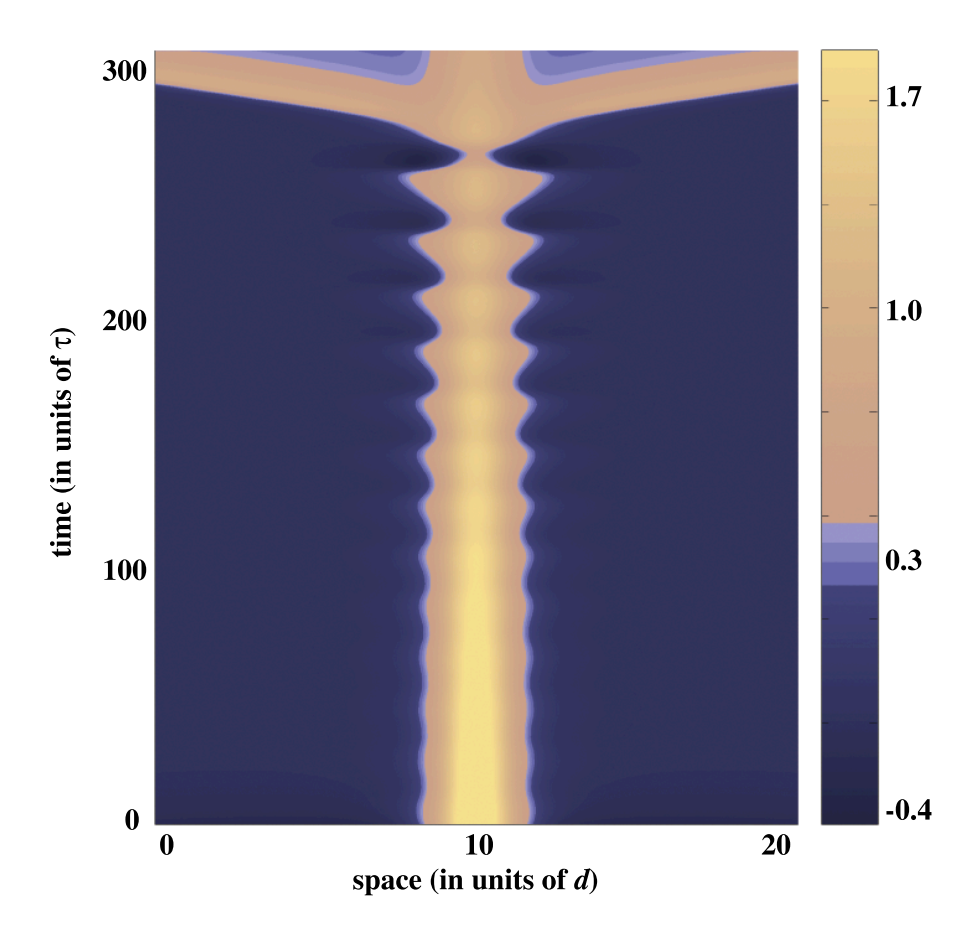


Figure 4.4. Breather-like solution arising from a Hopf instability of a stationary pulse due to a slow reduction in the amplitude \mathcal{I} of the Gaussian input inhomogeneity (4.2) for an exponential weight distribution. Here $\mathcal{I}=5.5$ at t=0 and $\mathcal{I}=1.5$ at t=250. Other parameter values are $\epsilon=0.03, \beta=2.5, \kappa=0.3, \sigma=1.0$. The amplitude of the oscillation steadily grows until it undergoes a secondary instability at $\mathcal{I}\approx 2$, beyond which the breather persists and periodically generates pairs of traveling pulses (only one of which is shown). The breather itself disappears when $\mathcal{I}\approx 1$.

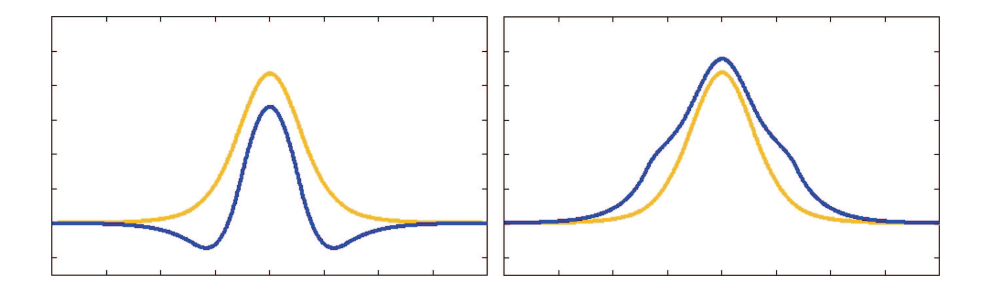


Figure 4.5. Two snapshots of a breather with u in blue and ρ in gold.

network ($\mathcal{I} = 0$) also supports the propagation of traveling pulses, it does not support the existence of a breather that can act as a source of these waves.

Our simulations suggest both supercritical and subcritical Hopf bifurcations can occur for scenario (ii). The conclusion of supercriticality is based on the evidence that there is continuous growth of the amplitude of the oscillations from the stationary solution as \mathcal{I} is reduced through the predicted bifurcation point, and, moreover, that the frequency of the oscillatory solution near the bifurcation point is approximately equal to the predicted Hopf frequency

$$\omega_H = \operatorname{Im} \widehat{\lambda}_{\pm} = \sqrt{\epsilon(\beta - \epsilon)}.$$

For example, the Hopf bifurcation of the stationary pulse for the parameter values given in Figure 4.4 was determined numerically to be supercritical. Conversely, the Hopf bifurcation in scenario (i) appears to be subcritical. Furthermore, the basin of attraction of the stable pulse on the middle branch seems to be small, rendering it, as well as any potential breather, difficult to approach. Hence, we did not investigate this case further.

As mentioned above, a secondary instablity occurs at some $\mathcal{I} < \mathcal{I}_{HB}$, whereupon traveling pulses are emitted; this behavior appears to occur only for values of ϵ that support traveling pulses in the homogeneous model ($\mathcal{I}=0$). As the point of secondary instability is approached, the breather starts to exhibit behavior suggestive of pulse emission, except that the recovery variable q increases rapidly enough to prevent the nascent waves from propagating. On the other hand, beyond the point of instability, recovery is not fast enough to block pulse emission; we also find that that the activity variable u always drops well below threshold after each emission. Interestingly, for a range of input amplitudes we observe frequency-locking between the oscillations of the breather and the rate at which pairs of pulses are emitted from the breather. Two examples of n: m mode-locked solutions are shown in Figure 4.6, in

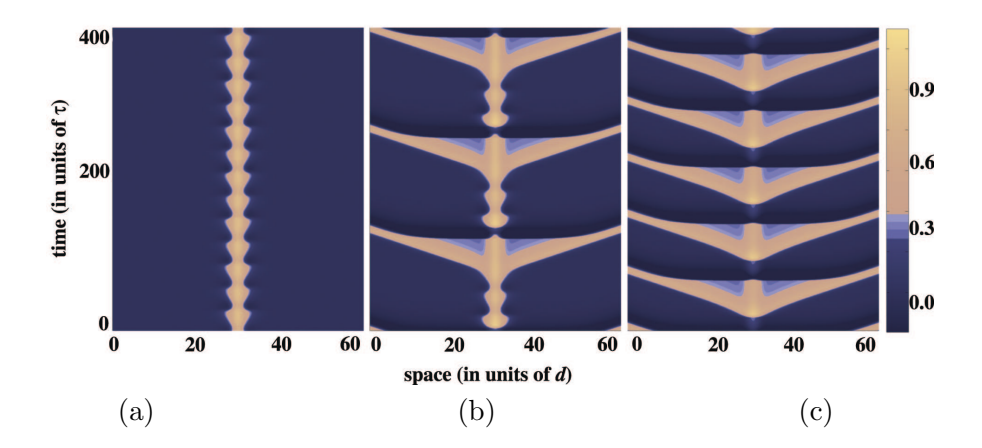


Figure 4.6. Mode locking in the transition from breather to pulse-emitter. (a) 0:1 mode–locking for $\mathcal{I}=2.3$ (b) 1:4 mode–locking for $\mathcal{I}=2.1$ (c) 1:2 mode–locking for $\mathcal{I}=1.3$

which there are n pairs of pulses emitted per m oscillation cycles of the central breather. As \mathcal{I} is reduced further, the only mode that is seen is 1:2, which itself ultimately vanishes and the system is attracted to the subthreshold solution.

Although the above account applies to the case $\sigma = 1/\sqrt{2}$, most features are valid for more general σ . One main point of difference lends insight into the disappearance of the breather. If we consider stationary pulses for $\sigma = 1$ and explore the evolution of the breathing pulse as we futher decrease I_0 beyond the bifurcation point, we find that a secondary bifurcation occurs, giving rise to two modes of breathing rather than one. By graphing, in the (u,ρ) -phase plane, the orbit corresponding to spatial point at the center of the input, we find that the evolution of the orbit, as \mathcal{I} is decreased, strongly resembles that of a period-doubling bifurcation, as shown in Figure 4.7(a,b). Decreasing \mathcal{I} leads to additional period doublings, as illustrated in Figure 4.7(c). Ultimately, decreasing \mathcal{I} leads to similar unstable behavior found for $\sigma = 1/\sqrt{2}$. This suggests that for $\sigma = 1/\sqrt{2}$ the first period-doubling bifurcation may be subcritical and the orbit instead weaves its way around the unstable limit cycle giving rise to the sequence of breathing pulses and emission, as shown in Figure 4.8. Decreasing the input strength \mathcal{I} reduces the number of breathings the system undergoes before the grand excursion associated with emission, until there is solely emission.

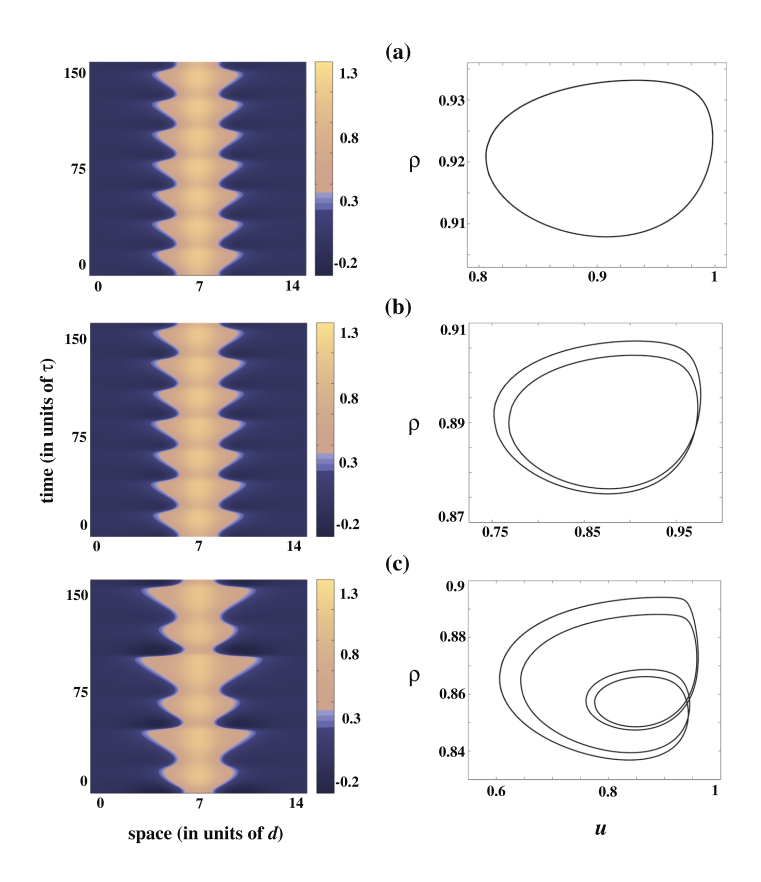


Figure 4.7. Sequence of period-doubling bifurcations of a breathing pulse for $\sigma=1$ and (a) $\mathcal{I}=2.4$, (b) $\mathcal{I}=2.3$, and (c) $\mathcal{I}=2.2$. The left-hand column shows spacetime plots for different values of current amplitude beyond the initial Hopf bifurcation point, with an orbit corresponding to the center spatial point plotted in the (u,q)-phase plane in the right-hand column; other spatial points are qualitatively similar. Other parameter values are $\kappa=0.3$, $\beta=2.5$, $\epsilon=0.03$. (Note that at higher resolution each loop in Figure (c) is actually a pair of closely spaced loops indicating that it corresponds to the third doubling in the sequence).

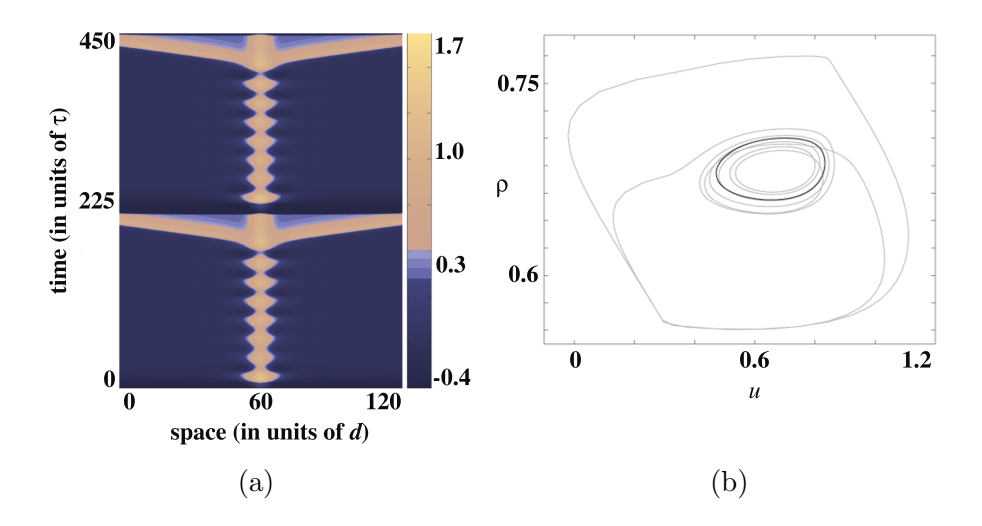


Figure 4.8. Subcritical period-doubling bifurcation to a pulse-emitter. (a) Spacetime plot of a pulse-emitter for $\sigma = 1/\sqrt{2}$, $\mathcal{I} = 1.35$, $\kappa = 0.3$, $\beta = 2.5$ and $\epsilon = 0.03$. (b) Corresponding phase portrait showing the orbit (gray trajectory) of the center spatial point plotted in the (u, ϱ) -phase plane. Also shown is the corresponding orbit (black trajectory) of the stable breather that exists when $\mathcal{I} = 1.4$. The transition from breather to pulse-emitter may result from a subcritical period-doubling bifurcation; in this case the periodic orbit becomes unstable, and the system is attracted to a more complicated periodic orbit. This new orbit has a phase where it appears to weave its way through the (theoretical) unstable periodic orbit, generating the irregularly shaped breathings, followed by the large excursion corresponding to pulse emission.

4.2.2 Breathers in a Biophysical Model

Although the rate model is very useful as an analytically tractable model of neural tissue, it is important to determine whether or not its predictions regarding spatiotemporal dynamics hold in more biophysically realistic conductance—based models. For concreteness, we consider a version of the Traub model, in which there is an additional slow potassium M-current that produces the effect of spike-rate adaptation [23]. The Traub dynamics are responsible for the individual spikes, whereas the termination of the packet of spikes is caused by slow activation of the potassium M-current. Comparison with the firing rate model is made by considering how frequently each neuron spikes.

We discretize space by setting $x = j\Delta x$ for j = 1, ..., N, and label neurons by index j. The membrane potential of the jth neuron satisfies Hodgkin-Huxley like dynamics [23]:

$$C\frac{dV_j}{dt} = -I_{\text{ion}}(V_j, m, n, h, q) - I_j^{\text{syn}}(t) + I_j$$

with synaptic current

$$I_j^{\text{syn}}(t) = g_{\text{syn}} \sum_k w(|j-k|) s_k(t) (V - V_{\text{syn}})$$
$$\frac{ds_j}{dt} = K(V_j(t)) (1 - s_j) - \frac{1}{\tau} s_j$$

and ionic currents

$$I_{ion}(V, m, n, h) = g_{\rm L}(V - V_{\rm L}) + g_{\rm K} n^4 (V - V_{\rm K}) + g_{\rm Na} m^3 h(V - V_{\rm Na}) + g_q q(V - V_{\rm K})$$

$$\tau_p(V) \frac{dp}{dt} = p_{\infty}(V) - p \qquad p \in \{m, n, h, q\}$$

The various biophysical model functions and the parameters used in the numerics are listed in Appendix A. Note that we have also included an external Gaussian input current I_j in order to investigate the behavior predicted by the rate model. Without this external input, the biophysical model has previously been shown to support a traveling pulse, consisting of either a single action potential or a packet of action potentials [23]. Since the firing rate model describes the average activity, we interpret high activity as repetitive firing of neurons and low activity as neurons that are subthreshold or quiescent. Hence, we expect that the application of a strong unimodal input should generate a stationary pulse, i.e., a localized region of neurons that are repetitively firing, surrounded by a region of neurons that are quiescent. Subsequent reduction of the input should lead to oscillations in this localized region followed by emission of packets of action potentials.

One obvious difference between this biophysical model and the rate model discussed in section 4.1 is that the gating variable associated with spike-rate adaptation evolves according to more complicated nonlinear dynamics, while that of the firing rate model evolves according to simple linear dynamics. Nevertheless, the behavior of the rate model appears to carry over to the biophysical model, thus lending support to the ability of rate models to describe the averaged behavior of spiking biophysical models. For large input amplitude \mathcal{I} , the system approaches a solution in which a region, localized about the input, is repetitively firing, while the outer region is quiescent; moreover, the firing rate is maximal in the center of this region and decreases towards the

boundaries, which is analogous to the stationary pulse of the firing rate model. As $\mathcal I$ is subsequently decreased, there is a transition to breather-like behavior; periodically, packets or bursts of action potentials begin to propagate from the active region and, shortly thereafter, fail to propagate as the newly excited region recovers. As in the rate model, further reduction of the amplitude $\mathcal I$ leads to a transition to a state in which packets of persistent action potentials are emitted. Two examples are shown in Figure 4.9. The first is in a regime where the breather still dominates with the occasional emission of wave packets.

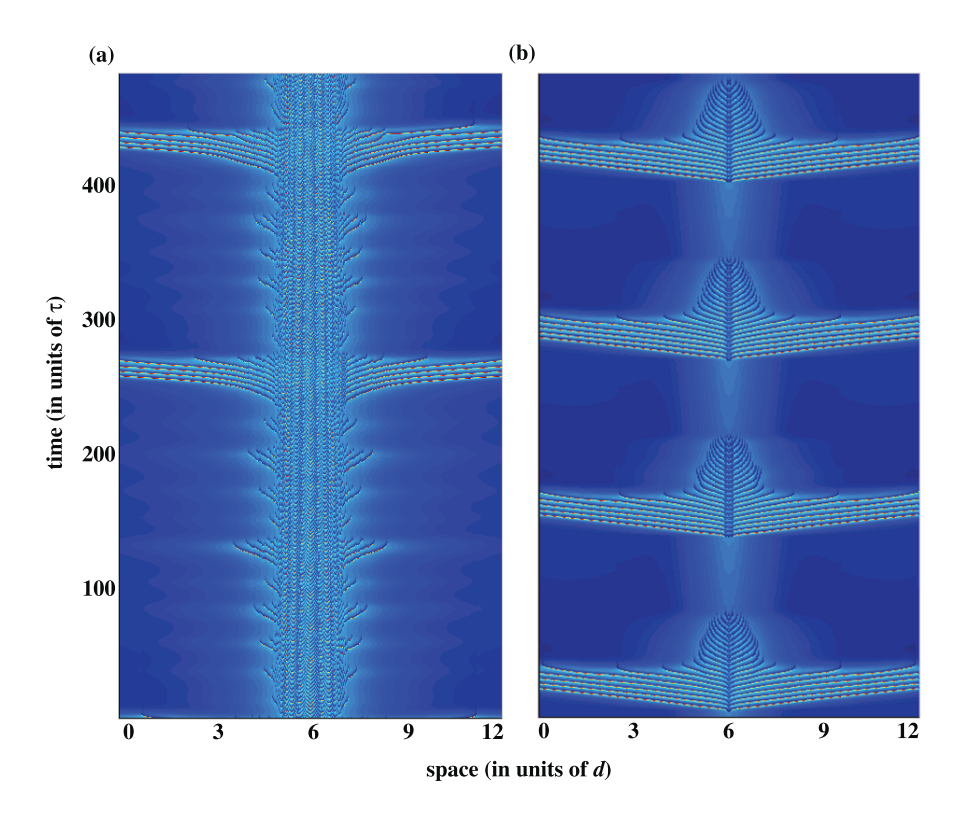


Figure 4.9. Breathers in a biophysical model with an exponential weight distribution. (a) $\mathcal{I} = 75 \text{mA/cm}^2$ (b) $\mathcal{I} = 50 \text{mA/cm}^2$ where \mathcal{I} is the amplitude of the Gaussian input. Other parameter values are specified in Appendix A.

The second corresponds to regular pulse emission, in which periodic bursts of persistent action potentials are emitted, each followed by an interlude of subthreshold behavior in the vicinity of the input; this is similar to the 1:2 pulse-emitter of the firing rate model shown in Figure 4.6. We expect similar behavior to occur in other biophysical models endowed with some form of slow negative feedback.

4.3 Discussion

In this chapter we have shown that a localized external input can induce oscillatory behavior in an excitatory neural network in the form of breathing pulses, and that these breathers can subsequently act as sources of wave emission. Interestingly, following some initial excitation, breathers can be supported by subthreshold inputs. From a mathematical perspective, there are a number of directions for future work. First, one could try to develop some form of weakly nonlinear analysis in order to determine analytically whether or not the Hopf instability of the stationary pulse is supercritical or subcritical. It would also be interesting to explore more fully the behavior around the degenerate bifurcation point $\epsilon = \beta$, where there exists a pair of zero eigenvalues of the associated linear operator that is suggestive of a Takens-Bogdanov bifurcation. The latter would predict that for certain parameter values around the degenerate bifurcation point, the periodic orbit arising from the Hopf bifurcation could be annihilated in a homoclinic bifurcation associated with another unstable stationary pulse. It could be, however, that the homoclinic bifurcation occurs on the periodic orbit that is rendered unstable by the period-doubling bifurcation. This would agree with the fact that no evidence was found indicating the period elongation which characteristic of orbits near a homoclinic bifurcation point.

We have established that the combined effect of local inhomogeneities and recurrent synaptic interactions can result in nontrivial forms of coherent oscillations and waves. Although we have focused on rather abstract neural field equations, we have shown that our results carry over (at least qualitatively) to a more biophysically realistic conductance—based model. One of the advantages of studying simplified models is that it can generate predictions regarding how dynamical properties, such as wave speed, depend on characteristic features of neural tissue. As demonstrated by Schiff et al. in a recent study of wave propagation in disinhibited cortical slices, the speed of the wave can be controlled by external electric fields, confirming predictions determined by the same homogeneous neural field model [87]. Our own work predicts that coherent oscillations can be induced by local inhomogeneities. Such inhomogeneities could arise from external stimuli or reflect changes in the excitability of local populations of neurons. The former suggests a network mechanism for stimulus—induced

oscillations, which may play an important role in visual processing [41, 95], whereas the latter suggests a network mechanism for generating epileptiform activity.

It would be interesting to test our predictions—wave propagation failure and the existence of breathers and/or pulse-emitters—in disinhibited cortical slice experiments inducing localized inputs with electrodes. One of the potential difficulties in experimentally testing our predictions regarding input—induced coherent oscillations in cortical slices is that persistent currents tend to burn out (destroy) neurons. Although it might be possible to circumvent this problem using other forms of stimulation such as external electric fields [87], an alternative strategy is to consider the effects of moving stimuli, which are analyzed in Chapter 6. This is also more realistic from the perspective of the intact cortex, which is constantly being bombarded by nonstationary sensory inputs.

CHAPTER 5

BREATHERS IN TWO-DIMENSIONAL NEURAL NETWORKS

5.1 Two-dimensional pulses

We now extend our analysis to derive conditions for the existence and stability of radially symmetric stationary pulse solutions of a two-dimensional version of equation (4.1):

$$\frac{\partial u}{\partial t}(\mathbf{r},t) = -u(\mathbf{r},t) + \int_{\mathbb{R}^2} w(|\mathbf{r} - \mathbf{r}'|) H(u(\mathbf{r}',t) - \kappa) d\mathbf{r}' - \beta \varrho(\mathbf{r},t) + I(r)$$

$$\frac{1}{\epsilon} \frac{\partial \varrho}{\partial t}(\mathbf{r},t) = -\varrho(\mathbf{r},t) + u(\mathbf{r},t).$$
(5.1)

where $\mathbf{r}=(r,\theta)$ and $\mathbf{r}'=(r',\theta')$. The radially symmetric input I(r) is taken to be a positive, monotonically decreasing function which decays to zero at infinity. The weight distribution is taken to be either a positive, monotonically decreasing weight function or a Mexican hat weight function, such that $\int_{\mathbb{R}^2} w(\mathbf{r}) d\mathbf{r} < \infty$. As in the one–dimensional case, stationary pulse solutions are unstable in a homogeneous excitatory network but can be stabilized by the local input. Our analysis should be contrasted with a number of recent studies of two–dimensional stationary pulses [101, 107, 62]. These latter studies consider homogeneous networks with spatially homogeneous external inputs and do not include adaptation. In contrast to the excitatory weight function, the Mexican hat weight function has the ability to generate breathers which are not radially symmetric.

5.1.1 Stationary Pulse Existence

We begin by developing a formal representation of the two-dimensional stationary pulse solution for a general, monotonically decreasing weight function w. We then generate stationary-pulse existence curves for the specific case of an

exponential weight function, and analyze their dependence on the parameters of the system. Since we cannot obtain a closed-form for the solution in the case of the exponential weight distribution, we also derive an explicit solution for the case of a modified Bessel weight function that approximates the exponential. For concreteness, we consider a Gaussian input $I(r) = \mathcal{I}e^{-r^2/2\sigma^2}$. We furthermore consider pulses generated by a Mexican hat weight function derived from a difference of modified Bessel weight functions; the corresponding model arises from a two-population Wilson-Cowan type model where the excitatory population is modulated by slow adaptation and the inhibitory population evolves on a fast timescale (GABA_A), rendering it in quasi-steadystate.

5.1.2 General, Positive Synaptic Weight Distribution

A radially symmetric stationary pulse solution of equation (5.1) is $u = \varrho = U(r)$ with U depending only upon the spatial variable r such that

$$U(r) > \kappa, \quad r \in (0, a);$$
 $U(\infty) = 0,$ $U(a) = \kappa;$ $U(0) < \infty,$ $U(r) < \kappa, \quad r \in (a, \infty).$

Substituting into equation (5.1) gives

$$(1+\beta)U(r) = M(a,r) + I(r)$$
 (5.2)

where

$$M(a,r) = \int_{\mathbb{R}^2} w(|\mathbf{r} - \mathbf{r}'|) H(U(r') - \kappa) d\mathbf{r}'$$
$$= \int_0^{2\pi} \int_0^a w(|\mathbf{r} - \mathbf{r}'|) r' dr' d\theta. \tag{5.3}$$

In order to calculate the double integral in (5.3) we use the Fourier transform, which for radially symmetric functions reduces to a Hankel transform. To see this, consider the two-dimensional Fourier transform of the radially symmetric weight function w, expressed in polar coordinates,

$$\begin{split} w(r) &= \frac{1}{2\pi} \int_{\mathbb{R}^2} \mathrm{e}^{i(\mathbf{r} \cdot \mathbf{k})} \breve{w}(\mathbf{k}) d\mathbf{k} \\ &= \frac{1}{2\pi} \int_0^\infty \left(\int_0^{2\pi} \mathrm{e}^{ir\rho\cos(\theta - \phi)} \breve{w}(\rho) d\phi \right) \rho d\rho, \end{split}$$

where \check{w} denotes the Fourier transform of w and $\mathbf{k} = (\rho, \phi)$. Using the integral representation

$$\frac{1}{2\pi} \int_0^{2\pi} e^{ir\rho\cos(\theta - \varphi)} d\theta = J_0(r\rho),$$

where $J_{\nu}(z)$ is the Bessel function of the first kind, we express w in terms of its Hankel transform of order zero,

$$w(r) = \int_0^\infty \check{w}(\rho) J_0(r\rho) \rho d\rho \tag{5.4}$$

which, when substituted into equation (5.3), gives

$$M(a,r) = \int_0^{2\pi} \int_0^a \left(\int_0^\infty reve{w}(
ho) J_0(
ho | \mathbf{r} - \mathbf{r}' |)
ho d
ho
ight) r' dr' d heta'.$$

Switching the order of integration gives

$$M(a,r) = \int_0^\infty \check{w}(\rho) \left(\int_0^{2\pi} \int_0^a J_0(\rho |\mathbf{r} - \mathbf{r}'|) r' dr' d\theta' \right) \rho d\rho.$$
 (5.5)

In polar coordinates $|\mathbf{r} - \mathbf{r}'| = \sqrt{r^2 + {r'}^2 - 2rr'\cos(\theta - \theta')}$, then

$$\begin{split} \int_0^{2\pi} \int_0^a J_0(\rho|\mathbf{r} - \mathbf{r}'|) r' dr' d\theta' &= \int_0^{2\pi} \int_0^a J_0\left(\rho \sqrt{r^2 + r'^2 - 2rr'\cos(\theta - \theta')}\right) r' dr' d\theta' \\ &= \frac{1}{\rho^2} \int_0^{2\pi} \int_0^{a\rho} J_0\left(\sqrt{R^2 + R'^2 - 2RR'\cos(\theta')}\right) R' dR' d\theta' \end{split}$$

where $R = r\rho$ and $R' = r'\rho$. To separate variables, we use the addition theorem

$$J_0\left(\sqrt{R^2 + R'^2 - 2RR'\cos\theta'}\right) = \sum_{m=0}^{\infty} \epsilon_m J_m(R) J_m(R') \cos m\theta'$$

where $\epsilon_0 = 1$ and $\epsilon_n = 2$ for $n \ge 1$. Since $\int_0^{2\pi} \cos m\theta' d\theta' = 0$ for $m \ge 1$, it follows that

$$\int_0^{2\pi} \int_0^a J_0(\rho | \mathbf{r} - \mathbf{r}' |) r' dr' d\theta' = \frac{1}{\rho^2} \sum_{m=0}^{\infty} \epsilon_m J_m(R) \int_0^{a\rho} J_m(R') R' dR' \int_0^{2\pi} \cos m\theta' d\theta'$$

$$= \frac{2\pi}{\rho^2} J_0(R) \int_0^{a\rho} J_0(R') R' dR'$$

$$= \frac{2\pi a}{\rho} J_0(r\rho) J_1(a\rho).$$

Hence for general weight w, M(a,r) has the formal representation

$$M(a,r) = 2\pi a \int_0^\infty \check{w}(\rho) J_0(r\rho) J_1(a\rho) d\rho. \tag{5.6}$$

We now show that for a general, positive, monotonically decreasing weight function w(r), the function M(a,r) is necessarily a monotonically decreasing function of r. This ensures that the radially symmetric stationary pulse solution (5.2) is also a monotonically decreasing function of r in the case of a Gaussian input. Differentiating M with respect to r using equation (5.3) yields

$$\frac{\partial M}{\partial r}(a,r) = \int_0^{2\pi} \int_0^a w'(|\mathbf{r} - \mathbf{r}'|) \left(\frac{r - r'\cos(\theta')}{\sqrt{r^2 + r'^2 - 2rr'\cos(\theta')}}\right) r'dr'd\theta'. \quad (5.7)$$

By inspection of (5.7), $\frac{\partial M}{\partial r}(a,r) < 0$ for r > a, since w'(z) < 0. To see that it is also negative for r < a, we instead consider the equivalent Hankel representation of equation (5.6). Differentiation of M in this case yields

$$\partial_2 M(a,r) \equiv \frac{\partial M}{\partial r}(a,r) = -2\pi a \int_0^\infty \rho \check{w}(\rho) J_1(r\rho) J_1(a\rho) d\rho \tag{5.8}$$

implying that

$$\operatorname{sgn}(\partial_2 M(a,r)) = \operatorname{sgn}(\partial_2 M(r,a)).$$

Consequently $\frac{\partial M}{\partial r}(a,r) < 0$ also for r < a. Hence U is monotonically decreasing in r for any monotonic synaptic weight function w.

5.1.3 Exponential Weight Distribution

Consider the radially-symmetric exponential weight and Hankel representation

$$w(r) = \frac{1}{2\pi} e^{-r}, \qquad \check{w}(r) = \frac{1}{2\pi} \frac{1}{(1+\rho^2)^{\frac{3}{2}}}.$$
 (5.9)

The condition for the existence of a stationary pulse is then given by

$$(1+\beta)\kappa = \mathbf{M}(a) + I(a) \equiv G(a), \tag{5.10}$$

where

$$\mathbf{M}(a) \equiv M(a, a)$$

$$= a \int_{0}^{\infty} \frac{1}{(\rho^{2} + 1)^{\frac{3}{2}}} J_{0}(a\rho) J_{1}(a\rho) d\rho$$

$$= \left(\frac{1}{2} - \frac{1}{2} I_{0}(2a) + a I_{1}(2a)\right) - \left(\frac{2a}{\pi} - \frac{1}{2} \mathbf{L}_{0}(2a) + a \mathbf{L}_{1}(2a)\right)$$
 (5.12)

 I_{ν} is a modified Bessel function and \mathbf{L}_{ν} is a modified Struve function [106].

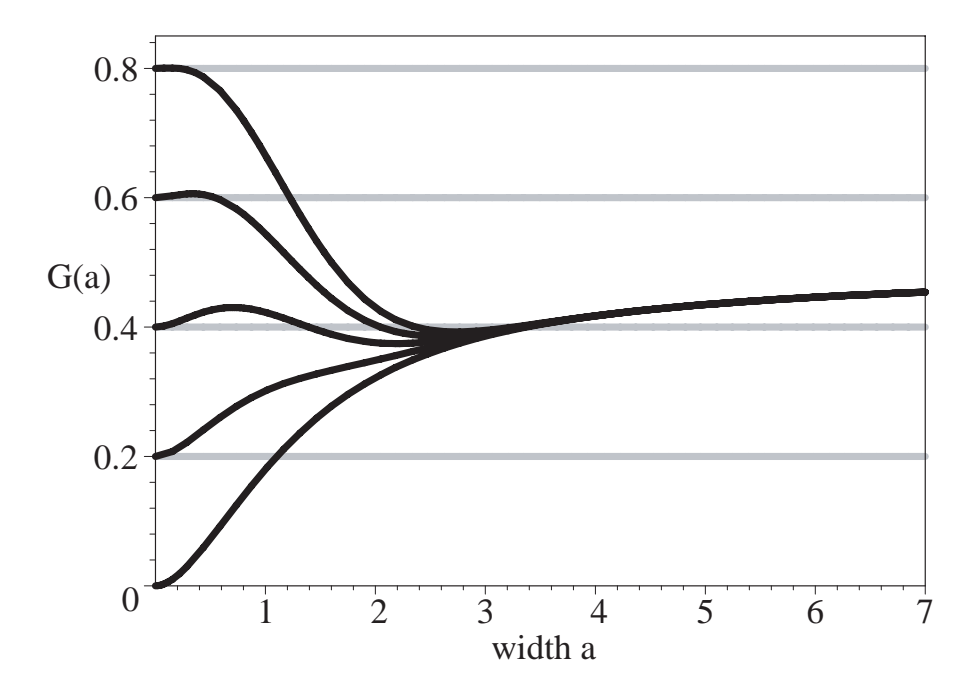


Figure 5.1. Plot of G(a) defined in equation (5.10) as a function of pulse width a for various values of input amplitude \mathcal{I} and for fixed input width $\sigma = 1$.

Proceeding in the same fashion as the one-dimensional case, stationary pulse existence curves for the exponential weight function are determined by intersections of the graphs of G(a) and $\hat{\kappa}$, which are shown in Figure 5.1. Qualitatively the catalogue of bifurcation scenarios is similar, although there is now an additional case. In one dimension we have G'(0)>0 so that there are always at least two solution branches when $\hat{\kappa}>1/2$. On the other hand, in two dimensions we have G'(0)<0 for sufficiently large input amplitude \mathcal{I} , so that it is possible to find only one solution branch for large $\hat{\kappa}$, that is, when $\hat{\kappa}>\kappa_0$ for some critical value $\kappa_0>1/2$. Hence, there are three distinct cases as shown in Figure 5.2. The effect of varying σ follows identically to the one-dimensional case.

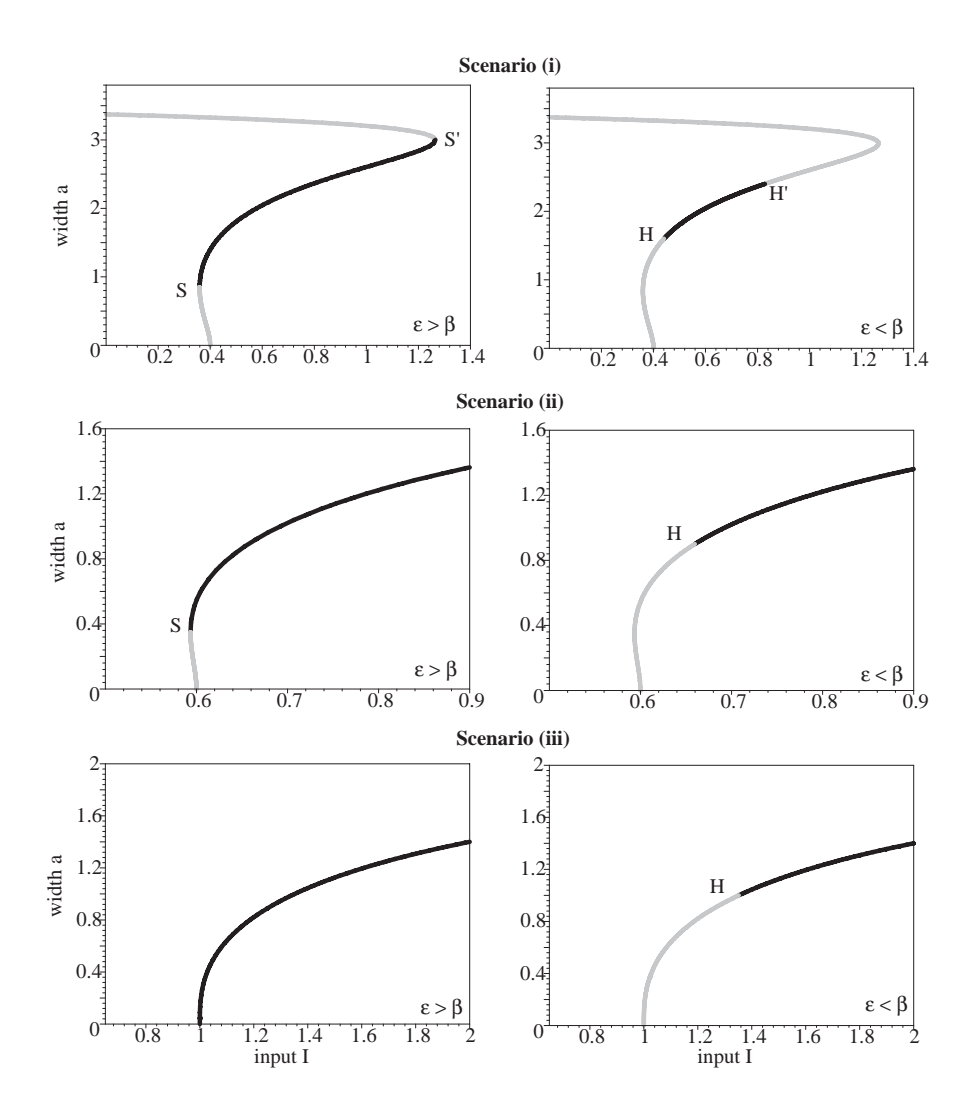


Figure 5.2. Two-dimensional stationary pulse existence curves for an exponential weight distribution: (i) $\kappa_c < \hat{\kappa} < \frac{1}{2}$, (ii) $\frac{1}{2} < \hat{\kappa} < \kappa_0$ and (iii) $\kappa_0 < \hat{\kappa}$. Other parameter values are $\beta = 1, \sigma = 1.0$. Black indicates stability whereas gray indicates instability of the stationary pulse. Saddle-node bifurcation points are indicated by S, S' and Hopf bifurcation points by H, H'.

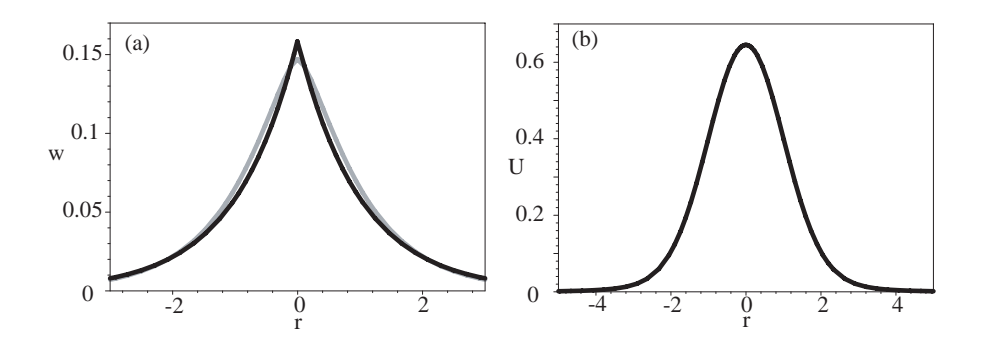


Figure 5.3. Radially symmetric weight functions and corresponding stationary pulse. (a) Synaptic weight functions, exponential weight in black and modified Bessel weight in gray. (b) Stationary pulse solution with half-width, a = 1, generated by the modified Bessel weight function with $\kappa = 0.4$, $\beta = 1$, $\mathcal{I} = 1$.

5.1.4 Positive Modified Bessel Weight Distribution

In the case of the exponential weight function w we do not have a closed-form for the integral in (5.6). Here we consider a nearby problem where we are able to construct the stationary pulse solution explicitly. Consider the radially-symmetric weight function, normalized to unity,

$$w_{\scriptscriptstyle \mathrm{K}}(r) = K_{\scriptscriptstyle 0}\left(\frac{r}{s}\right) - K_{\scriptscriptstyle 0}\left(\frac{2r}{s}\right).$$

where K_{ν} is the modified Bessel function of the second kind, whose Hankel transform is

$$\check{w}_{\kappa}(r) = \frac{2}{3\pi} \left(\frac{1}{\rho^2 + 1} - \frac{1}{\rho^2 + 2^2} \right).$$
(5.13)

The coefficient $2/3\pi$ is chosen so that there is a good fit with the exponential distribution as shown in Figure 5.3(a). Note that

$$w(0) = \frac{1}{2\pi} \frac{4 \ln(2)}{3} \approx \frac{1}{2\pi} (0.924), \qquad w(r) \sim \frac{1}{3} \left(\frac{\sqrt{2} \mathrm{e}^{-r} - \mathrm{e}^{-2r}}{\sqrt{r}} \right) \quad \text{for large } r.$$

The modified Bessel weight has the additional advantage of providing simpler expressions for many of the functions associated with the linear stability analysis of the stationary pulse solution.

Substituting equation (5.13) into equation (5.3), we can explicitly compute the resulting integral in terms of modified Bessel functions:

$$a\int_{0}^{\infty} \frac{1}{\rho^{2} + s^{2}} J_{0}(r\rho) J_{1}(a\rho) d\rho = \begin{cases} \frac{a}{s} I_{1}\left(sa\right) K_{0}\left(sr\right), & \text{for } r \geq a \\ \frac{1}{s^{2}} - \frac{a}{s} I_{0}\left(sr\right) K_{1}\left(sa\right), & \text{for } r < a \end{cases}$$

where I_{ν} is the modified Bessel function of the first kind. Substituting into equation (5.3) shows that

$$\begin{split} M(a,r) &= 2\pi a \int_0^\infty \check{w}(\rho) J_0(r\rho) J_1(a\rho) d\rho \\ &= \frac{4}{3} a \int_0^\infty \left(\frac{1}{\rho^2 + 1} - \frac{1}{\rho^2 + 2^2} \right) J_0(r\rho) J_1(a\rho) d\rho \\ &= \begin{cases} \frac{2}{3} \left(2a I_1\left(a\right) K_0\left(r\right) - I_1\left(2a\right) K_0\left(2r\right) \right) & \text{for } r \geq a \\ \\ 1 - \frac{2}{3} \left(2a I_0\left(r\right) K_1\left(a\right) - I_0\left(2r\right) K_1\left(2a\right) \right) & \text{for } r < a. \end{cases} \end{split}$$

The condition for the existence of a stationary pulse of radius a is thus given by equation (5.10) with

$$\mathbf{M}(a) = \frac{2}{3} \left(2aI_1(a) K_0(a) - I_1(2a) K_0(2a) \right).$$
 (5.14)

An example of an exact pulse solution is shown in Figure 5.3(b).

5.1.5 Mexican Hat Weight Function

Consider the positive modified Bessel weight function from the previous section

$$w_{\text{\tiny K}}\left(r,s\right) = K_{\text{\tiny 0}}\left(\frac{r}{s}\right) - K_{\text{\tiny 0}}\left(\frac{2r}{s}\right).$$

For appropriately chosen parameters the weight function

$$w(r) = \frac{2}{3\pi} \left[\frac{a_e}{\sigma_e^2} w_K(r, \sigma_e) - \frac{a_i}{\sigma_i^2} w_K(r, \sigma_i) \right]$$
 (5.15)

defines a Mexican hat comparable to that generated by the exponential function. Although M(a,r) is no longer monotonically decreasing in r, the profile may be checked graphically to ensure the threshold behavior is satisfied.

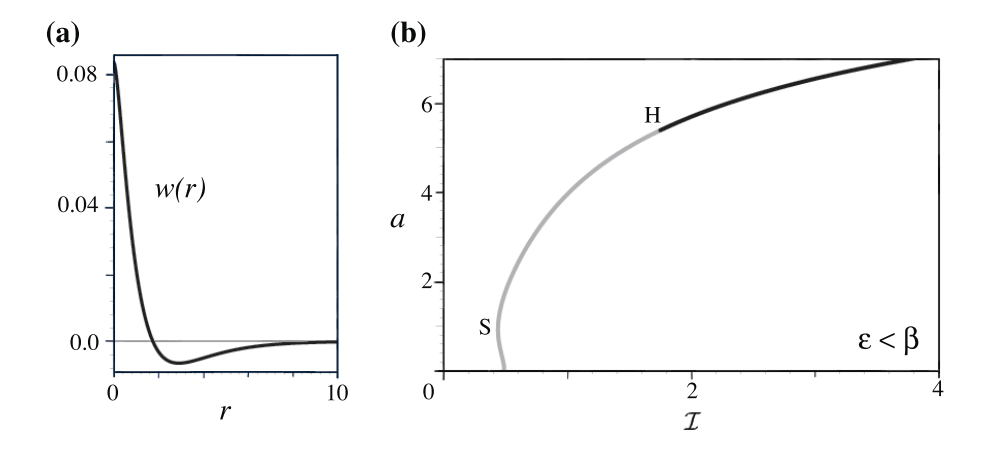


Figure 5.4. (a) Plot of the Mexican hat weight function w for $a_e = 1$, $\sigma_e = 1$, $a_i = 1.4$, $\sigma_i = 1.8$. (b) Corresponding pulse existence curves with black (gray) indicating stability (instability) of the stationary pulse solution. S and H indicate saddle-node and Hopf bifurcation points, respectively. Other parameters are $\kappa = 0.15$, $\beta = 2.25$, $\epsilon = 0.03$, $\sigma = 2.4$.

The profile of the pulse is given by (5.2), where the synaptic term is

$$M(a,r) = a_e M^{\circ} \left(a, r, \frac{1}{\sigma_e} \right) - a_i M^{\circ} \left(a, r, \frac{1}{\sigma_i} \right)$$
 (5.16)

and

$$M^{\circ}(a,r;s) = \begin{cases} \frac{2}{3}sa \left[2I_{1}(sa) K_{0}(sr) - I_{1}(2sa) K_{0}(2sr) \right], & r \geq a, \\ 1 - \frac{2}{3}sa \left[2I_{0}(sr) K_{1}(sa) - I_{0}(2sr) K_{1}(2sa) \right], & r < a. \end{cases}$$
(5.17)

The threshold condition for existence again is given by

$$\kappa(1+\beta) = M(a,a) + I(a),$$

with

$$M^{\circ}(a, r; s) = \frac{2}{3} sa \left[2I_{1}(sa) K_{0}(sa) - I_{1}(2sa) K_{0}(2sa) \right].$$

5.2 Stability Analysis

We now analyze the evolution of small time-dependent perturbations of the stationary pulse solution through linear stability analysis. We investigate saddle-node and Hopf bifurcations of the stationary pulse by relating the eigenvalues to the gradient of the Gaussian input I. The behavior of the system near and beyond the Hopf bifurcation is then studied numerically as in one dimension.

5.2.1 Spectral Analysis of the Linearized Operator

Equation (5.1) is linearized about the stationary solution (U, Q), by introducing the time-dependent perturbations

$$u(\mathbf{r},t) = U(r) + \bar{\varphi}(\mathbf{r},t)$$
$$\bar{\varrho}(\mathbf{r},t) = Q(r) + \bar{\psi}(\mathbf{r},t)$$

with Q=U, and expanding to first order in $\bar{\varphi}, \bar{\psi}$. This leads to the linear system of equations

$$\frac{\partial \bar{\varphi}}{\partial t}(\mathbf{r},t) = -\bar{\varphi}(\mathbf{r},t) + \int_{\mathbb{R}^2} w(|\mathbf{r} - \mathbf{r}'|) H'(U(r') - \kappa) \bar{\varphi}(\mathbf{r}',t) d\mathbf{r}' - \beta \bar{\psi}(\mathbf{r},t),$$

$$\frac{1}{\epsilon} \frac{\partial \bar{\psi}}{\partial t}(\mathbf{r},t) = -\bar{\psi}(\mathbf{r},t) + \bar{\varphi}(\mathbf{r},t).$$

We separate variables

$$\bar{\varphi}(\mathbf{r},t) = \varphi(\mathbf{r})e^{\lambda t}, \qquad \bar{\psi}(\mathbf{r},t) = \psi(\mathbf{r})e^{\lambda t},$$

where $\varphi, \psi \in \mathcal{C}^0(\mathbb{R}^2, \mathbb{C}^2)$, to obtain the system

$$\lambda \varphi(\mathbf{r}) = -\varphi(\mathbf{r}) + \int_{\mathbb{R}^2} w(|\mathbf{r} - \mathbf{r}'|) H'(U(r') - \kappa) \varphi(\mathbf{r}') d\mathbf{r}' - \beta \psi(\mathbf{r})$$

$$\frac{\lambda}{\epsilon} \psi(\mathbf{r}) = -\psi(\mathbf{r}) + \varphi(\mathbf{r}). \tag{5.18}$$

Solving equation (5.18) we find

$$\left(\lambda + 1 + \frac{\beta \epsilon}{\lambda + \epsilon}\right) \varphi(\mathbf{r}) = \int_{\mathbb{R}^2} w(|\mathbf{r} - \mathbf{r}'|) H'(U(r') - \kappa) \varphi(\mathbf{r}') d\mathbf{r}'. \tag{5.19}$$

Introducing polar coordinates $\mathbf{r} = (r, \theta)$ and using the result

$$H'(U(r) - \kappa) = \delta(U(r) - \kappa) = \frac{\delta(r - a)}{|U'(a)|},$$

we obtain

$$\left(\lambda + 1 + \frac{\epsilon \beta}{\lambda + \epsilon}\right) \varphi(\mathbf{r}) = \int_0^{2\pi} \int_0^\infty w(|\mathbf{r} - \mathbf{r}'|) \frac{\delta(r' - a)}{|U'(a)|} \varphi(\mathbf{r}') r' dr' d\theta'$$

$$= \frac{a}{|U'(a)|} \int_0^{2\pi} w(|\mathbf{r} - \mathbf{a}'|) \varphi(a, \theta') d\theta', \qquad (5.20)$$

where $\mathbf{a}' = (a, \theta')$

We consider the following two cases. (i) The function φ satisfies the condition

$$\int_0^{2\pi} w(|\mathbf{r} - \mathbf{a}'|)\varphi(a, \theta')d\theta' = 0$$

for all r. The integral equation reduces to

$$\lambda + 1 + \frac{\beta \epsilon}{\lambda + \epsilon} = 0,$$

yielding

$$\lambda_{\pm}^{\circ} = \frac{-(1+\epsilon) \pm \sqrt{(1+\epsilon)^2 - 4\epsilon(1+\beta)}}{2}.$$

This is part of the essential spectrum and is identical to the one-dimensional case; it is negative and does not cause instability. (ii) φ does not satisfy the above condition, and we must study the solutions of the integral equation

$$\mu\varphi(r,\theta) = a \int_0^{2\pi} \mathcal{W}(a,r;\theta - \theta')\varphi(a,\theta')d\theta', \tag{5.21}$$

where

$$\lambda + 1 + \frac{\epsilon \beta}{\lambda + \epsilon} = \frac{\mu}{|U'(a)|} \tag{5.22}$$

and $\mathcal{W}(a, r; \phi) = w\left(\sqrt{r^2 + a^2 - 2ra\cos\phi}\right)$. This equation demonstrates that $\varphi(r, \theta)$ is determined completely by its values $\varphi(a, \theta)$ on the restricted domain r = a. Hence we need only consider r = a, yielding the integral equation

$$\mu\varphi(a,\theta) = a \int_0^{2\pi} \mathcal{W}(a,a;\phi)\varphi(a,\theta-\phi)d\phi$$
 (5.23)

The solutions of this equation are exponential functions $e^{\gamma\theta}$ where γ satisfies

$$a \int_0^{2\pi} \mathcal{W}(a, a; \phi) e^{-\gamma \phi} d\phi = \mu.$$

By the requirement that φ is 2π -periodic in θ , it follows that $\gamma = in$ where $n \in \mathbb{Z}$. Thus the integral operator with kernel \mathcal{W} has a discrete spectrum given by

$$\mu_n = a \int_0^{2\pi} \mathcal{W}(a, a; \phi) e^{-in\phi} d\phi$$

$$= a \int_0^{2\pi} w \left(\sqrt{a^2 + a^2 - 2a^2 \cos \phi} \right) e^{-in\phi} d\phi$$

$$= 2a \int_0^{\pi} w \left(2a \sin \phi \right) e^{-2in\phi} d\phi$$
(5.24)

(after rescaling ϕ). Note that μ_n is real since

$$\Im m(\mu_n(a)) = -2a \int_0^{\pi} w(2a\sin\phi)\sin(2n\phi)d\phi = 0,$$

i.e., the integrand is odd-symmetric about $\pi/2$. Hence,

$$\mu_n(a) = \Re e(\mu_n(a)) = 2a \int_0^{\pi} w(2a\sin\phi)\cos(2n\phi)d\phi$$

with the integrand even-symmetric about $\frac{\pi}{2}$.

The μ_n can be thought of as *spatial* eigenvalues, i.e., belonging to the point spectrum of the linear operator arising from spatial component of the spectral problem (5.21). Each eigenvalue pair λ_n of the linearized operator has an associated spatial Fourier mode φ_n with corresponding spatial eigenvalue μ_n . The dependence of λ_n on μ_n is given by

$$\lambda_n^{\pm} = \frac{1}{2} \left(-\Lambda_n \pm \sqrt{\Lambda_n^2 - 4\epsilon(1+\beta)(1-\Gamma_n)} \right), \tag{5.25}$$

where

$$\Lambda_n = 1 + \epsilon - \Gamma_n(1+\beta), \qquad \Gamma_n = \frac{\mu_n(a)}{(1+\beta)|U'(a)|}.$$
 (5.26)

Stability of the two-dimensional pulse requires that

$$\Lambda_n > 0$$
, $\Gamma_n < 1$ for all $n \ge 0$.

This reduces to the stability conditions

$$\epsilon > \beta$$
: $\Gamma_n < 1$ for all $n \ge 0$
 $\epsilon < \beta$: $\Gamma_n < \frac{1+\epsilon}{1+\beta}$ for all $n \ge 0$. (5.27)

5.2.2 General, Positive Synaptic Weight Distribution

Herein we collect results that apply to all positive, monotonically decreasing weight functions. First, we rewrite the stability conditions in terms of the gradient of the input D(a) = |I'(a)|. From equations (5.2), (5.8) and (5.9) we have

$$U'(a) = \frac{1}{1+\beta} \bigg(-M_r(a) + I'(a) \bigg),$$

where

$$M_r(a) \equiv -\frac{\partial}{\partial r} M(a,r) \bigg|_{r=a} = 2\pi a \int_0^\infty \rho \check{w}(\rho) J_1(a\rho) J_1(a\rho) d\rho. \tag{5.28}$$

We have already established in section 5.1.2 that $M_r(a) > 0$ for a positive, monotonically decreasing weight function. Hence,

$$|U'(a)| = \left(\frac{1}{1+\beta}\right) - M_r(a) + I'(a)$$

$$= \left(\frac{1}{1+\beta}\right) \left(M_r(a) + D(a)\right). \tag{5.29}$$

The stability conditions (5.27) thus become

$$\epsilon > \beta$$
: $D(a) > \mu_n(a) - M_r(a)$ for all $n \ge 0$,
 $\epsilon < \beta$: $D(a) > \left(\frac{1+\beta}{1+\epsilon}\right)\mu_n(a) - M_r(a)$ for all $n \ge 0$.

Then, since w(r) is a positive function of r, it follows that

$$\mu_n(a) \le 2a \int_0^{\pi} w(2a\sin\phi) |\cos(2n\phi)| d\phi \le 2a \int_0^{\pi} w(2a\sin\phi) d\phi = \mu_0(a),$$

implying that stability is only determined by n=0. Finally, we obtain the reduced stability conditions

$$\epsilon > \beta$$
: $D(a) > \mu_0(a) - M_r(a) \equiv D_{SN}(a)$ (5.30)

$$\epsilon < \beta: \qquad D(a) > \left(\frac{1+\beta}{1+\epsilon}\right)\mu_0(a) - M_r(a) \equiv D_c(a).$$
(5.31)

We now relate stability of the stationary pulse to the gradient D on different branches of the existence curves shown in Figure 5.2 for w(r) given by the exponential distribution (5.9). In this case the integral expressions for $\mu_0(a)$, $M_r(a)$ and $\mathbf{M}(a)$ can be evaluated explicitly in terms of finite sums of modified Bessel and Struve functions. However, the following results essentially are valid on all corresponding existence curves associated with any positive, monotonically decreasing weight function.

Stability for $\epsilon > \beta$. Equation (5.10) implies that $G'(a) = \mathbf{M}'(a) + I'(a)$. Since $\mathbf{M}(a) = M(a, a)$, it follows from equations (5.3), (5.24) and (5.28) that

$$\mathbf{M}'(a) = \partial_1 M(a, a) + \partial_2 M(a, a)$$

= $\mu_0(a) - M_r(a)$ (5.32)

and hence

$$G'(a) = \mu_0(a) - M_r(a) - D(a). \tag{5.33}$$

Thus stability condition (5.30) is satisfied when G'(a) < 0 and not satisfied when G'(a) > 0. Saddle-node bifurcations occur when G'(a) = 0, that is, when D(a) passes through $D_{SN}(a) = \mu_0(a) - M_r(a)$. This establishes the stability of the middle branch in case (i) and the upper branch of cases (ii) and (iii) shown in the left-hand column of Figure 5.2.

Hopf curves for $\epsilon < \beta$. A Hopf bifurcation occurs when $\Lambda_0 = 0$ and $\Gamma_0 < 1$, or equivalently, when $D(a) = D_c(a)$. Since $\mu_0(a) > 0$ it follows from equations (5.30) and (5.31) that $D_c(a) > D_{\text{SN}}(a)$, and hence Hopf bifurcations only occur on the branches that are stable when $\epsilon > \beta$. As in the one-dimensional case, the Hopf and saddle-node points coincide when $\epsilon = \beta$ and so we expect, as ϵ decreases from β , the Hopf bifurcation point(s) to traverse these previously stable branches from the saddle-node point(s). Again, in order to show this more explicitly, we find a relationship for D(a) that is independent of the input amplitude \mathcal{I} . Using equation (5.10), the input gradient D can be related as

$$D(a) = |I'(a)|$$

$$= \frac{a}{\sigma^2} I(a)$$

$$= \frac{a}{\sigma^2} (\kappa (1+\beta) - \mathbf{M}(a)).$$
(5.34)

For each of the cases discussed in section 4.1.1, we examine graphically the crossings of the curves D(a), $D_c(a)$: stability corresponds to $D(a) > D_c(a)$ with Hopf bifurcation points at $D(a) = D_c(a)$. The results are displayed in Figure 5.5, with the explicit expressions for D(a), $D_c(a)$, $\mu_0(a)$, $M_r(a)$ collected in section 5.2.3.

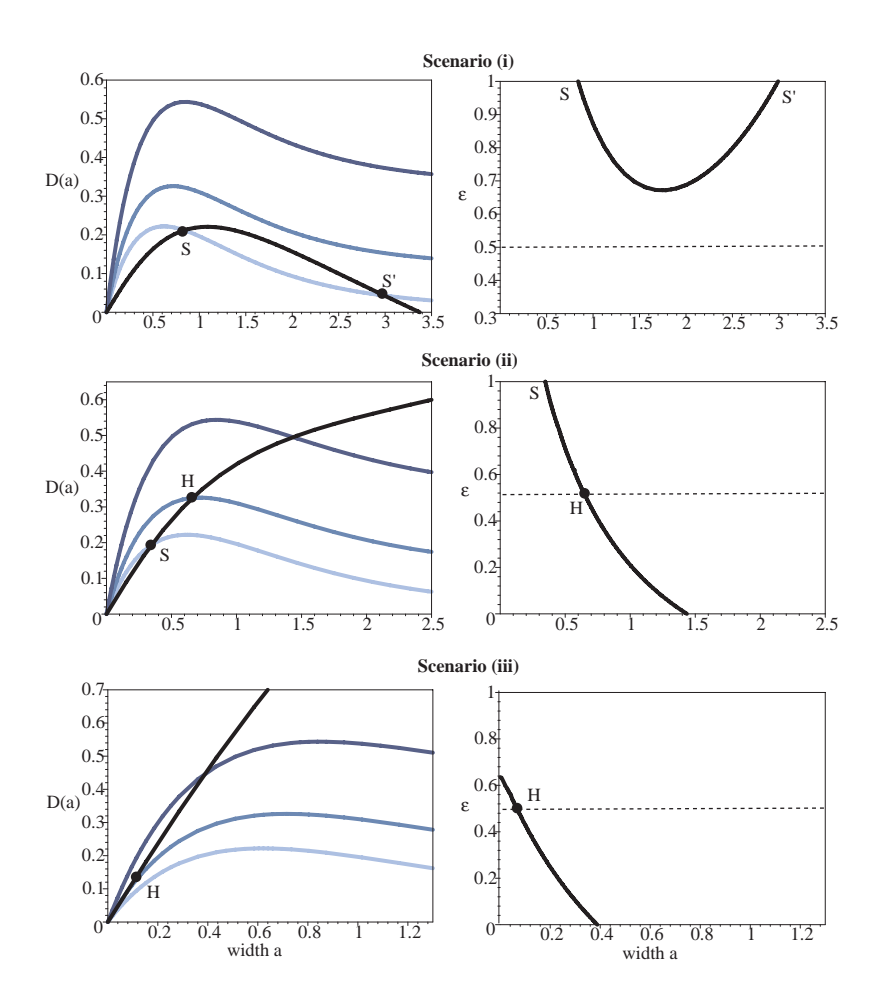


Figure 5.5. LEFT COLUMN: Gradient curves for the bifurcation scenarios shown in Figure 5.2: (i) $\kappa_c < \hat{\kappa} < \frac{1}{2}$, (ii) $\frac{1}{2} < \hat{\kappa} < \kappa_0$ and (iii) $\kappa_0 < \hat{\kappa}$. The thick solid curve shows the input gradient D(a) as a function of pulse width a. The increasingly lighter curves show the critical gradient $D_c(a)$ as function of a for $\epsilon = 0.0, 0.5, 1.0$ and $\beta = 1$. For a given value of $\epsilon < \beta$, a stationary pulse of width a is stable provided that $D(a) > D_c(a)$. A pulse loses stability via a Hopf bifurcation at the intersection points $D(a) = D_c(a)$. The Hopf bifurcation point for $\epsilon = 0.5$ are indicated by H; in the first scenario there are no Hopf points at this particular value of ϵ . In the limit $\epsilon \to \beta$, we have $H \to S$. RIGHT COLUMN: Corresponding Hopf stability curves in the (a, ϵ) -plane.

5.2.3 Exponential Weight Distribution

In the case of the exponential weight distribution the above theory applies. To construct the stability curves we explicitly calculate the functions μ_0 , M_r , D_c , and D. In addition we provide a general expression for $\mu_n(a)$.

$$\mu_0(a) = \frac{a}{\pi} \int_0^{\pi} \exp(-2a\sin\phi)d\phi$$

$$= \frac{2a}{\pi} \int_0^{\frac{\pi}{2}} \exp(-2a\cos\phi)d\phi$$

$$= a\left(\frac{2}{\pi} \int_0^{\frac{\pi}{2}} \cosh(-2a\cos\phi)d\phi\right) - a\left(\frac{2}{\pi} \int_0^{\frac{\pi}{2}} \sinh(-2a\cos\phi)d\phi\right)$$

$$= a\left(I_0\left(2a\right) - \mathbf{L}_0(2a)\right), \tag{5.35}$$

$$\mu_n(a) = \frac{a}{\pi} \int_0^{\pi} \exp(-2a\sin\phi) e^{-i2n\phi} d\phi$$

$$= \frac{a}{\pi} \int_0^{\pi} \exp\left(-i(2n\phi - 2ai\sin\phi)\right) d\phi$$

$$= a\left(\mathbf{J}_{2n}(2ai) - i\mathbf{E}_{2n}(2ai)\right)$$

$$= a\left((-1)^n I_{2n}(2a) - i\mathbf{E}_{2n}(2ai)\right), \tag{5.36}$$

where \mathbf{J}_{ν} , \mathbf{E}_{ν} are the Anger and Weber functions of order ν , respectively.

$$M_r(a) = a \int_0^\infty \frac{\rho}{(\rho^2 + 1)^{\frac{3}{2}}} J_1(a\rho) J_1(a\rho)$$

= $a \Big(\mathbf{L}_0(2a) - I_0(2a) \Big) - \Big(\mathbf{L}_1(2a) - I_1(2a) \Big),$ (5.37)

where

$$I_1(2a) = \frac{4a}{\pi} \int_0^{\pi/2} \cosh(2a\cos\theta) \sin^2\theta d\theta$$
$$\mathbf{L}_1(2a) = \frac{4a}{\pi} \int_0^{\pi/2} \sinh(2a\cos\theta) \sin^2\theta d\theta.$$

Note, there is no simple reduction for \mathbf{E}_{ν} in the case of integral order other than 0, however, $i\mathbf{E}_{2n}(iz)$ is real for $z \in \mathbb{R}$.

Equation (5.31) then implies that

$$D_{c}(a) = \frac{\beta + \epsilon + 2}{1 + \epsilon} a \Big(I_{0}(2a) - \mathbf{L}_{0}(2a) \Big) - \Big(I_{1}(2a) - \mathbf{L}_{1}(2a) \Big).$$
 (5.38)

As in one dimension, sufficiently wide pulse solutions are always stable, which is established by studying the asymptotic behavior of D(a) and $D_c(a)$, for large pulse width $a \to \infty$. Using the asymptotic expansions for large a,

$$I_0(2a) - \mathbf{L}_0(2a) \sim \frac{1}{\pi} \left(\frac{1}{a} + \frac{1}{4a^2} \right)$$

 $I_1(2a) - \mathbf{L}_1(2a) \sim \frac{2}{\pi} \left(1 - \frac{1}{4a^2} \right),$ (5.39)

we deduce that

$$D_c(a) \sim \frac{1}{\pi} \left(\frac{\beta - \epsilon}{1 + \epsilon} \right) + \left(\frac{1}{4} \left(\frac{\beta - \epsilon}{1 + \epsilon} \right) + 1 \right) \frac{1}{\pi a^2}.$$
 (5.40)

Similarly, from equation (5.12) we have

$$\mathbf{M}(a) = a \int_0^\infty \frac{1}{(\rho^2 + 1)^{\frac{3}{2}}} J_0(a\rho) J_1(a\rho) d\rho$$

$$= \left(\frac{1}{2} + a I_1(2a) - \frac{1}{2} I_0(2a)\right) - \left(\frac{2a}{\pi} + a \mathbf{L}_1(2a) - \frac{1}{2} \mathbf{L}_0(2a)\right). \quad (5.41)$$

Equation (5.34) and the asymptotic expansions (5.39) then imply that

$$D(a) \sim \frac{a}{\sigma^2} \left((1+\beta)\kappa - \frac{1}{2} \right) + \frac{1}{\pi\sigma^2} - \frac{1}{8\pi a^2}.$$
 (5.42)

Finally, combining equations (5.40) and (5.42),

$$D(a) - D_c(a) \sim \frac{a}{\sigma^2} \left((1+\beta)\kappa - \frac{1}{2} \right) + \frac{1}{\pi\sigma^2} - \left(\frac{\beta - \epsilon}{1+\epsilon} \right) + \mathcal{O}(a^{-2}). \tag{5.43}$$

From this we conclude that for all $\sigma > 0$, a stationary pulse solution (if it exists) is stable in the limit $a \to \infty$, provided that $\hat{\kappa} > 1/2$.

5.2.4 Mexican Hat Weight Distribution

Interestingly, in the case of the Mexican hat function (5.15), the spatial eigenvalues μ_n are no longer necessarily stratified. As a consequence, a Fourier mode other than the radially symmetric mode n=0 incurs instability through a Hopf bifurcation. The resulting dynamical instability breaks the underlying radial symmetry of the stationary pulse, leading to the formation of a nonradially symmetric breather, demonstrating that one must consider stability with respect to general perturbations rather than only radial perturbations, as in [101]. The number of breathing lobes is consistent with the order of the dominant unstable Fourier mode associated with perturbations of the stationary pulse boundary. Furthermore, we establish that breathers persist under the inclusion of inhibitory connectivity, reflecting the connectivity of the intact cortex.

The choice of the modified Bessel weight w_K allows $M_r(a)$ and $\mu_n(a)$, for all n, to be expressed as finite sums of modified Bessel functions. We calculate

$$\frac{a}{\pi} \int_{0}^{\pi} K_{0}(2\alpha \sin \phi) \cos(2m\phi) d\phi = aI_{m}(\alpha) K_{m}(\alpha).$$

to determine

$$\mu_n(a) = \frac{4}{3} \left(\frac{a_e}{\sigma_e^2} \wp(a, \sigma_e) - \frac{a_i}{\sigma_i^2} \wp(a, \sigma_i) \right)$$

where

$$\wp(a,s) = a \left[I_m \left(\frac{a}{s} \right) K_m \left(\frac{a}{s} \right) - I_m \left(\frac{2a}{s} \right) K_m \left(\frac{2a}{s} \right) \right].$$

Then differentiating (5.17) with respect to r and evaluating at a yields

$$M_r(a) = a_e M_r^{\circ} \left(a, \frac{1}{\sigma_e} \right) - a_i M_r^{\circ} \left(a, \frac{1}{\sigma_i} \right)$$
 (5.44)

where

$$M_r^{\circ}(a,s) = \frac{4}{3}s^2a \left[I_1(sa) K_1(sa) - I_1(2sa) K_1(2sa) \right]$$
 (5.45)

Furthermore, for most parameter values (5.29) continues to hold, however, it is possible that $M_r(a) < 0$, in which case we must handle the absolute value |U'(a)| more carefully. In the case that it is positive we have the stability conditions

$$\epsilon > \beta$$
: $D(a) > \mu_n(a) - M_r(a)$ for all $n \ge 0$, (5.46)

$$\epsilon < \beta: \qquad D(a) > \left(\frac{1+\beta}{1+\epsilon}\right)\mu_n(a) - M_r(a) \equiv D_c^n \qquad \text{for all } n \ge 0.$$
 (5.47)

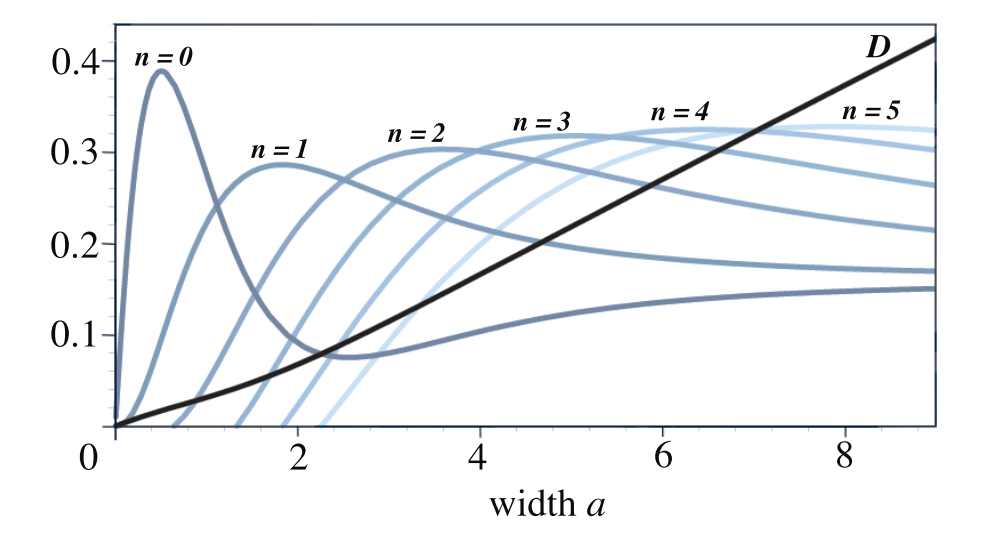


Figure 5.6. Plot of the the functions D(a) (black curve) and $D_c^n(a)$ (blue curves) for different values of n with $\sigma=5.2$; see Figure 5.4 for other parameters. The stationary pulse is stable if $D(a)>D_c^n(a)$ for all n, with a Hopf bifurcation occurring at the first value of a for which this is no longer true. Given input strength \mathcal{I} and corresponding width a, the largest $D_c^n(a)$ determines the mode that dominates the instability. For example a value of $\mathcal{I}=0.53$ corresponds to a=2, indicating that mode n=1 should dominate.

The pulse width a, determined by \mathcal{I} , is a bifurcation parameter of the system, with a Hopf bifurcation occurring at a transverse intersection point of the graphs of D(a) and $D_c^n(a)$ where $D(a) > D_c^n(a)$ fails to hold for all n; see Figure 5.6. The spatial extent of the current input σ controls the steepness of D(a) (see (5.47)), thereby determining which mode destabilizes in the Hopf bifurcation. Importantly, the relative values of $D_c^n(a)$ preserve the ordering of linear dominance of each mode n, indicating which mode should dominate the growth. Thus, by varying the input parameters σ , \mathcal{I} , one can control the destabilizing mode and the dominant mode, respectively, and consequently control the lobed structure of the emergent periodic solution. This analysis establishes that a Mexican hat network can undergo a Hopf bifurcation corresponding to excitation of a nonzero Fourier mode (n > 0). As we confirm numerically below, this leads to the formation of nonradially symmetric breathers.

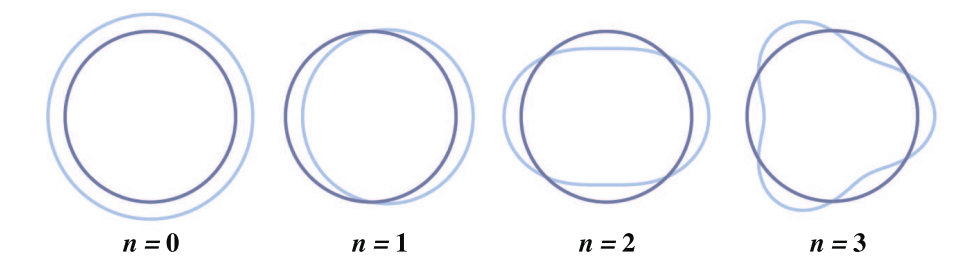


Figure 5.7. Small perturbations decomposed in terms of Fourier modes (light curves) associated with general perturbations of the threshold boundary of a stationary pulse (dark curves).

The basic structure of the emergent breathers can be predicted by noting that a small perturbation φ of the stationary pulse U results in a small perturbation $\boldsymbol{\delta} = \left(\delta_r(\theta), \theta\right)$ of the threshold boundary $\boldsymbol{a} = (a, \theta)$. The corresponding threshold condition is

$$\kappa = u(\boldsymbol{a} + \boldsymbol{\delta}) = U(\boldsymbol{a} + \delta_r(\boldsymbol{\theta})) + \varphi(\boldsymbol{a} + \boldsymbol{\delta}),$$

= $U(\boldsymbol{a}) + U'(\boldsymbol{a})\delta_r(\boldsymbol{\theta}) + \varphi(\boldsymbol{a}, \boldsymbol{\theta}) + \mathcal{O}(|\boldsymbol{\delta}|^2).$

Using that $U(a) = \kappa$, we find

$$\delta_r(\theta) = \frac{\varphi(a,\theta)}{|U'(a)|} + \mathcal{O}(|\boldsymbol{\delta}|^2).$$

Since φ may be decomposed into Fourier modes in the linear regime, we illustrate in Figure 5.7 the perturbative effect each mode imparts upon the threshold boundary. Furthermore, if one mode should dominate the linear growth of an instability, we expect the boundary of the breather to develop similar structure. We note that nonradially symmetric instabilities have also been found in a study of homogenous networks, where concentric ring solutions can destabilize into multiple bump solutions, the number of which corresponds to the Fourier mode dominating the instability [62]. However, in this case the emergent time–periodic solutions manifest such structure in several forms of spatially localized, periodic solutions, which are described in the following section.

5.3 Numerical Simulations

In this section we summarize the results of numerical simulations. When \mathcal{I} corresponds to a stable stationary pulse, a perturbation of the exact solution leads to a short transient before equilibrium. In the excitatory network, this transient generates a circular wave, when such a wave exists. We now discuss the behavior of each network beyond the Hopf bifurcation point.

5.3.1 Exponential Weight Distribution

Analogous to the one–dimensional case, we find numerically that the upper branch in scenarios (ii) and (iii) can undergo a supercritical Hopf bifurcation leading to the formation of a two–dimensional breather. An example is shown in Figure 5.8(a), obtained using a Runge-Kutta scheme on a 300x300 grid with a time step of 0.02. Moreover, the breather can undergo a secondary instability, resulting in the periodic emission of circular target waves; see Figure 5.8(b).

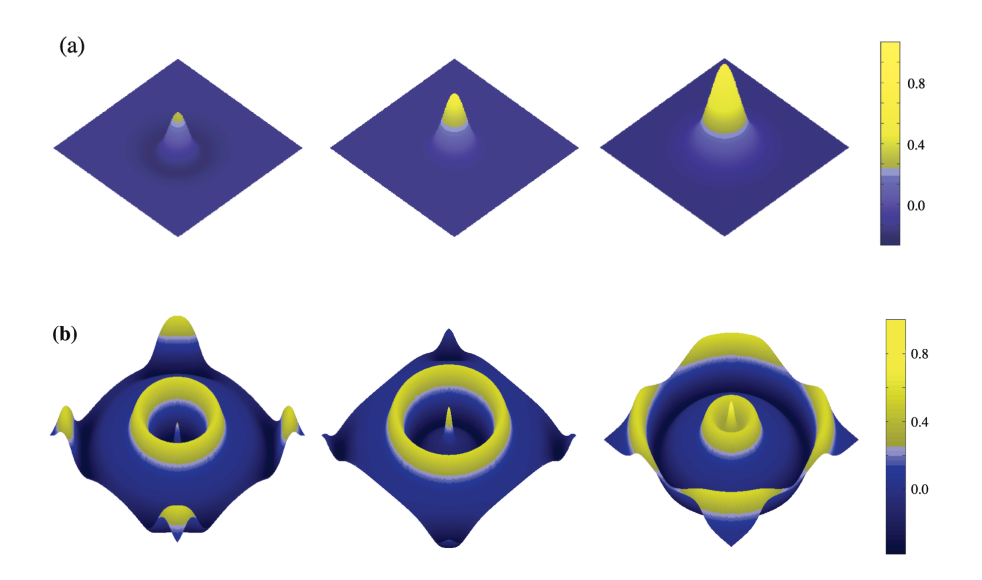


Figure 5.8. Two-dimensional breathers for the excitatory (exponential) weight distribution. (a) Two-dimensional breather sequence with $\beta=4$, $\kappa=0.25$, $\epsilon=0.1$. (b) Two-dimensional pulse-emitter with $\beta=4$, $\kappa=0.2$, $\epsilon=0.1$, $\mathcal{I}=0.2$.

5.3.2 Mexican Hat Weight Distribution

Numerical simulations were performed using a Runge-Kutta (RK4) scheme, with a fast-Fourier transform to handle the integral on a rectangular grid (400x400–2000x2000) and quadrature on an irregular polar grid. The polar grid consists of concentric rings, with each ring increasing the grid point count by one more than the neighboring inner ring. The ring spacing is chosen so that each area element contributes equal weight to the integral. Selecting \mathcal{I} so that the system is positioned beyond the bifurcation point with mode n dominating the instability, the system is evolved from a small random perturbation of the corresponding exact (unstable) stationary pulse solution.

Our simulations reveal many types of spatially localized, periodic solutions that are generated by the Mexican hat network. In all cases the periodic solution exhibits a lobed structure, the number of which corresponds to the dominant Fourier mode. Breathers take the general form of emerging and retracting lobes, which often rotate about the input in mirror symmetry, as shown in Figure 5.9. On the rectangular grid it is possible to generate breathers for n=1,2,4,8 which exhibit strictly radially expanding/contracting lobes, that do not rotate about the input, as shown in Figure 5.11-a. It is likely that such breathers are observed because they are commensurate with the grid. However, the irregular polar grid does in fact produce expanding/contracting type breathers for n=1,2. It may be possible with exceedingly large grid point counts, or with a regular polar grid, to generate such breathers. Though, it is more reasonable to expect a population of real neurons to exhibit behavior more along the lines of Figure 5.9.

Interestingly, when the initial transient is sufficiently irregular, or if a sufficiently large initial perturbation with n-fold symmetry is applied, spatially localized rotating solutions (or rotors) emerge, see Figure 5.11-b. It seems that there is some sort of separatrix dividing the flow either to an attracting breather or rotor. In the case of the rectangular grid, it is clear that certain modes which are commensurate with the grid are favored in terms of growth of the instability associated with small random perturbations of the unstable stationary pulse. This can lead initially to an irregularly shaped lobed structure of activity, possibly due to a competition between the dominant mode and a grid-favored mode, that ultimately transitions to a breather or rotor whose lobed structure is consistent with the dominant mode. Various rotors are shown in Figure 5.10.

For very small threshold values $\kappa \approx 0.01$ it is also possible to generate wave–emitting solutions which similarly break radial symmetry; see Figure 5.12. The small threshold restriction is due to the long-range inhibition of the Mexican hat network is dependent upon its amplitude and strength.

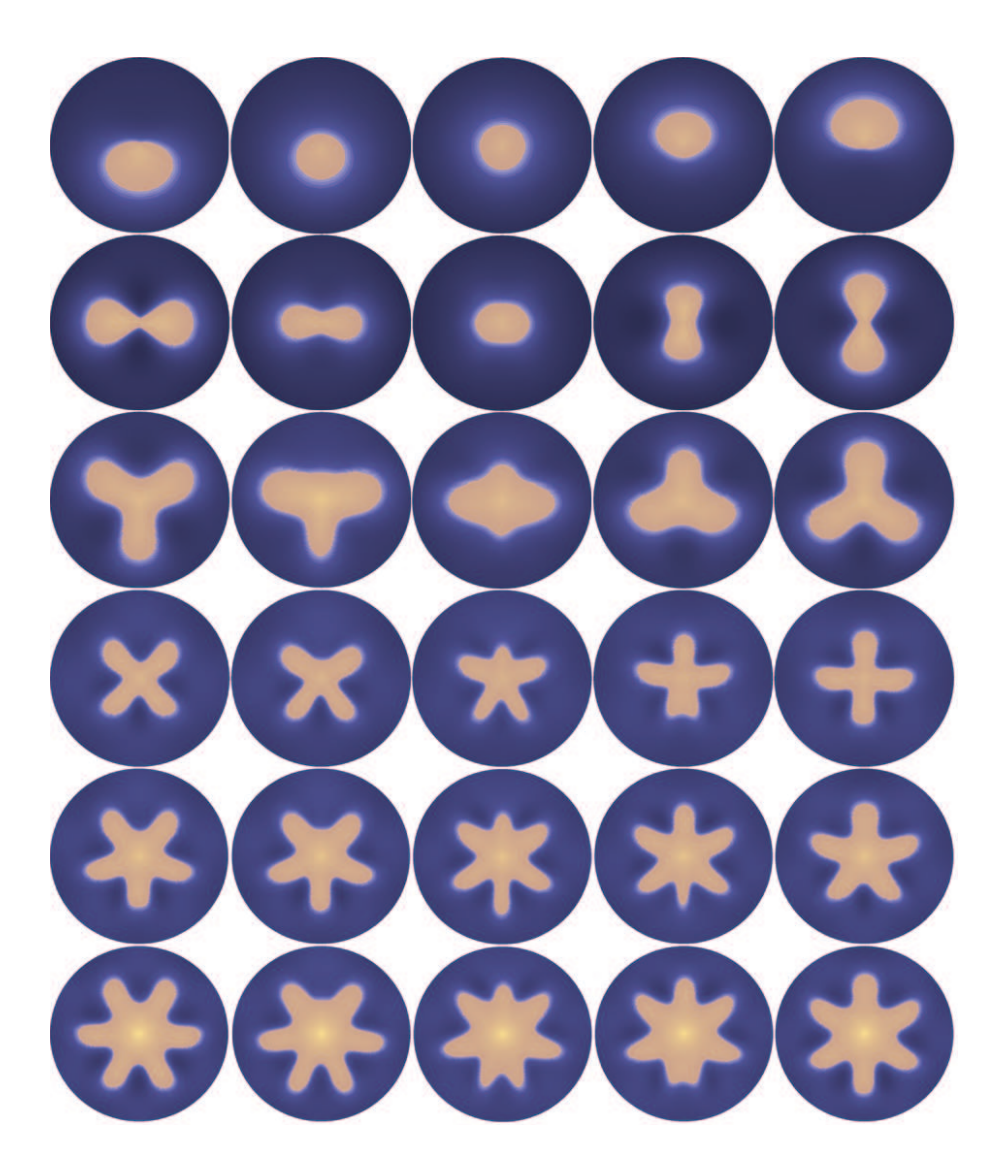


Figure 5.9. Breathers for the Mexican hat weight function and polar grid. Light colors denote suprathreshold values, with the number of lobes corresponding to the dominating unstable Fourier mode.

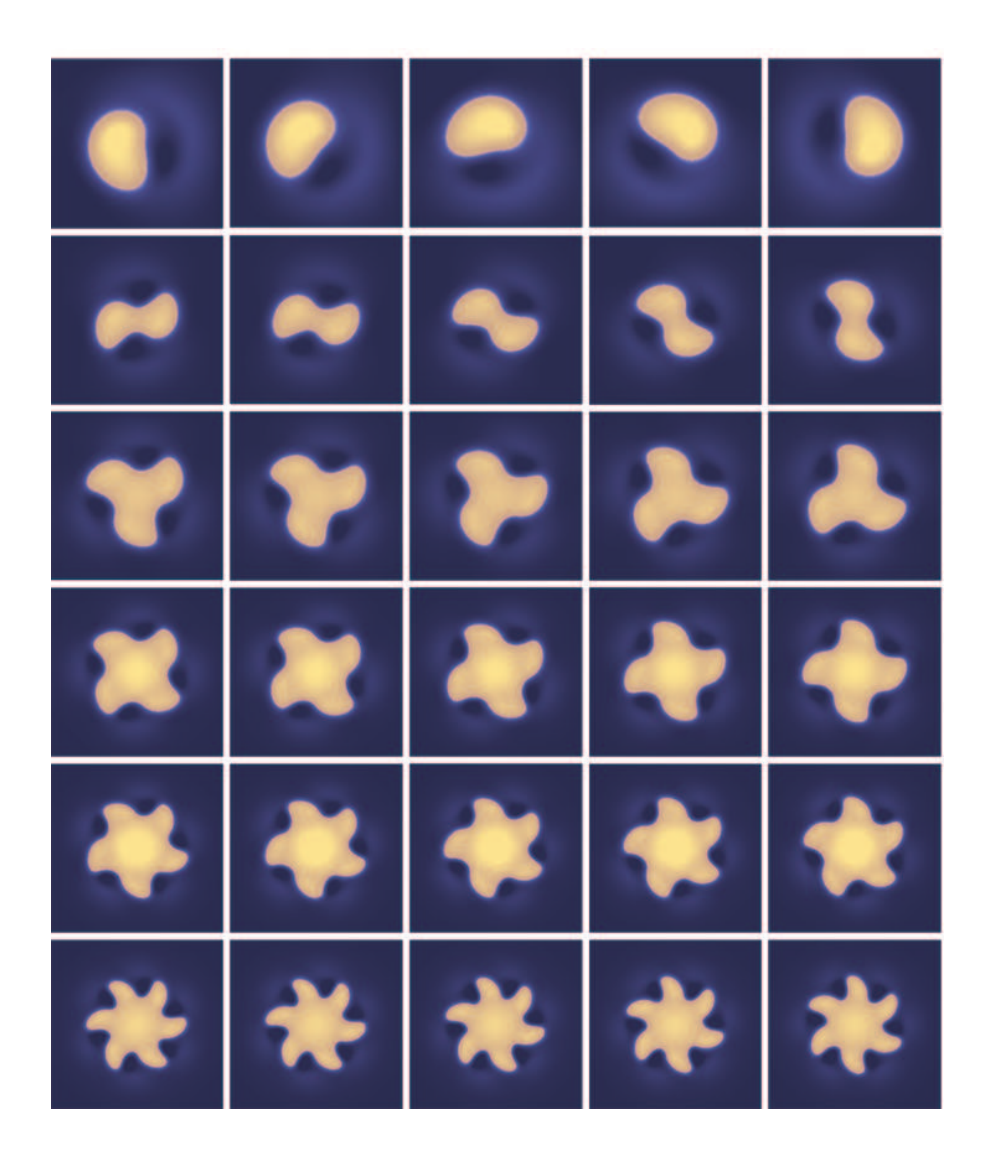


Figure 5.10. Rotors for the Mexican hat weight function and rectangular grid. In each case the number of lobes corresponds to the dominant unstable Fourier mode.

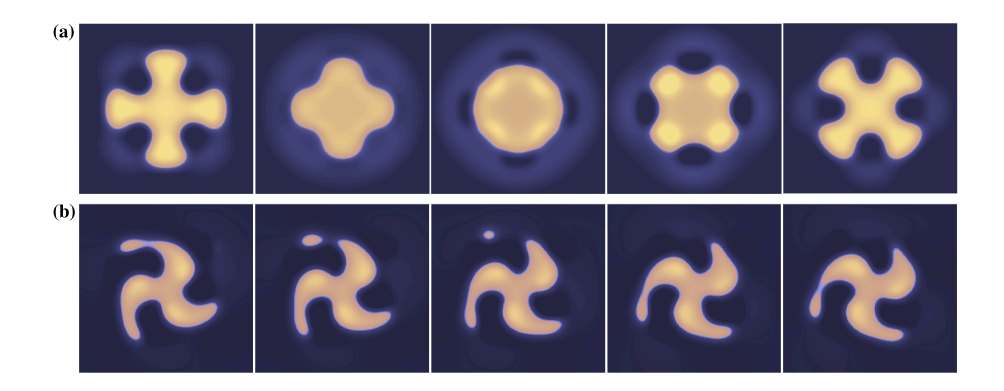


Figure 5.11. (a) Strictly expanding/contracting four-fold breather on a rectangular grid. (b) Far beyond the Hopf bifurcation point, a three-fold rotor emits a transient pulse of activity.

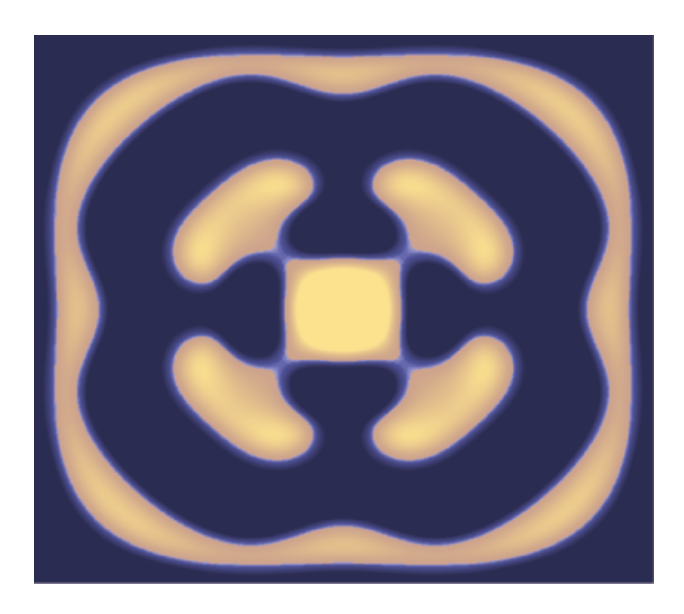


Figure 5.12. Wave emission exhibiting four-fold symmetry.

5.4 Discussion

In this chapter we have extended the analysis of stationary pulses and breathers to two-dimensional networks with radially symmetric inputs. In the case of an excitatory weight function, the results are similar to the one-dimensional case, (i) radially symmetric stationary pulses are stabilized by sufficiently large inputs, (ii) for $\epsilon < \beta$ the stationary pulse undergoes a Hopf bifurcation prior to the saddle-node bifurcation, giving rise to radially-symmetric breathing pulses, and (iii) a further reduction leads to a secondary instability in which the breather periodically emits circular waves into the surrounding medium. The radial symmetry is due to the fact that the lowest order spatial mode of the linearization always dominates the instability. Interestingly, we find that this is not necessarily the case for the Mexican hat weight function. By varying the spatial extent of the input, the Hopf bifurcation may correspond to a higher mode. Beyond the bifurcation point, different modes dominate the instability and determine the shape of the breather. Furthermore, the network also supports coexistent, spatially-localized rotating waves.

Interestingly, it is found that the attracting dynamics depend, in part, upon the grid used as an approximate representation of the continuous domain. The relevant question arises, what are the appropriate types of solution generated by the network, when the network is an infinite-dimensional neural continuum or a finite-dimensional rectangular or polar grid? While infinite-dimensional in nature, dissipative systems often possess a stable, finite-dimensional attractor, lending the support for the confidence in *finite-dimensional* numerical schemes to represent the behavior of the continuous system. It would be interesting to understand how the dynamics of the *n*-lobed breather are generated by the rectangular and polar grids, i.e., to determine what are the conditions which produce strictly expanding/contracting breathers and breathers which exhibit emerging/retracting lobes that rotate about the input. Moreover, does there always a coexisting rotor of the same order which contains its own basin of attraction, establishing two forms of attracting, spatially localized periodic solutions, both of which may be generated in the Hopf bifurcation.

One of the predictions of our analysis is that breathers may be observed in tangential slices (an effective two-dimensional medium) when a persistent localized input is applied. In the case of disinhibited cortical slices, a radially symmetric input should produce roughly radially symmetric breathers of activity, whereas, if inhibitory connections are maintained, nonradially symmetric breathers should be observed. There are a number of experimental challenges to overcome, however, including the destruction of neurons due to persistent current input and the control of the structure of the input. The use of electric fields by Richardson et al. [?] may be one feasible approach. Experimental verification of breathers may reveal that some form of slow, negative feedback

is playing a strong role in the dynamics of neural populations, lending support for the use of rate-based neural network models.

Since breathers continue to exist in the presence of inhibition, our work also establishes that persistent inputs may be a source of oscillations in the intact cortex, which could have important implications for the processing of sensory stimuli. From a more general dynamical systems perspective, we have identified a mechanism for the generation of complex spatially localized oscillations in two–dimensional excitable media with nonlocal Mexican hat interactions and input inhomogeneities. This then raises the interesting question as to whether or not analogous dynamical instabilities can occur in diffusively coupled excitable media. Indeed, it has recently been shown that Mexican hat networks exhibit a range of dynamical phenomena also found in three–component reaction-diffusion systems [19].

CHAPTER 6

STIMULUS-LOCKED TRAVELING WAVES AND BREATHERS IN AN EXCITATORY NETWORK

In this chapter we extend the Evans function approach of Zhang [116] and the results on stationary inhomogeneous inputs (Chapter 4), by analyzing the existence and stability of traveling waves locked to a moving input of constant speed v. Consider the Pinto-Ermentrout model subject to a moving input

$$\tau \frac{\partial u(x,t)}{\partial t} = -u(x,t) - \beta \varrho(x,t) + \int_{\mathbb{R}^2} w(x-x') H(u(x',t)-\kappa) dx' + I(x-vt)$$

$$\frac{1}{\epsilon} \frac{\partial \varrho(x,t)}{\partial t} = -\varrho(x,t) + u(x,t). \tag{6.1}$$

We assume throughout that w(x) is a positive, even function, monotonically decreasing on $[0,\infty)$, that satisfies the normalization condition $\int_{\mathbb{R}^2} w(x)dx < \infty$ ∞ . The input is written as $I(x-vt)=I_0\,\chi(x-vt)$ with χ a fixed spatial profile that is either a bounded, monotonically decreasing function in the case of fronts, or a unimodal Gaussian-like function in the case of pulses. The input amplitude I_0 and velocity v are treated as bifurcation parameters. Working in the moving frame of the input, we derive threshold-crossing conditions for the existence of a stimulus-locked wave and use these conditions to construct existence tongues in (v, I_0) -parameter space whose tips at $I_0 = 0$ correspond to the intrinsic waves of the homogeneous network, assuming that the latter exist. In the particular case of an exponential weight distribution, we show that there are two tongues in the positive v domain, corresponding to an unstable/stable pair of right-moving intrinsic waves. We determine the stability of the waves within these existence tongues by first constructing the Evans function for a general weight distribution w satisfying the properties listed below equation (6.1) and then numerically calculating the zeros of the Evans function for the exponential weight distribution. We show that as the input is reduced, a stimulus-locked

wave within the tongue of the unstable intrinsic wave can undergo a Hopf bifurcation leading to the emergence of a traveling oscillatory wave. The latter takes the form of a breather or a pulse-emitter in the moving frame of the stimulus. In the limit $v \to 0$ our results reduce to those previously obtained for stationary inputs; see Chapter 4.

The structure of the chapter is as follows. In order to illustrate the general approach, we begin by considering the simpler case of zero negative feedback $(\beta = 0)$, for which equation (6.1) reduces to a scalar equation in u (section 6.1). The corresponding existence tongues for stimulus–locked fronts and their stability can be completely determined analytically. We next consider the existence of stimulus-locked pulses in the full vector system (6.1), numerically solving a set of nonlinear functional equations in order to construct the associated tongues (section 6.2). We then develop the linear stability analysis of stimulus-locked pulses in order to determine the stability of solutions within the tongues (section 6.3). Finally, we present numerical simulations illustrating the formation of traveling breathers and pulse-emitters. Although we focus on traveling pulses rather than fronts in the case of the full system (6.1), it is straightforward to carry over our results to the case of stimulus-locked fronts, as mentioned in section 3.4.4. Throughout we work with dimensionless units. The fundamental time scale is taken to be the membrane time constant τ , which is assumed to be of the order 10 msec. The fundamental length scale is taken to be the range d of synaptic coupling, which can vary between a few hundred micrometers to a few millimeters.

6.1 Stimulus-Locked Traveling Fronts in a Scalar Equation

We carry out a complete analysis of the existence and stability of stimulus-locked fronts in a scalar version of (6.1). As an illustrative example, we construct tongue diagrams for an exponential weight, showing how the existence regions of fronts in the (v, I_0) -plane deform as the threshold κ is varied. We also establish that the fronts within the existence tongues are always stable.

6.1.1 Existence of Stimulus-Locked Fronts

Consider the scalar network

$$\frac{\partial u(x,t)}{\partial t} = -u(x,t) + \int_{-\infty}^{\infty} w(x-y)H(u(y,t) - \kappa)dy + I(x-vt)$$
 (6.2)

where the input is taken to be a positive, bounded, monotonic function. This equations is not translationally invariant due to the presence of the input.

However, we may seek traveling front solutions of the form $u(x,t) = U(\xi)$ where $\xi = x - vt$ and

$$U(\xi) > \kappa$$
, $\xi < \xi_0$; $U(\xi_0) = \kappa$; $U(\xi) < \kappa$, $\xi > \xi_0$,

for some $\xi_0 \in \mathbb{R}$. The wave of excitation is assumed to travel at the same velocity as the input, though the relative positions of the active region (above threshold), and the input may vary with respect to the velocity and the input strength. Thus, the active region is locked to the input but may precede or succeed the input in position. We take $U \in \mathcal{C}^1(\mathbb{R}, \mathbb{R})$, where $\mathcal{C}^n(\mathbb{R}, \mathbb{R})$ denotes the set of all n-times continously differentiable functions $f: \mathbb{R} \longrightarrow \mathbb{R}$ which are bounded with respect to the sup norm. If $I_0 = 0$ then the system is translationally invariant and ξ_0 becomes a free parameter. In this case we refer to traveling waves as intrinsic or natural waves. The profile of the front is determined according to

$$-v\frac{dU(\xi)}{d\xi} = -U(\xi) + \int_{-\infty}^{\xi_0} w(\xi - \eta)d\eta + I(\xi).$$
 (6.3)

Setting

$$W(\xi) = \int_{-\infty}^{\xi} w(\eta) d\eta,$$

we can integrate equation (6.2) for v > 0 over $[\xi, \infty)$ to obtain

$$U(\xi) = \frac{1}{v} \int_{\xi}^{\infty} e^{(\xi - \eta)/v} N_e(\eta; \xi_0) d\eta,$$

where

$$N_e(\xi; \xi_0) = 1 - W(\xi - \xi_0) + I(\xi).$$

We are assuming that w is normalized such that $\int_{\mathbb{R}} w(\eta) d\eta = 1$. Similarly, for v < 0 we integrate over $(-\infty, \xi]$ to find

$$U(\xi) = -\frac{1}{v} \int_{-\infty}^{\xi} e^{(\xi - \eta)/v} N_e(\eta; \xi_0) d\eta.$$

The threshold condition for the existence of a stimulus-locked front is $\kappa = U(\xi_0)$. As a specific example, we consider a Heaviside input $I(\zeta) = I_0 H(-\zeta)$ and an exponential weight function

$$w(x) = \frac{1}{2d} e^{-|x|/d},$$
 (6.4)

with length scale fixed by setting d=1. The resulting threshold condition is

$$\kappa = \begin{cases}
\frac{1}{2(1+v)} + \begin{cases} 0, & \xi_0 \ge 0, \\ I_0(1-e^{\xi_0/v}), & \xi_0 < 0, \end{cases}, & v > 0; \\
\frac{1+2|v|}{2(1+|v|)} + \begin{cases} I_0e^{\xi_0/v}, & \xi_0 > 0, \\ I_0, & \xi_0 \le 0, \end{cases}, & v < 0.
\end{cases}$$
(6.5)

In the absence of an input $(I_0 = 0)$, the threshold condition reduces to

$$\kappa = \begin{cases} \frac{1}{2(1+v_{\circ})}, & v \ge 0, \\ \frac{1+2|v_{\circ}|}{2(1+|v_{\circ}|)}, & v < 0, \end{cases}$$

where v_{\circ} is the natural speed of the wave. Solving for v_{\circ} in terms of κ , we find that v_{\circ} is a sigmoidal function of κ .

$$v_{\circ}(\kappa) = \begin{cases} \frac{\frac{1}{2} - \kappa}{\kappa}, & 0 < \kappa \le \frac{1}{2}, \\ \frac{\frac{1}{2} - \kappa}{(\kappa - 1)}, & \frac{1}{2} < \kappa < 1. \end{cases}$$

The homogeneous network supports a stationary natural front $(v_o = 0)$ when $\kappa = \frac{1}{2}$, a front moving to the right for $0 < \kappa < \frac{1}{2}$, and front moving to the left for $\frac{1}{2} < \kappa < 1$. Moreover, $v_o \to \infty$ as $\kappa \to 0$ and $v_o \to -\infty$ as $\kappa \to 1$. It does not support a natural front when $\kappa > 1$, as any heteroclinic orbit joining the equilibria $\{0,1\}$ at infinity does not satisfy the threshold behavior used to define a traveling front solution. This recovers a result from [26].

We now analyze equation (6.5) for $I_0 > 0$ in order to determine the regions of the (v, I_0) -parameter subspace for which stimulus-locked waves exist. We first consider the case v > 0. For $\xi_0 \ge 0$ we have the threshold condition

$$\kappa = \frac{1}{2(1+v)}$$

and, hence, there are infinitely many waves parameterized by $\xi_0 \in [0, \infty)$, all of which travel with the natural speed $v = \frac{1-2\kappa}{2\kappa}$ for $0 < \kappa < \frac{1}{2}$. This degeneracy is a consequence of using the Heaviside input and would not occur, if a continuous,

strictly monotonic input were used; however, the analysis is considerably more involved. For $\xi_0 < 0$ we have instead

$$\kappa = \frac{1}{2(1+v)} + I_0(1 - e^{\xi_0/v}).$$

As the right-hand-side is monotonic in ξ_0 , we can solve for ξ_0 as a function of v to obtain

$$\xi_0(v) = v \ln \left[1 - \frac{1}{I_0} \left(\kappa - \frac{1}{2(1+v)} \right) \right].$$

Since $\xi_0 < 0$ and v > 0, we see that solutions exist only if

$$0 < 1 - \frac{1}{I_0} \left(\kappa - \frac{1}{2(1+v)} \right) \le 1$$

or, equivalently,

$$2(\kappa - I_0) < \frac{1}{1+v} \le 2\kappa. \tag{6.6}$$

The right inequality of (6.6) implies that, if $\kappa < \frac{1}{2}$, then $v > v_{\circ}(\kappa)$, where v_{\circ} is the corresponding natural velocity. Similarly, the left inequality implies that, if $I_0 < \kappa$, then $0 < v < v_1(\kappa - I_0)$, with $v_1(s) = \frac{1}{2s} - 1$. Hence, for $0 < \kappa \le \frac{1}{2}$ we obtain the existence regions in the (v, I_0) -plane shown in Figure 6.1(a-b). The left boundary is given by $v = v_{\circ}(\kappa)$ and the right boundary by $v = v_1(\kappa - I_0)$. The two boundaries form a tongue that emerges from the natural speed $v_{\circ}(\kappa)$ at $I_0 = 0$.

Now consider v < 0. For $\xi_0 < 0$ we have the threshold condition

$$\kappa = \frac{1+2|v|}{2(1+|v|)} + I_0$$

which implies

$$|v| = \frac{1 - 2(\kappa - I_0)}{2(\kappa - I_0 - 1)} \equiv v_2(\kappa - I_0).$$

Again we have an infinite family of waves corresponding to a single speed. Since $|v| \ge 0$, such solutions only exist for

$$\kappa - 1 < I_0 < \kappa - \frac{1}{2}.$$

On the other hand, for $\xi_0 \geq 0$ we have the threshold condition

$$\kappa = \frac{1 + 2|v|}{2(1 + |v|)} + I_0 e^{\xi_0/v}.$$

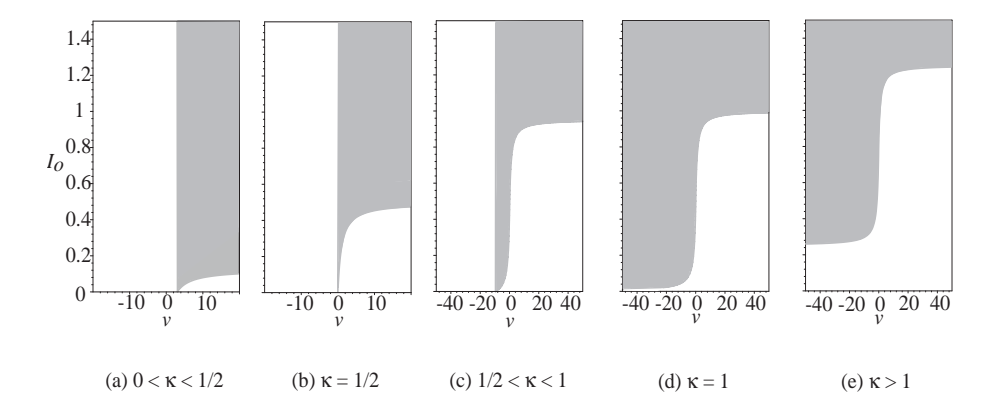


Figure 6.1. Deformation of existence regions (gray) for stimulus-locked traveling fronts as κ varies in the scalar equation.

Monotonicity of the right-hand-side again allows us to solve for $\xi_0(v)$ to find

$$\xi_0(v) = v \ln \left[\frac{1}{I_0} \left(\kappa - \frac{1 + 2|v|}{2(1 + |v|)} \right) \right].$$

and, since v < 0 and $\xi_0 \ge 0$, it follows that waves only exist for v satisfying

$$\kappa - I_0 \le \frac{1 + 2|v|}{2(1 + |v|)} < \kappa. \tag{6.7}$$

The right inequality of (6.7) implies that, if $\frac{1}{2} < \kappa < 1$, then $v_{\circ}(\kappa) < v < 0$. Thus, for $\frac{1}{2} < \kappa < 1$ we obtain the existence region shown in Figure 6.1(c); the left boundary is given by $v = v_0(\kappa)$ and the right boundary by $v = v_2(\kappa - I_0)$ for v < 0 and $v = v_1(\kappa - I_0)$ for v > 0. Again there is a tongue with tip at the natural speed. For $\kappa > 1$ the left boundary disappears, and one only finds stimulus-locked waves when $I_0 > \kappa - 1$, i.e., natural waves no longer exist. The left inequality of (6.7) implies that if $\frac{1}{2} < \kappa - I_0 < 1$ then $v < v_2(\kappa - I_0) < 0$, whereas, if $\kappa - I_0 > 1$ then no solution exists. For all $\kappa > 1$ the region of existence is identical to that for $\kappa = 1$, though it is shifted vertically by $\kappa - 1$, as shown in Figure 6.1(d-e).

6.1.2 Stability of Stimulus-Locked Fronts

Consider the evolution of small smooth perturbations $\bar{\varphi}$ of the stimulus-locked front solution U. Linearizing equation (6.2) about the wave, the perturbations evolve according to

$$\frac{\partial \bar{\varphi}}{\partial t} - v \frac{\partial \bar{\varphi}}{\partial \xi} + \bar{\varphi} = \int_{\mathbb{R}} w(\xi - \eta) H'(U(\eta) - \kappa) \bar{\varphi}(\eta) d\eta. \tag{6.8}$$

Separating variables, $\bar{\varphi}(\xi,t) = \varphi(\xi)e^{\lambda t}$, we find that $\varphi \in \mathcal{C}^1(\mathbb{R},\mathbb{C})$ satisfies the eigenvalue problem

$$(\mathcal{L} + \mathcal{N}_s) \varphi = \lambda \varphi \tag{6.9}$$

where

$$\mathcal{L}\varphi = v\frac{\partial\varphi}{\partial\xi} - \varphi, \qquad \mathcal{N}_s\varphi(\xi) = \frac{w(\xi - \xi_0)}{|U'(\xi_0)|} \varphi(\xi_0). \tag{6.10}$$

We need to characterize the spectrum of the linear operator $\mathcal{L}+\mathcal{N}_s: \mathcal{C}^1(\mathbb{R},\mathbb{C}) \longrightarrow \mathcal{C}^0(\mathbb{R},\mathbb{C})$ in order to determine the linear stability of the traveling pulse. The following definitions concern linear operators $\mathcal{T}: \mathcal{D}(\mathcal{T}) \longrightarrow \mathcal{B}$ where \mathcal{B} is a Banach space and the domain $\mathcal{D}(\mathcal{T})$ of \mathcal{T} is dense in \mathcal{B} [114]. In our case $\mathcal{D}(\mathcal{L}+\mathcal{N}_s)=\mathcal{C}^1(\mathbb{R},\mathbb{C})$ which is dense in $\mathcal{C}^0(\mathbb{R},\mathbb{C})$. λ is in the resolvent set ρ , if $\lambda \in \mathbb{C}$ is such that $\mathcal{T}-\lambda$ has a range dense in \mathcal{B} and a continuous inverse $(\mathcal{T}-\lambda)^{-1}$, otherwise λ is in the spectrum σ . We decompose the spectrum into the following disjoint sets. λ is an element of the point spectrum σ_p , if $\mathcal{T}-\lambda$ is not invertible; λ is an element of the continuous spectrum σ_c , if $\mathcal{T}-\lambda$ has an unbounded inverse with domain dense in \mathcal{B} ; λ is an element of the residual spectrum σ_r , if $\mathcal{T}-\lambda$ has an inverse (bounded or not) whose domain is not dense in \mathcal{B} . We refer to elements of the point spectrum as eigenvalues and the union of the continuous and residual spectra as the essential spectrum.

Regarding the essential spectrum, we mention that \mathcal{N}_s is a compact linear operator. The consequence is that, since \mathcal{N}_s is compact, the operators $\mathcal{L} + \mathcal{N}_s$ and \mathcal{L} have the same essential spectra [54, 53]. To see that the operator is compact, we define \mathcal{N}_s by the composition $\mathcal{T} \circ \mathcal{S}$ where

$$\delta \varphi = \varphi(\xi_0), \qquad (\Im z)(\xi) = \frac{w(\xi - \xi_0)}{|u'(\xi_0)|} z.$$

Since $S: \mathcal{C}^1(\mathbb{R}, \mathbb{C}) \longrightarrow \mathbb{C}$ has a finite dimensional range, it is a compact linear operator. Moreover, since $\mathcal{T}: \mathbb{C} \longrightarrow \mathcal{C}^0(\mathbb{R}, \mathbb{C})$ is a bounded linear operator, it follows that the composition $\mathcal{T} \circ S$ is a compact linear operator.

Resolvent and the point spectrum. We seek to construct a bounded inverse by solving the inhomogeneous equation

$$(\mathcal{L} + \mathcal{N}_s - \lambda)\varphi = -f, \tag{6.11}$$

where $f \in \mathcal{C}^0(\mathbb{R}, \mathbb{C})$, using a variation of parameters approach along the lines of Zhang [116]. We write equation (6.11) as

$$\frac{\partial}{\partial \xi} \left(e^{-\left(\frac{1+\lambda}{v}\right)\xi} \varphi(\xi) \right) = -\frac{1}{v} e^{-\left(\frac{1+\lambda}{v}\right)\xi} \left(\mathcal{N}_s \varphi(\xi) + f(\xi) \right). \tag{6.12}$$

For $\frac{\Re e(\lambda)+1}{v}>0$, integrating equation (6.12) over $[\xi,\infty)$ yields

$$\varphi(\xi) - \Lambda_{+}(\lambda; \xi) \, \varphi(\xi_0) = \mathcal{H}_f(\xi). \tag{6.13}$$

where

$$\Lambda_{+}(\lambda;\xi) = \frac{1}{v|U'(\xi_{0})|} \int_{\xi}^{\infty} w(\eta - \xi_{0}) e^{\left(\frac{1+\lambda}{v}\right)(\xi - \eta)} d\eta,$$

$$\mathcal{H}_{f}(\xi) = \frac{1}{v} \int_{\xi}^{\infty} e^{\left(\frac{1+\lambda}{v}\right)(\xi - \eta)} f(\eta) d\eta.$$

Using the Hölder inequality, it can be shown that both $\Lambda_+(\lambda; \xi)$ and $\mathcal{H}_f(\xi)$ are bounded for all $\xi \in \mathbb{R}$ and $f \in \mathcal{C}^0(\mathbb{R}, \mathbb{C})$. It is then seen from equation (6.13) that $\varphi(\xi)$ is determined by its restriction $\varphi(\xi_0)$, in which case we obtain

$$\left(1 - \Lambda_{+}(\lambda; \xi_{0})\right) \varphi(\xi_{0}) = \frac{1}{v} \int_{\xi_{0}}^{\infty} e^{\left(\frac{1+\lambda}{v}\right)(\xi - \eta)} f(\eta) d\eta.$$

This can be solved for $\varphi(\xi_0)$ and, hence for $\varphi(\xi)$, if and only if

$$1 - \Lambda_+(\lambda; \xi_0) \neq 0.$$

This results in a bounded inverse which is defined on all of $\mathcal{C}^0(\mathbb{R}, \mathbb{C})$, and, therefore, all corresponding λ are in the resolvent set. On the other hand, we cannot invert the operator for λ such that

$$1 - \Lambda_{+}(\lambda; \xi_0) = 0.$$

In this case

$$(\mathcal{L} + \mathcal{N}_s - \lambda)\varphi = 0 \tag{6.14}$$

has nontrivial solutions, indicating that λ is in the point spectrum. Moreover, if we define the function

$$\mathcal{E}_{+}(\lambda;\xi_{0}) = 1 - \Lambda_{+}(\lambda;\xi_{0}), \qquad \frac{\Re(\lambda) + 1}{v} > 0,$$

we see that eigenvalues form the zero set. Similarly for $\frac{\Re e(\lambda)+1}{v} < 0$, integrating equation (6.12) over $(-\infty, \xi_0]$ yields a similar condition for the existence of eigenfunctions

$$1 = \Lambda_{-}(\lambda, \xi_0), \qquad \frac{\Re e(\lambda) + 1}{v} < 0$$

where

$$\Lambda_{-}(\lambda;\xi) = -\frac{1}{v|U'(\xi_0)|} \int_{-\infty}^{\xi} w(\eta - \xi_0) e^{\left(\frac{1+\lambda}{v}\right)(\xi - \eta)} d\eta.$$
 (6.15)

The Evans function is then defined as

$$\mathcal{E}(\lambda; \xi_0) = 1 - \Lambda_{\pm}(\lambda; \xi_0), \qquad \frac{\Re e(\lambda) + 1}{v} \ge 0.$$

Essential spectrum. Since \mathcal{N}_s does not contribute to the essential spectrum of $\mathcal{L} + \mathcal{N}_s$, we need only calculate the essential spectrum of the linear operator \mathcal{L} . The essential spectrum is the set of $\lambda = -1 + iv\rho$ where $\rho \in \mathbb{R}$. Since this has negative real-part, the essential spectrum does not contribute to any wave instabilities. We demonstrate that, for these values of λ , there exists bounded functions for which the inverse operator $(\mathcal{L} - \lambda)^{-1}$ becomes unbounded, indicating that λ is a member of the continuous spectrum.

Suppose $\lambda = -1 + iv\rho$ and consider the sequence of bounded functions [117]

$$\varphi_m(\xi) = \left(1 - e^{-\frac{\xi^2}{2m^2}}\right) e^{i\rho\xi}, \qquad m \in \mathbb{N}$$

for which

$$\|\varphi_m\|_{\infty} = 1, \quad \forall m \in \mathbb{N}, \ \rho \in \mathbb{R}.$$

However,

$$(\mathcal{L} - \lambda)\varphi_m(\xi) = \frac{v}{m^2} \xi e^{-\frac{\xi^2}{2m^2}} e^{i\rho\xi}$$

which implies that

$$\left\| (\mathcal{L} - \lambda) \varphi_m \right\|_{\infty} = \left\| \frac{v}{m^2} \right\| \xi e^{-\frac{\xi^2}{2m^2}} \right\|_{\infty} \longrightarrow 0, \quad \text{as} \quad m \longrightarrow \infty.$$

Hence, $(\mathcal{L} - \lambda)^{-1}$ is unbounded, and the set of $\lambda = -1 + iv\rho$ where $\rho \in \mathbb{R}$ form the essential spectrum. The residual spectrum in this case is empty, though we shall see that the vector system does, in fact, have a nonempty residual spectrum.

Evans function for an exponential weight distribution. We now explicitly calculate the zeros of the Evans functions for a Heaviside input and exponential weight distribution. The region in the complex plane $\mathbf{D} = \{z : \Re e(z) > -1\}$ is the domain of the Evans function \mathcal{E}_+ , and we need only consider this region to determine the stability of the wave. For v > 0 and $\lambda \in \mathbf{D}$,

$$\mathcal{E}_{+}(\lambda, \xi_{0}) = 1 - \frac{1}{v|U'(\xi_{0})|} \int_{\xi_{0}}^{\infty} w(\eta - \xi_{0}) e^{\left(\frac{1+\lambda}{v}\right)(\xi_{0} - \eta)} d\eta,
= 1 - \frac{1}{2(1+\lambda+v)} \frac{1}{|U'(\xi_{0})|},$$

and similarly for v < 0 and $\lambda \in \mathbf{D}$

$$\mathcal{E}_{-}(\lambda,\xi_{0}) = 1 + \frac{1}{v|U'(\xi_{0})|} \int_{-\infty}^{\xi_{0}} w(\eta - \xi_{0}) e^{\left(\frac{1+\lambda}{v}\right)(\xi_{0} - \eta)} d\eta,$$
$$= 1 + \frac{1}{2(1+\lambda+v)} \frac{1}{|U'(\xi_{0})|}.$$

Note that this recovers the Evans function obtained by Zhang [116] in the case of a homogeneous input. From this we can directly solve $\mathcal{E}_{\pm}(\lambda;\xi_0) = 0$ for λ

$$\lambda = -(1+|v|) + \frac{1}{2|U'(\xi_0)|}, \qquad v \in \mathbb{R}, \tag{6.16}$$

with $U'(\xi_0)$ determined from equation (6.2)

$$U'(\xi_0) = \frac{1}{v} \left(U(\xi_0) - \int_{-\infty}^{\xi_0} w(\xi_0 - \eta) d\eta - I(\xi_0) \right),$$

= $\frac{1}{v} \left(\kappa - \frac{1}{2} - I(\xi_0) \right),$

and κ satisfying the self-consistency conditions (6.5).

In the case $I_0 = 0$ the eigenvalues are given by

$$\lambda = -(1+|v|) + \frac{|v|}{2|\kappa - \frac{1}{2}|}, \qquad v \in \mathbb{R},$$
(6.17)

where v is the natural wave speed. Substituting equation (6.5) into (6.17) we find that the only eigenvalue in \mathbf{D} is the zero eigenvalue $\lambda = 0$. Moreover it can be shown that the eigenvalue is simple [116] and, hence, that the natural front is linearly stable, modulo uniform translations.

In the case of an inhomogeneous input $(I_0 > 0)$, we have to deal with each of the separate subdomains of the threshold conditions (6.5). First, for

v > 0, $\xi_0 > 0$ we notice that $I(\xi_0) = 0$ and κ is identical to the case of a natural wave, hence, $\lambda = 0$ is the only eigenvalue in **D**. If v > 0, $\xi_0 < 0$, substituting (6.5) for κ into (6.16) yields the eigenvalue

$$\lambda = -1 - v + \frac{v}{2|\kappa - \frac{1}{2} - I_0|}$$

$$= (1+v) \left[-1 + \frac{v}{|v + 2(1+v)I_0(1 - e^{\xi_0/v})|} \right].$$

Since $I_0(1 - e^{\xi_0/v}) > 0$ for all v > 0, $\xi_0 < 0$, $I_0 > 0$, it follows that $\lambda < 0$ and the corresponding front is always stable. On the other hand, if v < 0 and $\xi_0 < 0$, we find $\lambda = 0$, again indicating stability with respect to the degenerate family of waves corresponding to the boundary of the tongue. For $\xi_0 > 0$ we similarly calculate

$$\lambda = (1 + |v|) \left[-1 + \frac{|v|}{|v| + 2(1 + |v|)I_0 e^{\xi_0/v}} \right].$$

Since $2(1+|v|)I_0e^{\xi_0/v} > 0$ for v < 0, $\xi_0 > 0$, $I_0 > 0$, it again follows that $\lambda < 0$ and the corresponding front is always stable.

6.2 Stimulus-Locked Traveling Pulses in a Vector System

In this section we construct stimulus—locked traveling pulse solutions of equation (6.1) in the case of a unimodal input moving with constant velocity v. We first derive the formal solution for a general weight distribution w, and then use this to construct existence tongues in the (v, I_0) —plane for an exponential weight distribution and a Gaussian input of amplitude I_0 .

6.2.1 Existence of Stimulus-Locked Pulses

Consider a traveling pulse that is generated by, and locked to, an inhomogeneous input I traveling with constant speed v. Such a wave has permanent or *stationary* form, i.e., it translates as a rigid structure. Define the traveling wave coordinates (ξ, t) , where $\xi = x - vt$ and v is the velocity associated with

the input. A stimulus-locked traveling pulse is a pair of functions (U, Q), with $U, Q \in \mathcal{C}^1(\mathbb{R}, \mathbb{R})$, which in traveling wave coordinates satisfies the conditions

$$U(\xi_i) = \kappa,$$
 $i = 1, 2;$ $U(\xi) \longrightarrow 0$ as $\xi \longrightarrow \pm \infty;$ $U(\xi) > \kappa,$ $\xi_1 < \xi < \xi_2;$ $U(\xi) < \kappa,$ otherwise.

with ξ_1, ξ_2 defining the points at which the activity U crosses threshold and $s = \xi_2 - \xi_1$ defining the width of the input. Taking u(x,t) = U(x-vt) and $\varrho(x,t) = Q(x-vt)$, the profile of the pulse is governed by

$$-v U_{\xi} = -U - \beta Q + \int_{\xi_1}^{\xi_2} w(\xi - \eta) d\eta + I(\xi),$$

$$-\frac{v}{\epsilon} Q_{\xi} = -Q + U.$$

In general, we take the excitatory weight function w(x) to be nonnegative, continuous, symmetric in x, and monotonically decreasing in |x|. Let $\mathbf{s} = (U,Q)^T$ and W denote an antiderivative of w; we can rewrite the system more compactly as

$$\mathcal{L}\mathbf{s} \equiv \begin{pmatrix} vU_{\xi} - U - \beta Q \\ vQ_{\xi} + \epsilon U - \epsilon Q \end{pmatrix} = - \begin{pmatrix} N_e \\ 0 \end{pmatrix}, \tag{6.18}$$

where

$$N_e(\xi) = W(\xi - \xi_1) - W(\xi - \xi_2) + I(\xi). \tag{6.19}$$

We use variation of parameters to solve this linear equation. The homogeneous problem $\mathcal{L}\mathbf{s} = \mathbf{0}$ has the two linearly independent solutions,

$$\mathbf{S}_{+}(\xi) = \begin{pmatrix} \beta \\ m_{+} - 1 \end{pmatrix} \exp(\mu_{+} \xi), \qquad \mathbf{S}_{-}(\xi) = \begin{pmatrix} \beta \\ m_{-} - 1 \end{pmatrix} \exp(\mu_{-} \xi),$$

where

$$\mu_{\pm} = \frac{m_{\pm}}{v},$$
 $m_{\pm} = \frac{1}{2} \left(1 + \epsilon \pm \sqrt{(1 - \epsilon)^2 - 4\epsilon \beta} \right).$

We set

$$\mathbf{s}(\xi) = \left[\mathbf{S}_{+} \middle| \mathbf{S}_{-}\right] \left(\begin{array}{c} a(\xi) \\ b(\xi) \end{array} \right),$$

where $a, b \in \mathcal{C}^1(\mathbb{R}, \mathbb{R})$ and [A|B] denotes the matrix whose first column is defined by the vector A and whose second column is defined by the vector B. Since $\mathcal{L}\mathbf{S}_{\pm} = 0$, equation (6.18) becomes

$$\left[\mathbf{S}_{+}\middle|\mathbf{S}_{-}\right]\frac{\partial}{\partial\xi}\begin{pmatrix}a(\xi)\\b(\xi)\end{pmatrix} = -\frac{1}{v}\begin{pmatrix}N_{e}(\xi)\\0\end{pmatrix}.$$
 (6.20)

Since $[\mathbf{S}_{+}|\mathbf{S}_{-}]$ is invertible, we find

$$\frac{\partial}{\partial \xi} \begin{pmatrix} a(\xi) \\ b(\xi) \end{pmatrix} = -\frac{1}{v\beta(m_{+} - m_{-})} \left[\mathbf{Z}_{+} \middle| \mathbf{Z}_{-} \right]^{T} \begin{pmatrix} N_{e}(\xi) \\ 0 \end{pmatrix}.$$

where

$$\mathbf{Z}_{+}(\xi) = \begin{pmatrix} 1-m_{-} \\ \beta \end{pmatrix} \exp(-\mu_{+}\xi), \qquad \mathbf{Z}_{-}(\xi) = -\begin{pmatrix} 1-m_{+} \\ \beta \end{pmatrix} \exp(-\mu_{-}\xi).$$

For v > 0, we integrate over $[\xi, \infty)$ to obtain

$$\begin{pmatrix} a(\xi) \\ b(\xi) \end{pmatrix} = \begin{pmatrix} a_{\infty} \\ b_{\infty} \end{pmatrix} + \frac{1}{v\beta(m_{+} - m_{-})} \int_{\xi}^{\infty} \left[\mathbf{Z}_{+} \middle| \mathbf{Z}_{-} \right]^{T} \begin{pmatrix} N_{e}(\eta) \\ 0 \end{pmatrix} d\eta,$$

where a_{∞}, b_{∞} denote the values of $a(\xi), b(\xi)$ as $\xi \longrightarrow \infty$. Thus

$$\mathbf{s}(\xi) = \left[\mathbf{S}_{+} \middle| \mathbf{S}_{-} \right] \begin{pmatrix} a_{\infty} \\ b_{\infty} \end{pmatrix} + \frac{1}{v\beta(m_{+} - m_{-})} \left[\mathbf{S}_{+} \middle| \mathbf{S}_{-} \right] \int_{\xi}^{\infty} \left[\mathbf{Z}_{+} \middle| \mathbf{Z}_{-} \right]^{T} \begin{pmatrix} N_{e}(\eta) \\ 0 \end{pmatrix} d\eta. \tag{6.21}$$

Using the Hölder inequality and that $N_e \in \mathcal{C}^0(\mathbb{R}, \mathbb{R})$, it is straightforward to show that the integral term in (6.21) is bounded for all $\xi \in \mathbb{R}$; hence, a bounded solution **s** exists only if $a_{\infty} = b_{\infty} = 0$. The general stimulus-locked pulse is given by

$$\mathbf{s}(\xi) = \frac{1}{v\beta(m_{+} - m_{-})} \left[\mathbf{S}_{+} \middle| \mathbf{S}_{-} \right] \int_{\xi}^{\infty} \left[\mathbf{Z}_{+} \middle| \mathbf{Z}_{-} \right]^{T} \binom{N_{e}(\eta)}{0} d\eta.$$

Furthermore, if we define the functions

$$\mathcal{M}_{\pm}(\xi) = \frac{1}{v(m_{+} - m_{-})} \int_{\xi}^{\infty} e^{\mu_{\pm}(\xi - \eta)} N_{e}(\eta) d\eta,$$

we can express the solution (U, Q) as follows

$$U(\xi) = (1 - m_{-})\mathcal{M}_{+}(\xi) - (1 - m_{+})\mathcal{M}_{-}(\xi)$$
(6.22)

$$Q(\xi) = \beta^{-1}(m_{+} - 1)(1 - m_{-}) \Big(\mathcal{M}_{+}(\xi) - \mathcal{M}_{-}(\xi) \Big). \tag{6.23}$$

Since $N_e(\xi)$ is dependent upon ξ_1, ξ_2 , the threshold conditions $U(\xi_i) = \kappa$, where i = 1, 2 and $\xi_1 < \xi_2$, determine the relationship between the input strength I_0 and the position of the pulse relative to the input I. This provides the following consistency conditions for the existence of a stimulus-locked traveling pulse, which, we note, reduce to the case of natural pulses for $I_0 = 0$:

$$\kappa = (1 - m_{-})\mathcal{M}_{+}(\xi_{i}) - (1 - m_{+})\mathcal{M}_{-}(\xi_{i}) \qquad i = 1, 2 \tag{6.24}$$

6.2.2 Pulses for an Exponential Weight Distribution

Consider, in particular, an exponential weight distribution given by equation (6.4) with d=1 and a Gaussian input

$$I(x) = I_0 e^{-\left(\frac{x}{\sigma}\right)^2}. (6.25)$$

Existence conditions, determined from equations (6.24), yield the following system of nonlinear equations that determines the relationship between the input parameters (v, I_0) and the threshold points (ξ_1, ξ_2) .

$$\kappa = K(\xi_1 - \xi_2) + T_+(\xi_1) - T_-(\xi_1), \tag{6.26}$$

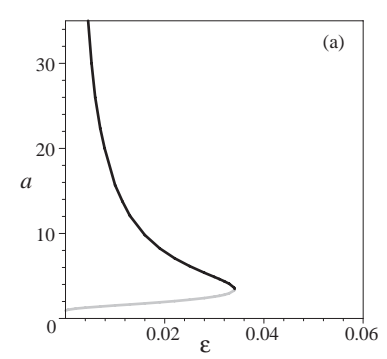
$$\kappa = J(\xi_1 - \xi_2) + T_+(\xi_2) - T_-(\xi_2), \tag{6.27}$$

where

$$\begin{split} J(\zeta) &= \frac{v + \epsilon}{2(v + m_+)(v + m_-)} \Big(1 - \mathrm{e}^{\zeta} \Big), \quad K(\zeta) = K_0 + K_1 \mathrm{e}^{\zeta} - K_+ \mathrm{e}^{\mu_+ \zeta} + K_- \mathrm{e}^{\mu_- \zeta}, \\ K_1 &= \frac{1}{2} \frac{v - \epsilon}{(v - m_+)(v - m_-)}, \qquad K_{\pm} = \frac{v^2 (1 - m_{\mp})}{m_{\pm} (v^2 - m_{\pm}^2)(m_+ - m_-)}, \\ K_0 &= \left(\frac{(1 - m_-)(2v + m_+)}{2m_+(v + m_+)(m_+ - m_-)} \right) - \left(\frac{(1 - m_+)(2v + m_-)}{2m_-(v + m_-)(m_+ - m_-)} \right), \\ T_{\pm}(\zeta) &= \frac{\sqrt{\pi} \ \sigma I_0}{2 \ v} \left(\frac{1 - m_{\mp}}{m_+ - m_-} \right) \exp\left((\mu_{\pm} \sigma)^2 / 4 + \mu_{\pm} \zeta \right) \mathrm{erfc} \left(\frac{\zeta}{\sigma} + \frac{\mu_{\pm} \sigma}{2} \right), \end{split}$$

and $\mathbf{erfc}(z)$ denotes the complementary Error function.

Natural traveling pulses ($I_0 = 0$). Numerically solving equations (6.26) and (6.27) for $I_0 = 0$, we find that for sufficiently small ϵ there exists a pair of traveling pulses arising from a saddle-node bifurcation. Previous numerical [80] simulations suggest that the larger and faster pulse is stable while the smaller slower pulse is unstable and acts as a separatrix between the fast pulse and the rest state. Zhang's [116] analysis has shown the fast pulse to be stable in the singular limit $\epsilon \longrightarrow 0$. In Figure 6.2 we present bifurcation diagrams using ϵ as a bifurcation parameter to demonstrate the existence and stability of natural pulses; stability is determined by numerically solving for the zero set of the Evans function, constructed in section 6.3.2. It is found that, away from the singular limit, the larger, faster pulse is stable (black) while the smaller, slower pulse is unstable (gray).



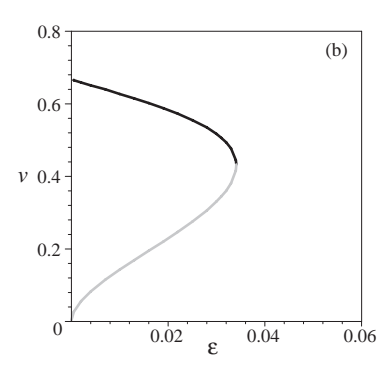


Figure 6.2. Bifurcation curves for the existence of natural traveling pulses $(I_0 = 0)$ for the vector system (6.1) in (a) the (ϵ, a) -plane and (b) the (ϵ, v) -plane, illustrating that natural pulses exist only for small ϵ . The stable branch (black), characterized by wide (large a), fast pulses, and the unstable branch (gray), characterized by narrow, slow pulses, annihilate in a saddle-node bifurcation at a critical value ϵ_c . In this case $\kappa = 0.3$, $\beta = 2.5$, and $\epsilon_c \approx 0.341$.

Stimulus-locked traveling pulses. Numerically solving equations (6.26) and (6.27) for $I_0 > 0$, we determine the regions in the (v, I_0) -plane where one or more stimulus-locked pulses exist. Performing a continuation from the pair of natural pulses, we generate a corresponding pair of existence tongues with tips at $I_0 = 0$. These are illustrated in Figure 6.3 with the left-hand (righthand) tongue emerging from the unstable (stable) natural pulse. We then note that the left-hand tongue includes stationary pulses at v=0. In Chapters 4 and 5 we have shown how a stationary unimodal input can generate a stable stationary pulse that bifurcates to a stable breather via a Hopf bifurcation as the input amplitude is reduced. In section 6.3.2 we construct the associated Evans function for traveling pulses within the tongue regions and use this to determine the stability of stimulus-locked pulses. We find that there is a Hopf curve within the left-hand tongue that is a continuation of the Hopf bifurcation point for stationary pulses (v=0); this is shown in Figure 6.3 by the gray curve. Above the Hopf curve the pulse is stable, while it is unstable below. Conversely, the pulse within the right-hand tongue is always stable. Note that there also exists additional stimulus-locked pulse solutions in certain subregions inside and outside of the tongues; however, these are found to be always unstable.

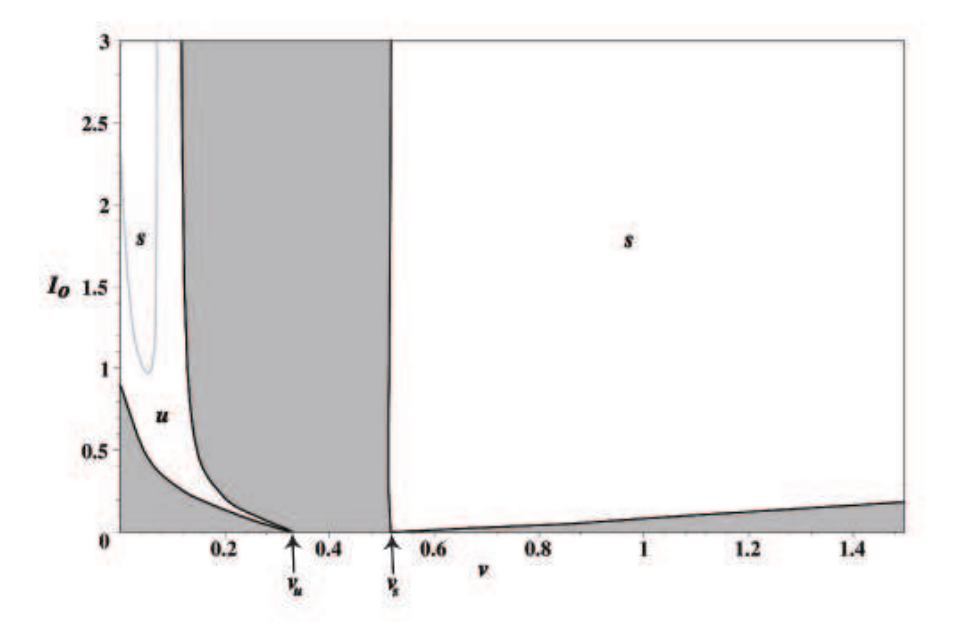


Figure 6.3. Regions of existence (white) of the stimulus-locked traveling pulses in the (v, I_0) -plane for $\sigma = 1.0$, $\kappa = 0.3$, $\epsilon = 0.03$, and $\beta = 2.5$. The left and right regions form tongues that issue from the unstable v_u and stable v_s natural traveling pulses, respectively. The Hopf curve within the left-hand tongue is shown in gray, above which the pulse is stable (s) and below which it is unstable (u); see section 6.3. Stationary pulses correspond to the intersection of the tongue and the line v = 0.

6.3 Stability of the Stimulus-Locked Traveling Pulse

We begin by analyzing the resolvent and the spectrum of the operator associated with the linearization of the vector system (6.1) about the general stimulus-locked traveling pulse constructed in section 6.2.1. This analysis indicates that potential instabilities arise only due to the behavior of eigenvalues, which can be determined by calculation of the zero set of the Evans function. We then present the explicit construction of the Evans function for the stimulus-locked traveling pulse, in the particular case of the exponential weight distribution, and calculate the zero sets of this Evans function for the pulse existence tongues shown in Figure 6.3, thereby determining their stability.

6.3.1 Spectral Analysis of the Linearized Operator

Consider the evolution of small smooth perturbations of the stimulus-locked traveling pulse with stationary form (U, Q),

$$u = U + \bar{\varphi},$$
 $\varrho = Q + \bar{\psi}.$

Substituting into the system expressed in traveling wave coordinates and linearizing, we find the perturbations, to first order, satisfy

$$\frac{\partial \bar{\varphi}}{\partial t} - v \frac{\partial \bar{\varphi}}{\partial \xi} + \bar{\varphi} + \beta \bar{\psi} = \int_{\mathbb{R}} w(\xi - \eta) H'(U(\eta) - \kappa) \bar{\varphi}(\eta) d\eta, \tag{6.28}$$

$$\frac{\partial \bar{\psi}}{\partial t} - v \frac{\partial \bar{\psi}}{\partial \xi} - \epsilon \bar{\varphi} + \epsilon \bar{\psi} = 0. \tag{6.29}$$

Separating variables,

$$\begin{pmatrix} \bar{\varphi}(\xi,t) \\ \bar{\psi}(\xi,t) \end{pmatrix} = \begin{pmatrix} \varphi(\xi) \\ \psi(\xi) \end{pmatrix} e^{\lambda t}$$
 (6.30)

the spatial components $\varphi, \psi \in \mathcal{C}^1(\mathbb{R}, \mathbb{C})$ satisfy the spectral problem

$$(\mathcal{L} + \mathcal{N}_s) \begin{pmatrix} \varphi \\ \psi \end{pmatrix} = \lambda \begin{pmatrix} \varphi \\ \psi \end{pmatrix} \tag{6.31}$$

where

$$\mathcal{L} = v \frac{\partial}{\partial \xi} - \mathcal{A}, \qquad \qquad \mathcal{A} = \begin{bmatrix} 1 & \beta \\ -\epsilon & \epsilon \end{bmatrix}, \qquad (6.32)$$

$$\mathcal{N}_s \begin{pmatrix} \varphi \\ \psi \end{pmatrix} = \begin{pmatrix} \frac{w(\xi - \xi_1)}{|U'(\xi_i)|} \varphi(\xi_1) + \frac{w(\xi - \xi_2)}{|U'(\xi_2)|} \varphi(\xi_2) \\ 0 \end{pmatrix}. \tag{6.33}$$

Resolvent and the point spectrum. Letting $\mathbf{z} = (\varphi, \psi)^T$, we seek to construct a bounded inverse by solving

$$(\mathcal{L} + \mathcal{N}_s - \lambda)\mathbf{z} = -\mathbf{f},$$

where $\mathbf{f} = (f_1, f_2)^T$ and $f_1, f_2 \in \mathcal{C}^0(\mathbb{R}, \mathbb{C})$. Following the variation of parameters approach of Zhang [116], we find the linearly independent solutions of the homogeneous problem $(\mathcal{L} - \lambda)\phi = 0$ are

$$\mathbf{\Phi}_{+}(\xi,\lambda) = \begin{pmatrix} \beta \\ m_{+}-1 \end{pmatrix} e^{\left(\frac{\lambda+m_{+}}{v}\right)\xi} \qquad \mathbf{\Phi}_{-}(\xi,\lambda) = \begin{pmatrix} \beta \\ m_{-}-1 \end{pmatrix} e^{\left(\frac{\lambda+m_{-}}{v}\right)\xi},$$

in which case we set

$$\mathbf{z}(\xi) = \left[\mathbf{\Phi}_{+}\middle|\mathbf{\Phi}_{-}\right]\left(rac{ar{a}(\xi)}{ar{b}(\xi)}\right).$$

Subsequently, the coefficient functions are determined according to

$$\left[\mathbf{\Phi}_{+}\middle|\mathbf{\Phi}_{-}\right]\frac{\partial}{\partial\xi}\left(\begin{array}{c}\bar{a}\\\bar{b}\end{array}\right) = -\frac{1}{v}\left(\mathcal{N}_{s}\mathbf{z} + \mathbf{f}\right). \tag{6.34}$$

Inversion of $\left[\Phi_{+} \middle| \Phi_{-} \right]$ leads to

$$\frac{\partial}{\partial \xi} \begin{pmatrix} \bar{a} \\ \bar{b} \end{pmatrix} = -\frac{1}{v\beta(m_{+} - m_{-})} \left[\mathbf{\Psi}_{+} \middle| \mathbf{\Psi}_{-} \right]^{T} \left(\mathcal{N}_{s} \mathbf{z} + \mathbf{f} \right)$$
(6.35)

where

$$\Psi_{+}(\xi,\lambda) = \begin{pmatrix} 1-m_{-} \\ \beta \end{pmatrix} e^{-\left(\frac{\lambda+m_{+}}{v}\right)\xi}, \qquad \Psi_{-}(\xi,\lambda) = -\begin{pmatrix} 1-m_{+} \\ \beta \end{pmatrix} e^{-\left(\frac{\lambda+m_{-}}{v}\right)\xi}.$$

For $\Re(\lambda) > -m_-$, we integrate over $[\xi, \infty)$ to obtain

$$\begin{pmatrix} \bar{a}(\xi) \\ \bar{b}(\xi) \end{pmatrix} = \begin{pmatrix} \bar{a}_{\infty} \\ \bar{b}_{\infty} \end{pmatrix} + \frac{1}{v\beta(m_{+} - m_{-})} \int_{\xi}^{\infty} \left[\mathbf{\Psi}_{+} \middle| \mathbf{\Psi}_{-} \right]^{T} (\mathbf{N}_{s} \mathbf{z} + \mathbf{f}) d\eta,$$

where $\bar{a}_{\infty}, \bar{b}_{\infty}$ denotes the values of $a(\xi), b(\xi)$ as $\xi \longrightarrow \infty$. Thus

$$\mathbf{z}(\xi) = \left[\mathbf{\Phi}_{+}\middle|\mathbf{\Phi}_{-}\right]\left(\frac{\bar{a}_{\infty}}{\bar{b}_{\infty}}\right) + \frac{1}{v\beta(m_{+} - m_{-})}\left[\mathbf{\Phi}_{+}\middle|\mathbf{\Phi}_{-}\right]\int_{\xi}^{\infty}\left[\mathbf{\Psi}_{+}\middle|\mathbf{\Psi}_{-}\right]^{T}(\aleph_{s}\mathbf{z} + \mathbf{f})d\eta.$$

As we shall discuss, the integral term is bounded for all ξ , and, consequently, for a bounded solution to exist, we must require that $\bar{a}_{\infty} = \bar{b}_{\infty} = 0$. Thus

$$\mathbf{z}(\xi) = \frac{1}{v\beta(m_+ - m_-)} \Big[\mathbf{\Phi}_+ \big| \mathbf{\Phi}_- \Big] \int_{\xi}^{\infty} \Big[\mathbf{\Psi}_+ \big| \mathbf{\Psi}_- \Big]^T \big(\mathcal{N}_s \mathbf{z} + \mathbf{f} \big) d\eta.$$

which can be rewritten as

$$\begin{pmatrix} \varphi(\xi) \\ \psi(\xi) \end{pmatrix} - \Lambda_1(\lambda, \xi) \begin{pmatrix} \varphi(\xi_1) \\ 0 \end{pmatrix} - \Lambda_2(\lambda, \xi) \begin{pmatrix} \varphi(\xi_2) \\ 0 \end{pmatrix} = \mathcal{H}(\xi)$$
 (6.36)

where

$$\Lambda_{i}(\lambda,\xi) = \frac{1}{v\beta(m_{+} - m_{-})} \left[\mathbf{\Phi}_{+} \middle| \mathbf{\Phi}_{-} \right] \int_{\xi}^{\infty} \left[\mathbf{\Psi}_{+} \middle| \mathbf{\Psi}_{-} \right]^{T} \frac{w(\eta - \xi_{i})}{|U'(\xi_{1})|} d\eta$$

$$\mathcal{H}(\xi) = \frac{1}{v\beta(m_{+} - m_{-})} \left[\mathbf{\Phi}_{+} \middle| \mathbf{\Phi}_{-} \right] \int_{\xi}^{\infty} \left[\mathbf{\Psi}_{+} \middle| \mathbf{\Psi}_{-} \right]^{T} \mathbf{f}(\eta) d\eta.$$

Elements of Λ_i and \mathcal{H} are finite sums of terms of the forms

$$\int_{\xi}^{\infty} e^{\left(\frac{\lambda + m_{\pm}}{v}\right)(\xi - \eta)} w(\eta - \xi_{i}) d\eta, \qquad \int_{\xi}^{\infty} e^{\left(\frac{\lambda + m_{\pm}}{v}\right)(\xi - \eta)} f_{i}(\eta) d\eta.$$

Using the Hölder inequality, it is straightforward to show that these terms, and hence Λ_i and \mathcal{H} , are bounded for all $\xi \in \mathbb{R}$ and for all $f_i \in \mathcal{C}^{\circ}(\mathbb{R}, \mathbb{C})$. Now we must determine the conditions under which equation (6.36) has a unique solution. Since the solution $\mathbf{z}(\xi)$ is determined completely by the restrictions $\mathbf{z}(\xi_1)$ and $\mathbf{z}(\xi_2)$, we obtain the following finite dimensional system by substituting $\xi = \xi_1, \xi_2$ into (6.36).

$$\left(\mathbf{I} - \Delta(\lambda)\right) \begin{pmatrix} \varphi(\xi_1) \\ \varphi(\xi_2) \end{pmatrix} = \begin{pmatrix} \mathcal{H}_1(\xi_1) \\ \mathcal{H}_1(\xi_2) \end{pmatrix},$$

where $\mathcal{H} = (\mathcal{H}_1, \mathcal{H}_2)^T$, $\bar{\Lambda}_i(\lambda, \xi) = (1\ 0)\ \Lambda_i(\lambda, \xi)\ (1\ 0)^T$, and

$$\Delta(\lambda, \xi_1, \xi_2) = \begin{pmatrix} \bar{\Lambda}_1(\lambda, \xi_1) & \bar{\Lambda}_2(\lambda, \xi_1) \\ \bar{\Lambda}_1(\lambda, \xi_2) & \bar{\Lambda}_2(\lambda, \xi_2) \end{pmatrix}.$$

This system has a unique solution if and only if $\det(\mathbf{I} - \Delta(\lambda)) \neq 0$, resulting in a bounded inverse defined on all of $\mathcal{C}^{0}(\mathbb{R}, \mathbb{C}) \times \mathcal{C}^{0}(\mathbb{R}, \mathbb{C})$. All such λ are elements of the resolvent set. Conversely, we cannot invert the operator for λ such that

$$\det(\mathbf{I} - \Delta(\lambda, \xi_1, \xi_2)) = 0,$$

in which case there exists nontrivial solutions to

$$(\mathcal{L} + \mathcal{N}_s - \lambda)\mathbf{z} = 0$$

and λ is an element of the point spectrum. Consequently, the function

$$\mathcal{E}(\lambda, \xi_1, \xi_2) = \det\left(\mathbf{I} - \Delta(\lambda, \xi_1, \xi_2)\right), \qquad \Re(\lambda) > -m_-$$
 (6.37)

identifies eigenvalues with its zero set, indicating that \mathcal{E} is an Evans function on the set for which $\Re e(\lambda) > -m_-$. Analogously, an Evans function can be

defined for $\Re(\lambda) < -m_+$; however, we do not pursue the explicit construction as it does not reflect an instability of the stimulus-locked wave.

Continuous Spectrum. Using arguments similar to the case of the scalar equation, it can be shown that the operator $\mathcal{N}_s: \mathcal{C}^1(\mathbb{R},\mathbb{C}) \times \mathcal{C}^1(\mathbb{R},\mathbb{C}) \longrightarrow \mathcal{C}^0(\mathbb{R},\mathbb{C}) \times \mathcal{C}^0(\mathbb{R},\mathbb{C})$ is compact. Again this implies that the essential spectrum of $\mathcal{L} + \mathcal{N}_s$ is identical to that of \mathcal{L} . In the case of the vector operator \mathcal{L} , the continuous spectrum is the union of the disjoint sets of $\lambda = -m_{\pm} + iv\rho$ where $\rho \in \mathbb{R}$. To see this, assume such λ and consider the sequence of functions $\phi_n^{\pm} \in \mathcal{C}^1(\mathbb{R}, \mathbb{C}) \times \mathcal{C}^1(\mathbb{R}, \mathbb{C})$, where n is a positive integer, \mathcal{Y}_{\pm} are the eigenvectors of the matrix \mathcal{A} , defined in (6.32), corresponding to the eigenvalues m_{\pm} , and

$$\phi_n^{\pm}(\xi) = e^{i\rho\xi} \left(1 - e^{-\frac{\xi^2}{2n^2}}\right) \mathcal{Y}_{\pm}.$$

 \mathcal{Y}_{\pm} are normalized so that $\left\|\phi_{n}^{\pm}\right\|_{\infty} = 1$ for all n; however,

$$\left\| \mathcal{L}\phi_n^{\pm} \right\| = \frac{v}{n^2} \left\| \xi e^{-\frac{\xi^2}{2n^2}} \right\| \longrightarrow 0, \quad \text{as} \quad n \longrightarrow \infty.$$

Hence, $(\mathcal{L}-\lambda)^{-1}$ is unbounded, and λ lies in the continuous spectrum of $\mathcal{L}+\mathcal{N}_s$.

Residual Spectrum. To complete the characterization of the spectrum, we demonstrate that the set $\{\lambda \in \mathbb{C} : \Re(\lambda) \in (-m_+, -m_-)\}$ defines the residual spectrum of $\mathcal{L} + \mathcal{N}_s$. We must show that for such λ there exists a bounded inverse whose domain is not dense in $\mathcal{C}^0(\mathbb{R}, \mathbb{C}) \times \mathcal{C}^0(\mathbb{R}, \mathbb{C})$. Consider our previous construction of the inverse $(\mathcal{L} + \mathcal{N}_s - \lambda)^{-1}$. Since we need only calculate the residual spectrum of \mathcal{L} , we integrate (6.35) over [c, d], neglecting \mathcal{N}_s , to obtain

$$\left(\frac{\bar{a}(d)}{\bar{b}(d)} \right) - \left(\frac{\bar{a}(c)}{\bar{b}(c)} \right) = -\frac{1}{v\beta(m_+ - m_-)} \int_c^d \left[\mathbf{\Psi}_+ \big| \mathbf{\Psi}_- \right]^T f(\eta) d\eta.$$

There are only two cases to consider. First, taking $c = \xi$ and $d = \infty$, we examine the integral term of $\mathbf{z}(\xi)$, components of which have the form

$$\int_{\xi}^{\infty} e^{\left(\frac{\lambda + m_{\pm}}{v}\right)(\xi - \eta)} \left[(1 - m_{\mp}) f_1(\eta) + \beta f_2(\eta) \right] d\eta.$$

Since $\lambda + m_- < 0$ and v > 0, all components are bounded, and hence $\mathcal{L} + \mathcal{N}_s - \lambda$ is bounded only if f either decays sufficiently fast such that

$$\int_{\xi}^{\infty} e^{\left(\frac{\lambda + m_{+}}{v}\right)(\xi - \eta)} \left[(1 - m_{-}) f_{1}(\eta) + \beta f_{2}(\eta) \right] d\eta < \infty, \qquad \xi \in \mathbb{R}$$

or satisfies $(1 - m_-)f_1(\eta) + \beta f_2(\eta) = 0$ for all η . Similarly, for $c = -\infty$ and $d = \xi$, we must require that

$$\int_{-\infty}^{\xi} e^{\left(\frac{\lambda + m_{-}}{v}\right)(\xi - \eta)} \left[(1 - m_{+}) f_{1}(\eta) + \beta f_{2}(\eta) \right] d\eta < \infty, \qquad \xi \in \mathbb{R}.$$

or $(1 - m_+)f_1(\eta) + \beta f_2(\eta) = 0$ for all η . Since the union of all such f is not dense in $\mathcal{C}^0(\mathbb{R}, \mathbb{C}) \times \mathcal{C}^0(\mathbb{R}, \mathbb{C})$, we conclude that λ lies in the residual spectrum.

6.3.2 Evans Function for Stimulus-Locked Traveling Pulses

The following gives the explicit construction of the Evans function for stimuluslocked pulses in the case of a Gaussian input, Heavside firing rate function, and exponential weight distribution and includes natural pulses ($I_0 = 0$). After a lengthy calculation,

$$\mathcal{E}(\lambda, \xi_1, \xi_2) = \det\left(\mathbf{I} - \Delta(\lambda, \xi_1, \xi_2)\right), \qquad \mathcal{R}e(\lambda) > -m_{-}$$

$$= \left(1 - \frac{\Theta_{+}(\lambda)}{\left|U'(\xi_1)\right|}\right) \left(1 - \frac{\Theta_{+}(\lambda)}{\left|U'(\xi_2)\right|}\right) - \frac{\Theta_{+}(\lambda)\Gamma(\lambda)}{\left|U'(\xi_1)U'(\xi_2)\right|} e^{(\xi_1 - \xi_2)}, \quad (6.38)$$

where

$$\Gamma_{\pm}(\lambda) = \frac{(1 - m_{\mp})v}{(m_{+} - m_{-})(v^{2} - (\lambda + m_{\pm})^{2})}$$

$$\Theta_{\pm}(\lambda) = \frac{1}{2(m_{+} - m_{-})} \left(\frac{1 - m_{-}}{\lambda + m_{+} \pm v} - \frac{1 - m_{+}}{\lambda + m_{-} \pm v} \right)$$

$$\Gamma(\lambda) = \Theta_{-}(\lambda)e^{(\xi_{1} - \xi_{2})} + \Gamma_{+}(\lambda)e^{\left(\frac{\lambda + m_{+}}{v}\right)(\xi_{1} - \xi_{2})} - \Gamma_{-}(\lambda)e^{\left(\frac{\lambda + m_{-}}{v}\right)(\xi_{1} - \xi_{2})}$$
(6.39)

Since the zero set of the Evans function (6.38) comprises solutions of a trancendental equation, we solve for the eigenvalues numerically by finding the intersection points of the zero sets of the real and complex parts of the Evans function. This leads to the stability results shown in Figure 6.3, namely, that pulses within the right-hand tongue are stable whereas pulses within the left-hand tongue are only stable if they lie inside the region enclosed by the Hopf bifurcation curve. An example of a zero set construction is shown in Figure 6.4 for fixed I_0 and various values of v. From these graphs we see that, as the speed of the input varies, a pair of complex eigenvalues traverses the imaginary axis twice, ultimately becoming a pair of real eigenvalues.

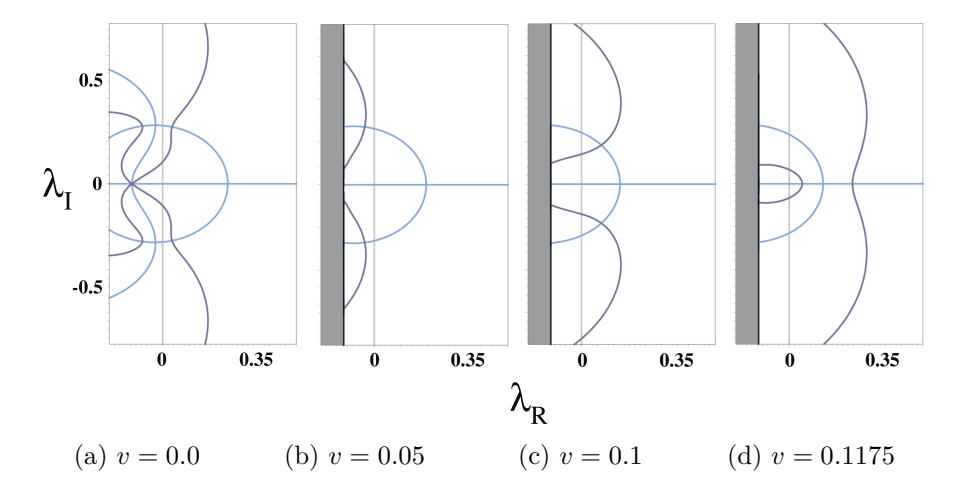


Figure 6.4. Graphs of the zero sets of the real (dark curves) and imaginary (light curves) parts of the Evans functions for $I_0 = 2.0$ and a sequence of stimulus speeds v; intersection points indicate eigenvalues. The vertical shaded region $\Re(\lambda) \leq -m_{-}$ indicates the essential spectrum, and the vertical gray line indicates the imaginary axis. This sequence of plots indicates that two Hopf bifurcation points occur, defining the boundary of the stable region within the left tongue depicted in Figure 6.3. (a) is associated with the existence of a stable stationary breather, (b) with a stable traveling pulse, and (c,d) with a traveling emitter. See section 6.3.3 for more details.

Linear stability of the traveling pulse solution is characterized by all eigenvalues of the linearized operator having negative real part, with the possible exception that $\lambda=0$ is a simple eigenvalue. Moreover, Hopf bifurcations may be identified by a pair of complex eigenvalues crossing the imaginary axis from the left-half plane. The sequence of plots in Figure 6.4 indicates how we arrive at the Hopf bifurcation curve in Figure 6.3. It has been found in many infinite-dimensional dynamical systems, for example, semilinear parabolic equations, that the criteria for a Hopf bifurcation carry over from ordinary differential equations. Although smoothness properties of the flow are required for its proof using invariant manifold theory, the result essentially relies on the behavior of eigenvalues of the linearized operator [71]. We shall assume this and use numerical simulations to explore the behavior of the model near and beyond these bifurcation points.

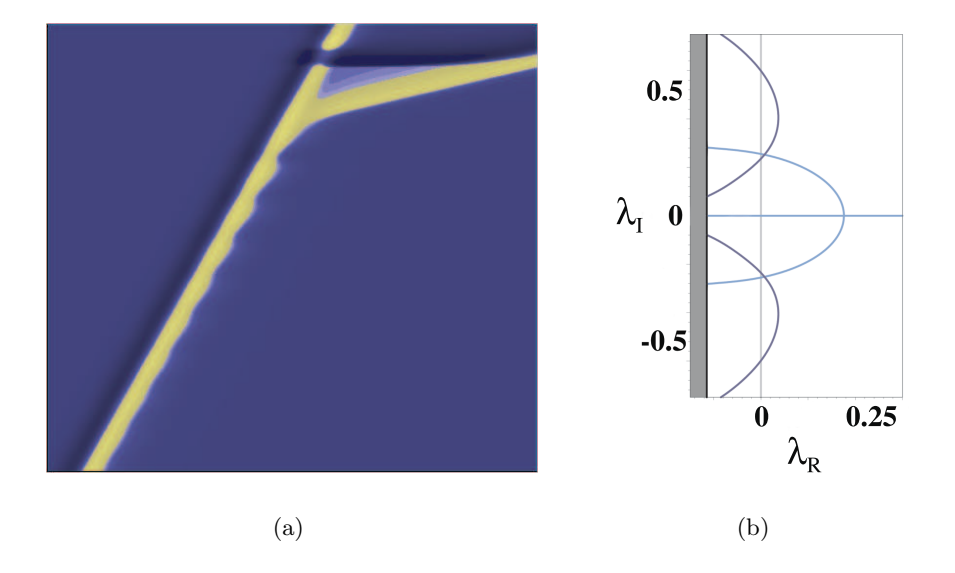


Figure 6.5. Instability of the stimulus-locked traveling pulse in the presence of two complex conjugate eigenvalues with positive real part for $I_0=1.0$, v=0.07, $\sigma=1$, $\kappa=0.3$, $\epsilon=0.03$, and $\beta=2.5$. In this case the bifurcation appears subcritical with the absence of a sharp jump to a stable breathing pulse. Instead, instability manifests itself as a periodic cycling of an initial phase of periodically-modulated growth of the active region, followed ultimately by the shedding of a natural traveling pulse. (a) Space—time plot showing one cycle of the instability, where the vertical axis represents time and the horizontal axis represents space. (b) Graph of the corresponding zero set of the Evans function. The periodic process of shedding or emitting natural traveling pulses becomes more rapid as the real part of the eigenvalue increases.

6.3.3 Numerical Simulations

In this section we explore the behavior of the vector system (6.1) in all regions of the (v, I_0) -plane shown in Figure 6.3. In particular we describe the various types of solutions that emerge beyond the Hopf bifurcation curve, as well as beyond the existence tongues.

For parameter values supporting natural traveling pulses, and in the absence of an input $(I_0 = 0)$, an initial, sufficiently large, local displacement of the activity u from rest induces a locally excited region of activity, which rapidly develops into a pair of diverging natural traveling pulses, as in the reaction-diffusion analogue. Similarly, for parameter values supporting stable stimulus-locked pulses in the presence of an input $(I_0 > 0)$, an initial displacement of u near the input (or no initial displacement in the case of sufficiently large input strength I_0) rapidly approaches the stable traveling pulse. For certain speeds v the initial transient can generate an additional single or pair of traveling waves that propagate away from the input. As expected the speed and width of the stimulus-locked traveling pulse closely match that of the theory.

Interestingly, for the parameter values in Figure 6.3, numerical simulations suggest that the left branch of the Hopf curve (gray) corresponds to a supercritical bifurcation, while the right branch is subcritical without a sharp transition to a breathing pulse. We first characterize the nature of solutions obtained by crossing the subcritical branch of the Hopf curve. We find a region of activity moving with the input whose right boundary oscillates with increasing amplitude. After a critical point, the system emits a natural traveling pulse, whose speed is faster than that of the input, as shown in Figure 6.5. The region between the one excited by the input and the new natural pulse recovers, and the process repeats periodically. We refer to such solutions as pulse-emitters. The smaller the real-part of the eigenvalue, the slower the instability grows and the more time is required for the wave to be emitted. As v is increased, the real part of the eigenvalue grows and the number of oscillations occurring before the shedding of natural waves decreases, until the eigenvalues become real, as illustrated in the Figure sequence 6.4(b-d), and the pulse rapidly emits natural pulses. This unstable behavior continues until v is increased to the boundary of the right-hand tongue where there is a smooth transition to a stable stimulus-locked pulse.

When the left-hand supercritical branch of the Hopf curve is crossed by reducing I_0 or v, we find a smooth transition to a stimulus-locked traveling breather. In the special case of a stationary stimulus (v = 0), reducing I_0 generates a stationary breather as we have shown previously [12, 33]. The breathing solutions continue to persist in a subregion of the (v, I_0)-plane bounded to the right by the left (supercritical) branch of the Hopf curve in 6.3. As one moves in this subregion away from the left Hopf branch, the amplitude of

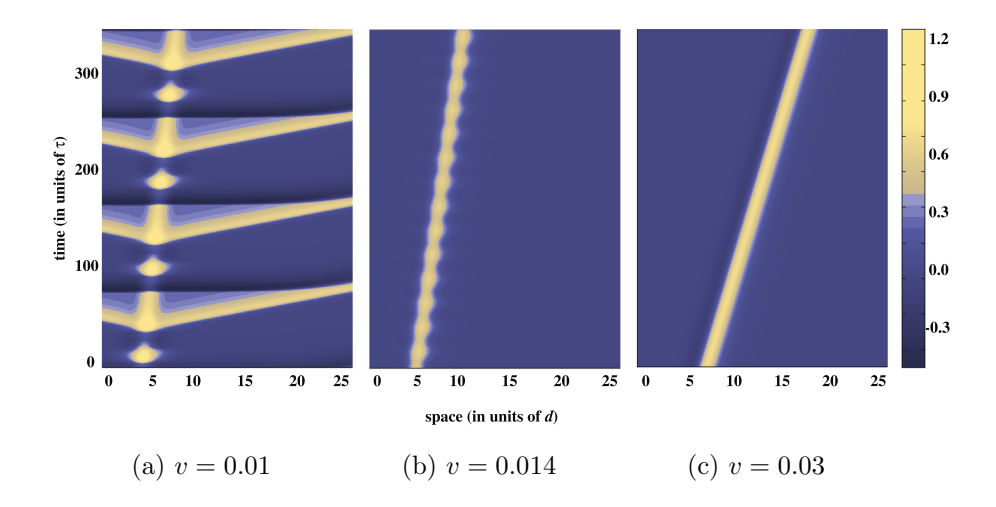


Figure 6.6. Sequence of spacetime plots for fixed input $I_0 = 1.5$, illustrating the transition from pulse-emitter, to breather, to stimulus-locked pulse as v increases through the supercritical branch of the Hopf curve shown in 6.3. Other parameters are $\epsilon = 0.03$, $\kappa = 0.3$, $\beta = 2.5$, $\sigma = 1$.

the oscillations grows. After some point, the breathing solution disappears and a new type of temporally periodic solution appears, each cycle of which is characterized by one or more breathing pulse oscillations followed by the emission of a pair of natural waves, possibly intermixed with interludes of subthreshold behavior. The transition from breathing pulse to emitting pulse may be due to a subcritical period-doubling bifurcation, a possible candidate for the transition to pulse-emitter in the case of a stationary input; see section 4.2. An example of such a transition is illustrated in Figure 6.6. This type of pulse-emitting solution appears to be part of a family of related responses of the system to a localized input, occurring whenever the associated traveling pulse (or breather) is either unstable or nonexistent. This includes the emitters found within the region between the subcritical Hopf curve and the stable right tongue shown in Figure 6.3, and, consequently, there is a smooth transition of behaviors joining the two regions, as shown in Figure 6.7. Analogous to the case of a stationary input, more complicated mode-locking phenomena is also observed.

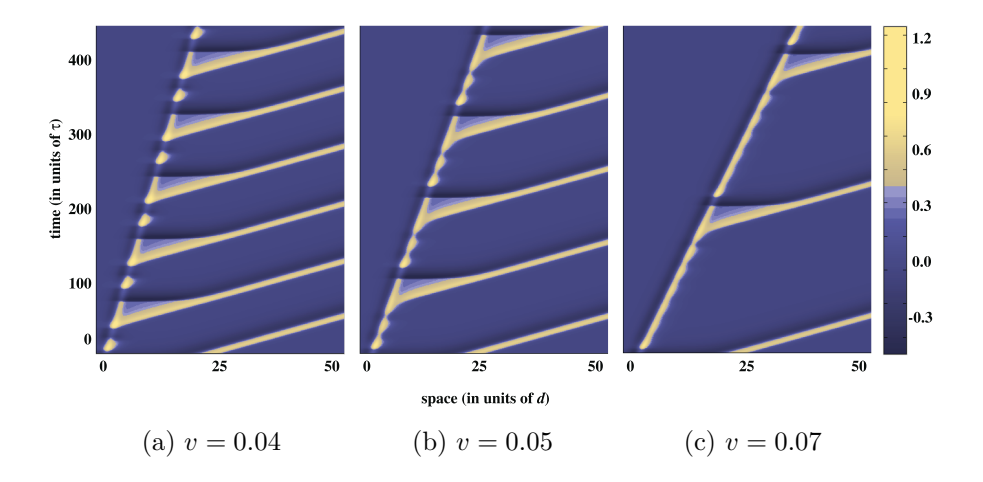


Figure 6.7. Transitions between various pulse-emitting solutions for fixed $I_0 = 0.9$ as v is increased. These solutions exist within and adjacent to the unstable part of the left-hand tongue of Figure 6.3, sufficiently below the Hopf curve that stable breathers no longer exist. Other parameters are $\epsilon = 0.03$, $\kappa = 0.3$, $\beta = 2.5$, $\sigma = 1$.

6.4 Discussion

In this chapter we have shown how to extend the analysis of the existence and stability of pulses arising from a stationary stimulus input to that of a input moving with constant speed. We described the continuation from the unstable/stable pair of natural pulses by constructing a corresponding pair of existence tongues emerging from the natural pulses at $I_0 = 0$, with the left-hand tongue including stationary pulses at v=0, for a particular choice of parameter values supporting natural pulses. We have extended Zhang's analysis of stability of natural pulses to that of stimulus-locked pulses and numerically evaluated the Evans function to determine eigenvalues away from the singular limit $\epsilon \to 0$. This allowed us to analyze the stability of the existence tongues in the (v, I_0) -plane and show the continuation of the Hopf bifurcation found for stationary pulses. Numerically this Hopf curve was found to have a supercritical branch, from which breathing pulses emerge and a subcritical branch from which no breathing pulse emerges. In general for parameter values that do not support either stimulus-locked pulses or breathers, the system generates more complicated unstable behavior including the emission of natural

traveling pulses, when such waves exist.

It would be interesting to contrast the type of local inhibition analyzed herein, primarily due to intrinsic neuronal properties, with that of nonlocal inhibition, arising from the ubiquitous inhibitory populations of neurons found in cortex. From previous work [1, 81], we know that the two-population, excitatory-inhibitory system supports stable stationary pulses which, moreover, can undergo a subcritical Hopf bifurcation. In this case no breathing pulse emerges. However, it is likely that the presence of a localized input is capable of stabilizing such a breathing pulse solution. In addition it would be interesting to provide a more thorough analysis of the scalar model considered by Xie & Giese [111].

As mentioned at the end of Chapter 4, persistent currents tend to destroy neurons. It may be possible test our predictions regarding moving stimuli in cortical slice preparations, since a moving stimulus would only expose a neuron to a sustained current for a short interval of time. Of course, constructing such a stimulus does, in fact, presents a serious experimental challenge. Nevertheless, more comparisons between models and experiments need to occur in order to gain confidence in the relevance of these equations to neural tissue. The use of electric fields to control wave propagation speed by Schiff et al. [87] and its agreement with the firing rate model make a hopeful beginning.

CHAPTER 7

FUTURE DIRECTIONS

There are many biological and mathematical directions that may be pursued from this point. One can apply the techniques in this dissertation to many different neural network firing rate models. The effect of inhomogeneous inputs in these equations is important, considering that inputs are the primary mode of neural communication. Since the thalamus receives a multitude of inputs, a primary example is a firing rate model of thalamic tissue, which was recently developed by Coombes [18]. The excitatory-inhibitory network is, perhaps, the most natural subsequent model to study. One approach is to use the simplifications on the neuronal firing rates that were proposed by Pinto and Ermentrout [81] (described in Chapter 1), or instead one could assume different firing rates, not necessarily neglecting the inhibition-inhibition interactions. It would be interesting to examine the differences in existence and stability that local and nonlocal inhibition generate and how these differences are reflected by the firing rate functions.

Since nonlocal inhibition can support stable stationary pulses, one would assume that stationary pulses will also be stable for weak inputs. How then does the system behave for stronger inputs? Moreover, in the case of slow nonlocal inhibition, Pinto and Ermentrout [81] show that the stationary pulse loses stability via a subcritical Hopf bifurcation. We expect this case to be similar to the case of local inhibition, that strong inputs will generate stable pulses whereas weak inputs should give rise to breathers. In this case do breathers persist over a larger interval than in the excitatory case or does a similar secondary bifurcation occur? One primary difference between local and nonlocal inhibition is that nonlocal inhibition tends to preclude the existence of traveling waves. Thus if there is a secondary bifurcation similar to that for local inhibition, emitted traveling waves will either fail to propagate, in the case of weak inhibition or emission will not occur. Since the input still forces the system, breathers will still persist. However their breathings will be more irregular, as in Figure 4.8, without the emission of waves. This is the case in the excitatory model for parameter values for which the network does not

support natural waves. Furthermore, how does the tongue diagram in Figure 3.5 change when nonlocal inhibition is included? Another avenue to pursue is the existence of breathers in the case of smooth firing rates using numerical simulations. The results for the Heaviside function will serve as a guide for where breathers should exist. This will provide another aspect to compare and contrast the effects of different firing rates. Ultimately, it could prove interesting to study the Hopf bifurcation for smooth firing rates using singular perturbation theory.

As mentioned earlier, breathers may have an important application in the binding problem. Binding is the ability of neuronal populations to reconnect correlated sensory information, which has been fragmented into rudimentary components during the first stages of sensory processing. For example a solid object stimulates a group of neurons in the primary visual cortex, with each neuron responding to a small portion of the object. Interestingly, it has been found that neurons that are responding to the same stimulus exhibit the same modulation in their firing rates [41, 95]. Since visual inputs into the cortex are relatively weak, the network could operate in the regime where breathers exist. Consequently, breathers may interact with each other and synchronize their oscillations. Of course, a connected visual stimulus would create a connected region of input in the visual cortex. However, to approach this problem, we begin with two breathers, which are separated by some distance, and determine whether they synchronize. The relevant networks consist of excitatory and inhibitory neurons, so this would rely and build upon the analysis of the excitatory-inhibitory model. In experiments it is found that the largest fluctuation occurs near the maximal input. However, in the excitatory case, as well as the excitatory-inhibitory simulations of Wilson and Cowan [109], the largest fluctuation is near the steepest gradient of the input. This may be due to the fact that the activity u is not necessarily the same as the firing rate f(u). Although the Heaviside function cannot make the distinction, it may be clarified by the numerical simulations with smooth firing rates. The breather may operate in different regimes of the firing rate function; in particular the point of maximal modulation may depend on whether the breather is operating in the linear part or saturating part of the sigmoidal function.

One challenging problem is to decide how to represent the breather. Even with the Heaviside firing rate function, the breather is very difficult to compute exactly, and, if it were possible, it would be difficult to analyze the interactions between two such breathers. One can try to develop a phase-type model, treating the breathers, in some sense, as coupled oscillators. In any case, this is where the crux of the problem lies, and numerical simulations can always be performed with the possibility of gaining insight into how best to approach the

problem analytically.

Another problem would be to develop a more thorough analysis of the direction-selective model considered by Xie and Giese [111]. The model is a scalar equation with a Mexican hat weight function that is skewed off center to induce direction selectivity. Rather than supporting stationary pulses in the case of Amari [1], this system has the ability, if inhibition is not too strong, to produce natural traveling waves. In any case the system supports stable stimulus-locked pulses in some region in (v,\mathcal{I}) parameter space. When the velocity of the input is sufficiently varied from the center of this region, the pulse becomes unstable via a Hopf bifurcation, though Xie and Giese do not properly describe the behavior of the eigenvalues. In preliminary numerical simulations, we find that the bifurcation is subcritical, with a sharp transition to lurching waves. The wave has a pulse shape that periodically sweeps forth and pauses in a lurching fashion. Interestingly, when the strength of inhibition decreases, the lurching wave smoothly develops into a pulse-emitting solution, where intermediate solutions emit waves that fail to propagate after some distance. This indicates the effect of nonlocal inhibition and the relationship between lurching waves and pulse-emitters in this model. Moreover, there may be a connection to the lurching waves of thalamic tissue, which are associated with integrate-and-fire models [37, 38]. This connection may be studied by comparing the integrate-and-fire model with a corresponding firing rate model of thalamic tissue [18].

Directly related to this dissertation is the extension of the numerical simulations to polar grids for the Mexican hat network in Chapter 5. It is clear that the rectangular grid is playing some role in selecting modes with which it is commensurate. Moreover, while it seems reasonable that the odd modes may form the swimmer-like patterns, it also seems possible that the swimming motion is a result of favored propagation due to a combination of the grid and the odd number of lobes. The polar grid is more computationally expensive. However the results should clear up these fundamental questions.

APPENDIX A

PARAMETERS FOR THE BIOPHYSICAL MODEL

$$\begin{split} V_{\rm syn} &= -45 \; {\rm mV}, & g_{\rm syn} &= 20 \; {\rm mS/cm}^2, \\ V_{\rm K} &= -100 \; {\rm mV}, & g_{\rm K} &= 80 \; {\rm mS/cm}^2, \\ V_{\rm Na} &= 50 \; {\rm mV}, & g_{\rm Na} &= 100 \; {\rm mS/cm}^2, \\ V_{\rm L} &= -67 \; {\rm mV}, & g_{\rm L} &= 0.2 \; {\rm mS/cm}^2, \\ F &= 1 \mu {\rm F/cm}^2, & g_q &= 3 \; {\rm mS/cm}^2, \\ & \alpha_m(v) &= 0.32(54+v)/(1-\exp(-(v+54)/4)), \\ & \beta_m(v) &= 0.28(v+27)/(\exp((v+27)/5)-1), \\ & \alpha_h(v) &= 0.128 \exp(-(50+v)/18), \\ & \beta_h(v) &= 4/(1+\exp(-(v+27)/5)), \\ & \alpha_n(v) &= 0.032(v+52)/(1-\exp(-(v+52)/5)), \\ & \beta_n(v) &= 0.5 \exp(-(57+v)/40). \end{split}$$

where

$$p_{\infty}(v) = \frac{\alpha_p(v)}{\alpha_p(v) + \beta_p(v)}, \qquad \tau_p(v) = \frac{1}{\alpha_p(v) + \beta_p(v)}, \qquad p \in \{m, n, h\},$$

$$q_{\infty}(v) = \frac{1}{1 + e^{(-(v+35)/20)}}, \qquad \tau_q(v) = \frac{1000}{3.3e^{(v+35)/20} + e^{-(v+35)/20}}$$

$$\tau = 1, \qquad K(V) = \frac{1}{1 + e^{-(V+50)}},$$

APPENDIX B

AMARI'S ANALYSIS

B.1 Stationary Pulses with Nonlocal Inhibition

We describe the conditions of existence and stability of a stationary pulse in a simplified model considered by Amari [1] and comment on an additional stability result from Pinto and Ermentrout [81].

Recall the one-dimensional excitatory-inhibitory firing rate model

$$\tau_e \frac{\partial u_e}{\partial t} = -u_e + w_{ee} * F_{ee}(u_e) - w_{ei} * F_{ei}(u_i), \tag{B.1}$$

$$\tau_i \frac{\partial u_i}{\partial t} = -u_i + w_{ie} * F_{ie}(u_e) - w_{ii} * F_{ii}(u_i). \tag{B.2}$$

Pinto and Ermentrout arrive at Amari's case of lateral inhibition by the following assumptions. For simplicity, neglect the self-inhibition of the inhibitory population, or recurrent inhibition, i.e., $w_{ii}=0$. As the firing rate function has a sigmoidal shape, we take $F_{ee}(u)=F_{ie}(u)=H(u-\theta)$ where H is the Heaviside function and θ is a threshold for firing. This means a cell either fires at a constant rate or is quiescent, depending on the amount of synaptic current entering the cell. For the inhibitory population, however, there is experimental evidence suggesting that $F_{ie}(u)=u$ is a good approximation [81, 73]. Moreover, we assume that the synaptic strength is purely a function of distance, i.e. $w_{mn}(x,y)=w_{mn}(x-y)$, where the functions w_{mn} are bounded, nonnegative, even, continuous functions normalized such that $\int_{-\infty}^{+\infty}w_{mn}(z)dz=1$.

Under these assumptions, we consider the system in steady-state

$$U_e(x) = \int_{-\infty}^{\infty} w_{ee}(x-y)H(U_e(y)-\theta)dy - \int_{-\infty}^{\infty} w_{ei}(x-y)U_i(y)dy, \quad (B.3)$$

$$U_i(x) = \int_{-\infty}^{\infty} w_{ie}(x - y)H(U_e(y) - \theta)dy.$$
(B.4)

Substituting (B.4) into (B.3), we obtain

$$U_e(x) = \int_{-\infty}^{\infty} \left(w_{ee}(x-y) - \int_{-\infty}^{\infty} w_{ei}(x-z)w_{ie}(z-y)dz \right) H(U_e(y) - \theta)dy.$$
(B.5)

Let us define the object in parentheses as

$$w = w_{ee} - w_{ei} * w_{ie}. (B.6)$$

In most cases w is a $Mexican\ hat$ function the archetype of which is a difference of two Gaussian functions. This brings us to the scalar equation with a Mexican hat that Amari's [1] studied

$$\tau \frac{\partial u_e}{\partial t}(x,t) = -u_e(x,t) + \int_{\mathbb{R}} w(x-y)K(u_e(y,t) - \theta)dy,$$

which can be obtained from (B.2) by assuming that inhibition acts instantaneously. Amari considers the existence and stability (not shown) of a standing pulse, i.e., a function u_e , such that $U_e(x) > \theta$ on (a, b) and $U_e(x) < \theta$ otherwise, satisfying

$$U_e(x) = \int_{-\infty}^{\infty} w(x - y)H(U_e(y) - \theta)dy,$$
 (B.7)

where w is a smooth, integrable function with the following properties [1, 107]:

- 1. w(0) > 0, w'(0) = 0,
- 2. there exist z_m such that $w(z_m) < 0, \ w'(z_m) = 0,$ $w'(z) < 0 \ \text{for} \ z \in (0, z_m),$ (Mexican hat function) $w'(z) > 0 \ \text{for} \ z \in (z_m, \infty),$
- 3. $\lim_{x \to \infty} w(z) = 0$.

Under the above assumptions, Amari found four different classes of solutions characterized by their threshold properties: 0-solutions in which $u < \theta$ for all x, ∞ -solutions in which $u > \theta$ for all x, a-solutions in which the medium is above threshold only over an interval (-a, a), and (a, p)-solutions which are p-periodic solutions with an excited region of length a. It should be noted that, due to the translational invariance of the synaptic weight function, any a-solution can be shifted to be centered at the origin.

The following quantities determine the asymptotic behavior of the system:

$$W(x) = \int_0^x w(y)dy, \qquad w_p = \sum_{n=-\infty}^\infty w(x+np),$$
 (B.8)

$$W_m = \max_{x \in [0,\infty)} W(x), \tag{B.9}$$

$$W_{\infty} = \lim_{x \to \infty} W(x), \qquad W_p(x) = \int_0^x w_p(y) dy.$$
 (B.10)

The a-solutions satisfy $W(2a) - \theta = 0$ and are stable if and only if w(2a) < 0; the infinite family of periodic solutions (a, p) must satisfy $W_p(2a) - \theta = 0$ and are stable if and only if $w_p(2a) < 0$. Let $\{0, a_1, a_2, \infty\}$ denote the existence of the 0-solution, two different a-solutions, and the ∞ -solutions, respectively. The existence of solution types is listed for the following parameter regimes:

Spatially uniform solutions, whenever they exist, are stable. When a pair of a-solutions exist, the wider is stable and the narrower is unstable, whereas, a solitary a-solution is always unstable. In this latter case, the a-solution acts as a separatrix dividing the flow towards the 0-solution and the ∞ -solution: therefore, initial data lying above this unstable pulse will converge to a traveling pulse whose front and back propagate in opposite directions, leaving the

medium excited. In the case of a pair of a-solutions, inital data lying above the narrower, unstable pulse will converge to the wider, stable pulse [1, 23]. The stability was determined by analyzing the movement of the endpoints of the pulse and its dependence on the function W.

Pinto and Ermentrout [81] performed a linear stability analysis on the original system (B.1)-(B.2), linearizing about the stationary pulse solutions and examining the dependence of the resulting eigenvalues on the time constant of inhibition, $\tau = \frac{\tau_i}{\tau_c}$. The conditions for stability of the stationary pulse are

$$\frac{w(0) + w(2a)}{|w(0) - w(2a)|} < 1, \tag{Amari's condition} \tag{B.11}$$

$$\frac{w_{ee}(0) + w_{ee}(2a)}{w(0) - w(2a)} < \left(1 + \frac{1}{\tau}\right). \tag{B.12}$$

If the latter is not satisfied, stability is lost by a pair of complex eigenvalues crossing the imaginary axis. It was found numerically that the Hopf bifurcation appears to be subcritical without a sharp transition to periodic solutions.

B.2 Traveling Pulses with Local Inhibition

Amari also considered the following Wilson-Cowan type model, neglecting recurrent inhibition

$$\tau \frac{\partial u_e}{\partial t} = -u_e + w_{ee} * F_{ee}(u_e) - w_{ei} * F_{ei}(u_i), \tag{B.13}$$

$$\tau \frac{\partial u_i}{\partial t} = -u_i + \bar{w}_{ie} F_{ie}(u_e), \tag{B.14}$$

where w_{ee}, w_{ei} are bounded, positive, even, continuous functions decreasing on $(0, \infty)$, and \bar{w}_{ie} is a constant, representing local inhibition [1]. Notice that here excitatory neurons at x excite inhibitory neurons solely at the point x. Taking the firing rates to be Heaviside functions with thresholds, we obtain

$$\tau \frac{\partial u_e}{\partial t} = -u_e + w_{ee} * H_e(u_e) - w_{ei} * H_i(u_i), \tag{B.15}$$

$$\tau \frac{\partial u_i}{\partial t} = -u_i + \bar{w}_{ie} H_e(u_e), \tag{B.16}$$

where

$$H_e(u) = H(u - \theta_e)$$
 $H_i(u) = H(u - \theta_i).$

Assuming the excited region is (0, a) in the excitatory population and (b_1, b_2) in the inhibitory population, we seek traveling wave solutions $u_e(x, t) = U_e(x - ct)$ and $u_i(x, t) = U_i(x - ct)$ satisfying

$$-\tau c \frac{dU_e}{d\eta} = -U_e + w_{ee} * H_e(U_e) - w_{ei} * H_i(U_i),$$
 (B.17)

$$-\tau c \frac{dU_i}{dn} = -U_i + \bar{w}_{ie} H(U_e), \tag{B.18}$$

such that

$$\lim_{\eta \to \pm \infty} U_e(\eta) = 0, \qquad \lim_{\eta \to \pm \infty} U_i(\eta) = 0.$$

We can solve (B.18) independently to find the inhibitory activity pulse profile

$$U_{i}(\eta) = \begin{cases} 0, & a < \eta, \\ \bar{w}_{ie}(1 - e^{(\eta - a)/c\tau}), & 0 \le \eta \le a, \\ \bar{w}_{ie}(1 - e^{-a/c\tau})e^{\eta/c\tau}, & \eta \le 0, \end{cases}$$
(B.19)

thereby determining the values b_1, b_2 to be

$$b_1 = c\tau \ln \left(\frac{\theta_i}{(1 - e^{-a/\tau})\bar{w}_{ie}} \right), \tag{B.20}$$

$$b_2 = a + c\tau \ln \left(1 - \frac{\theta_i}{\bar{w}_{ie}} \right). \tag{B.21}$$

Applying the boundary conditions, the excitatory activity pulse profile is

$$U_e(\eta) = \frac{1}{c\tau} \int_{\eta}^{\infty} e^{\frac{\eta - \hat{\eta}}{c\tau}} \breve{W}(\eta) d\eta, \tag{B.22}$$

where

$$\check{W}(\eta) = \int_0^a w_{ee}(\eta - \hat{\eta})d\hat{\eta} - \int_{b_1}^{b_2} w_{ei}(\eta - \hat{\eta})d\hat{\eta}.$$

Since $u_e(0) = \theta_e$ and $u_e(a) = \theta_e$, the conditions for existence of a and c are

$$\int_{0}^{\infty} e^{\frac{\eta}{c\tau}} \breve{W}(\eta) d\eta = c\tau \theta_{e}, \tag{B.23}$$

$$\int_{0}^{\infty} e^{-\frac{\eta}{c\tau}} \breve{W}(\eta + a) d\eta = c\tau \theta_{e}. \tag{B.24}$$

On an interesting note, in this model with Heaviside firing rates, as well as the piecewise-constant Fitzhugh-Nagumo model [88], traveling waves exist without the need for a large difference in time constants of the two variables. However, the continuous versions of the same models require a substantial difference in time constants for the existance of traveling wave solutions, indicating that the piecewise constant models is a special case [88, 24].

REFERENCES

- [1] S. Amari, Dynamics of pattern formation in lateral inhibition type neural fields, Biol. Cybern., 27 (1977), pp. 77–87.
- [2] D. J. Amit and N. Brunel, Model of global spontaneous activity and local structured activity during delay periods in the cerebral cortex, Cerebral Cortex, 7 (1997), pp. 237–252.
- [3] M. Bode, Front-bifurcations in reaction-diffusion systems with inhomogeneous parameter distributions, Physica D, 106 (1997), pp. 270–286.
- [4] W. H. Bosking, Y. Zhang, B. Schofield, and D. Fitzpatrick, Orientation selectivity and the arrangement of horizontal connections in tree shrew striate cortex, J. Neurosci., 17 (1997), pp. 2112–2127.
- [5] P. C. Bressloff, Resonant-like synchronization and bursting in a model of pulse-coupled neurons with active dendrites, J. Comput.Neuro., 6 (1999), pp. 237–249.
- [6] —, Synaptically generated wave propagation in excitable neural media, Phys. Rev. Lett., 82 (1999), pp. 2979–82.
- [7] —, Traveling waves and pulses in a one-dimensional network of excitable integrate-and-fire neurons, J. Math. Biol., 40 (2000), pp. 169–198.
- [8] —, Traveling fronts and wave propagation failure in an inhomogeneous neural network, Physica D, 155 (2001), pp. 83–100.
- [9] ——, Mathematical Neuroscience Lecture Notes, unpublished, 2002.
- [10] ——, Spontaneous symmetry breaking in self-organized neural fields, Biological Cybernetics submitted, (2004).
- [11] P. C. Bressloff and S. E. Folias, Front bifurcations in an excitatory neural network, SIAM J Appl Math, 65 (2004), pp. 131–151.
- [12] P. C. Bressloff, S. E. Folias, A. Prat, and Y.-X. Li, Oscillatory waves in inhomogeneous neural media, Phys. Rev. Lett., 91 (2003), p. 178101.

- [13] J. CARR, Applications of Centre Manifold Theory, Springer-Verlag, New York, 1981.
- [14] F. S. Chance, Modelling cortical dynamics and the responses of neurons in the primary visual cortex, Ph.D. dissertation, Brandeis University., (2002).
- [15] R. D. CHERVIN, P. A. PIERCE, AND B. W. CONNORS, *Propagation of excitation in neural network models*, J. Neurophysiol., 60 (1988), pp. 1695–1713.
- [16] S. N. CHOW AND J. K. HALE, Methods of Bifurcation Theory, Springer-Verlag, Berlin, 1982.
- [17] B. W. Connors and Y. Amitai, Generation of epileptiform discharge by local circuits of neocortex, in Epilepsy: Models, Mechanisms, and Concepts, 78 (1993), pp. 388–423.
- [18] S. COOMBES, Waves and bumps in neuronal networks with axo-dendritic synaptic interactions, Physica D, 178 (2003), pp. 219–241.
- [19] S. COOMBES AND M. R. OWEN, Phys. Rev. Lett., 94 (2005), p. 148102.
- [20] F. CRICK, Function of the thalamic reticular complex; the searchlight hypothesis, Proc. Natl. Acad. Sci. USA, 81 (1984), pp. 4586–4590.
- [21] P. Dayan and L. F. Abbot, *Theoretical Neuroscience*, MIT Press, Cambridge, 2001.
- [22] A. Destexhe, Z. Mainen, and T. Sejnowski, Synthesis of models for excitable membranes, synaptic trasmission and neuromodulation using a common kinetic formalism, J. Comput. Neurosci, 1 (1994), pp. 195–231.
- [23] G. B. Ermentrout, The analysis of synaptically generated traveling waves, J. Comput. Neurosci., 5 (1998), pp. 191–208.
- [24] ——, Neural networks as spatial pattern forming systems., Rep. Prog. Phys., 61 (1998), pp. 353–430.
- [25] G. B. Ermentrout and D. Kleinfeld, Traveling electrical waves in cortex: Insights from phase dynamics and speculation on a computational role, Neuron, 29 (2001), pp. 33–44.
- [26] G. B. Ermentrout and J. B. McLeod, Existence and uniqueness of travelling waves for a neural network, Proc. Roy. Soc. Edin. A, 123 (1993), pp. 461–478.

- [27] J. W. Evans, Nerve axon equations: IV the stable and unstable impulse, Indiana Univ. Math. J., 24 (1975), pp. 1169–1190.
- [28] J. W. Evans and J. Feroe, Local stability theory of the nerve impulse, Math. Biosci., 37 (1977), pp. 23–50.
- [29] C. P. Fall, E. S. Marland, J. M. Wagner, and J. J. Tyson, Computation Cell Biology, Springer-Verlag, New York, 2002.
- [30] P. Fife, Mathematical Aspects of Reacting and Diffusing Systems, vol. 28 of Springer-Verlag Lecture Notes in Biomathematics, Springer-Verlag, Berlin, 1979.
- [31] P. C. FIFE AND J. B. McLeod, The approach of solutions of nonlinear diffusion equations to traveling front solutions, Arch. Rational Mech. Anal., 65 (1977), pp. 335–361.
- [32] S. E. Folias and P. C. Bressloff, *Breathers in two-dimensional neural media*, Phys. Rev. Lett. (submitted).
- [33] ——, Breathing pulses in an excitatory neural network, SIAM J. Appl. Dyn. Syst., 3 (2004), pp. 378–407.
- [34] ——, Stimulus-induced stationary and traveling breathers in an excitatory neural network, SIAM J. Appl. Math. to appear, (2005).
- [35] J. M. Fuster and G. Alexander, Neuron activity related to short term memory, Science, 173 (1971), p. 652.
- [36] D. GOLOMB AND Y. AMITAI., Propagating neuronal discharges in neocortical slices: Computational and experimental study, J. Neurophysiol., 78 (1997), pp. 1199–1211.
- [37] D. GOLOMB AND G. B. ERMENTROUT, Continuous and lurching traveling pulses in neuronal networks with delay and spatially decaying connectivity, PNAS, 96 (1999), pp. 13480–13485.
- [38] —, Effects of delay on the type and velocity of travelling pulses in neuronal networks with spatially decaying connectivity, Comput. Neural Syst., 11 (2000), pp. 221–246.
- [39] —, Bistability in pulse propagation in networks of excitatory and inhibitory populations, Phys. Rev. Lett., 86 (2001), pp. 4179–4182.

- [40] J. P. GOODRIDGE AND D. S. TOURETZKY, Modelling attractor deformation in the rodent head-direction system, J. Neurophysiol., 83 (2000), p. 3402.
- [41] C. M. Gray, Synchronous oscillations in neuronal systems: Mechanisms and functions, J. Comput. Neurosci., 1 (1992), pp. 11–38.
- [42] P. Grindrod, The Theory and Applications of Reaction-Diffusion Equations: Patterns and Waves, Oxford University Press, Cambridge, 1996.
- [43] A. HAGBERG AND E. MERON, Pattern formation in non-gradient reaction-diffusion systems: the effects of front bifurcations, Nonlinearity, 7 (1994), pp. 805–835.
- [44] A. Hagberg, E. Meron, I. Rubinstein, and B. Zaltzman, Controlling domain patterns far from equilibrium, Phys. Rev. Lett., 76 (1996), pp. 427–430.
- [45] B. D. HASSARD, N. D. KAZARINOFF, AND Y.-H. WAN, Theory and Applications of Hopf Bifurcation, Cambridge University Press, Cambridge, 1981.
- [46] M. Hirsch and S. Smale, Differential Equations, Dynamical Systems and Linear Algebra, Academic Press, New York, 1974.
- [47] A. L. Hodgkin and A. F. Huxley, A quatitative description of membrane current and its application to conduction and excitation in nerve, J. Physiol., 117 (1952), pp. 500–544.
- [48] M. H. HOLMES, Introduction to Perturbation Methods, Springer-Verlag, New York, 1995.
- [49] M. A. P. IDIART AND L. F. ABBOTT, Propagation of excitation in neural network models, Network, 4 (1993), pp. 285–294.
- [50] G. IOOSS AND D. D. JOSEPH, Elementary Stability and Bifurcation Theory, Springer-Verlag, New York, 1980.
- [51] D. JOHNSTON AND S. M. WU, Foundations of Cellular Neurophysiology, MIT Press, Cambridge, 1995.
- [52] C. K. R. T. Jones, Stability of the traveling wave solution of the FitzHugh-Nagumo system, Trans. Amer. Math. Soc., 286 (1984), pp. 431–469.

- [53] T. Kapitula, N. Kutz, and B. Sandstede, *The Evans function for nonlocal equations.*, Indiana University Mathematics Journal, (2003).
- [54] T. Kato, Perturbation Theory for Linear Operators, Springer-Verlag, Berlin, 1966.
- [55] J. P. KEENER, Waves in excitable media, SIAM J. App. Math., 39 (1980), pp. 538–548.
- [56] ——, Homogenization and propagation in the bistable equation., Physica D, 136 (2000), pp. 1–17.
- [57] ——, Principles of Applied Mathematics, Perseus Books, Cambridge, 2000.
- [58] —, Propagation of waves in an excitable medium with discrete release sites, SIAM J. Appl. Math., 61 (2000), pp. 317–334.
- [59] J. P. KEENER AND J. SNEYD, Mathematical Physiology, Springer-Verlag, New York, 1998.
- [60] D. KLEINFELD, K. R. DELANEY, M. S. FEE, J. A. FLORES, D. W. TANK, AND A. GALPERIN, Dynamics of propagating waves in the olfactory network of a terrestrial mollusk: an electrical and optical study., J. Neurophysiol., 72 (1994), pp. 1402–1419.
- [61] C. Koch and I. Segev, Methods in Neuronal Modeling: from Ions to Networks, MIT Press, Cambridge, 1998.
- [62] C. R. LAING AND W. C. TROY, *PDE methods for non-local models*, SIAM J. Dyn. Syst., 2 (2003), pp. 487–516.
- [63] ——, Two-bump solutions of Amari-type models of neuronal pattern formation, Physica D, 178 (2003), pp. 190–218.
- [64] C. R. LAING, W. C. TROY, B. GUTKIN, AND G. B. ERMENTROUT, Multiple bumps in a neuronal model of working memory, SIAM J. Applied Math., 63 (2002), pp. 62–97.
- [65] Y. W. LAM, L. B. COHEN, M. WACHOWIAK, AND M. R. ZOCHOWSKI, Odors elicit three different oscillations in the turtle olfactory bulb, J. Neurosci., 20 (2000), pp. 749–762.
- [66] Y.-X. Li, Tango waves in a bidomain model of fertilization calcium waves, Physica D, 186 (2003), pp. 27–49.

- [67] A. Longstaff, Neuroscience, Springer-Verlag, New York, 2000.
- [68] R. MAEX AND G. A. ORBAN, Model circuit of spiking neurons generating directional selectivity in simple cells, J. Neurophysiol., 75 (1996), pp. 1515–1545.
- [69] W. MAGNUS, F. OBERHETTINGER, AND R. P. SONI, Formulas and Theorems for the Special Functions of Mathematical Physics, Springer-Verlag, New York, 1966.
- [70] R. MALACH, M. H. Y. AMIR, AND A. GRINVALD, Relationship between intrinsic connections and functional architecture revealed by optical imaging and in vivo targeted biocytin injections in primate striate cortex, Proc. Natl. Acad. Sci., 90 (1993), pp. 10469–10473.
- [71] J. E. MARSDEN AND M. F. MCCRACKEN, the Hopf Bifurcation and its Applications, Springer-Verlag, London, 1976.
- [72] D. A. McCormick and T. Bal, Sleep and arousal: Thalamocirtical mechanisms, Annv. Rev. Neurosci., 20 (1997), pp. 185–215.
- [73] D. A. McCormick, B. W. Connors, J. W. Lighthall, and D. A. Prince, Comparative electrophysiology of pyramidal and sparsely spiny stellate neurons of the neocortex, J. Neurophysiol., 54 (1985), pp. 782–806.
- [74] M. MIKLAVCIC, Applied Functional Analysis and Partial Differential Equations, World Scientific, London, 1998.
- [75] E. K. MILLER, C. A. ERICKSON, AND R. DESIMONE, Neural mechanisms of visual working memory in prefrontal cortex of the macaque, J. Neuroscience, 16 (1996), pp. 5154–5167.
- [76] J. MILTON AND P. JUNG, ED., *Epilepsy as a Dynamic Disease*, Springer-Verlag, New York, 2003.
- [77] K. W. MORTON AND D. F. MAYERS, Numerical Solutions of Partial Differential Equations, Cambridge University Press, Cambridge, 1994.
- [78] A. W. NAYLOR AND G. R. SELL, Linear Operator Theory in Engineering Science, Holt, Rinehart, and Winston, New York, 1971.
- [79] M. A. L. NICOLELIS, L. A. BACCALA, R. C. S. LIN, AND J. K. CHAPIN, Sensorimotor encoding by synchronous neural ensemble activity at multiple levels of the somatosensory system, Science, 268 (1995), pp. 1353-1358.

- [80] D. Pinto and G. B. Ermentrout, Spatially structured activity in synaptically coupled neuronal networks: I. traveling fronts and pulses, SIAM J. Appl. Math, 62 (2001), pp. 206–225.
- [81] —, Spatially structured activity in synaptically coupled neuronal networks: II. lateral inhibition and standing pulses, SIAM J. Appl. Math, 62 (2001), pp. 226–243.
- [82] D. Pinto, S. L. Patrick, W. C. Huang, and B. W. Connors, *The fine structure of epileptiform activity in neocortex in vitro*, submitted, (2004).
- [83] —, Mechanisms of inititation, propagation, and termination of epileptiform activity in neocortex in vitro, submitted, (2004).
- [84] A. Prat and Y.-X. Li, Stability of front solutions in inhomogeneous media, Physica D, 186 (2003), pp. 50–68.
- [85] J. C. PRECHTL, L. B. COHEN, B. PASARAM, P. P. MITRA, AND D. KLEINFELD, Visual stimuli induce waves of electrical activity in turtle cortex, Proc. Natl. Acad. Sci. USA, 94 (1997), pp. 7621–7626.
- [86] A. D. REDISH, A. N. ELGA, AND D. S. TOURETZKY, A coupled attractor model of the rodent head direction system, Network, 7 (1996), pp. 671–685.
- [87] K. A. RICHARDSON, S. J. SCHIFF, AND B. J. GLUCKMAN, Control of traveling waves in the mammalian cortex, Phys. Rev. Lett., 94 (2005), p. 028103.
- [88] J. RINZEL AND J. B. KELLER, Traveling wave solutions of a nerve conducting equation, Biophysical J., 13 (1973), pp. 1212–37.
- [89] J. RINZEL AND D. TERMAN, Propagation phenomena in a bistable reaction-diffusion system, SIAM J. Appl. Math, 42 (1982), pp. 1111–1137.
- [90] P. R. ROELFSEMA, A. K. ENGEL, P. KONIG, AND W. SINGER, Visuomotor integration is associated with zero time-lag synchronization among cortical areas, Nature, 385 (1997), pp. 157–161.
- [91] J. E. Rubin, Stability, bifurcations and edge oscillations in standing pulse solutions to an inhomogeneous reaction-diffusion system, Proc. Roy. Soc. Edinburgh A, 129 (1999), pp. 1033–1079.

- [92] J. E. Rubin and W. C. Troy, Sustained spatial patterns of activity in neuronal populations with or without lateral inhibition, SIAM J. Appl. Math, (2004).
- [93] P. Schutz, M. Bode, and H. G. Purwins, Bifurcations of front dynamics in a reaction-diffusion system with spatial inhomogeneities, Physica D, 82 (1995), pp. 382–397.
- [94] P. E. Sharp, H. T. Blair, and J. Cho, The anatomical and computational basis of the rat head-direction cell signal, Trends in Neurosci., 24 (2001), pp. 289–297.
- [95] W. Singer, Neural synchrony: A versatile code for the definition of relations?, Neuron, 24 (1999), pp. 49–65.
- [96] H. Spors and A. Grinvald, Spatio-temporal dynamics of odor representations in the mammalian olfactory bulb, Neuron, 34 (2002), pp. 301–315.
- [97] M. Steriade, The Intact and Sliced Brain, MIT Press, Cambridge, 2001.
- [98] H. Suarez, C. Koch, and R. Douglas, Modeling direction selectivity of simple cells in striate visual cortex within the framework of the canonical microcircuit, J. Neurosci., 15 (1995), p. 6700.
- [99] J. S. Taube and J. P. Bassett, Persistent neural activity in head direction cells, Cerebral Cortex, 13 (2003), pp. 1162–1172.
- [100] J. S. Taube, R. U. Muller, and J. B. Ranck Jr., Head direction cells recorded from the postsubiculum in freely moving rats: Effects of environmental manipulations, J. Neurosci., 10 (1990), pp. 436–447.
- [101] J. G. TAYLOR, Neural 'bubble' dynamics in two dimensions: Foundations, Biol. Cybernetics, 80 (1999), pp. 303–409.
- [102] E. C. TITCHMARSH, Introduction to the Theory of Fourier Integrals, Oxford University Press, London, 1959.
- [103] F. G. TRICOMI, Integral Equations, vol. 5 of Pure and Applied Texts in Mathematics, Interscience Publishers, New York, 1967.
- [104] J. J. Tyson and J. P. Keener, Singular perturbation theory of traveling waves in excitable media: A review, Physica D, 32 (1988), pp. 327–361.

- [105] X.-J. WANG AND J. RINZEL, Alternating and synchronous rhythms in reciprocally inhibitory model neurons, Neural Computation, 4 (1992), pp. 84–97.
- [106] G. N. Watson, A Treatise on the Theory of Bessel Functions, Cambridge University Press, Cambridge, 1952.
- [107] H. WERNER AND T. RICHTER, Circular stationary solutions in twodimensional neural fields, Biol. Cybernetics, 85 (2001), pp. 211–217.
- [108] H. R. WILSON AND J. D. COWAN, Excitatory and inhibitory interactions in localized populations of model neurons, Biophysical Journal, 12 (1972), pp. 1–24.
- [109] —, A mathematical theory of the functional dynamics of cortical and thalamic nervous tissue, Kybernetik, 13 (1973), pp. 55–80.
- [110] J. Wu, L. Guan, and Y. Tsau, Propagating activation during oscillations and evoked responses in neocortical slices, J. Neurosci., 19 (1999), pp. 5005-5015.
- [111] X. XIE AND M. GIESE, Nonlinear dynamics of direction-selective recurrent neural media, Phys. Rev. E, 65 (2002), p. 051904.
- [112] X. XIE, R. H. R. HAHNLOSER, AND H. S. SEUNG, Double-ring network model of the head-direction system, Phys. Rev. E, 66 (2002), p. 041902.
- [113] T. Yoshioka, G. G. Blasdel, J. B. Levitt, and J. S. Lund, Relation between patterns of intrinsic lateral connectivity, ocular dominance, and cytochrome oxidase-reactive regions in macaque monkey striate cortex, Cerebral Cortex, 6 (1996), pp. 297–310.
- [114] K. Yosida, Functional Analysis, Springer-Verlag, Berlin, 1980.
- [115] K. Zhang, Representation of spatial organization by the intrinsic dynamics of the head-direction cell ensemble: A theory, J. Neurosci., 16 (1996), pp. 2112–2126.
- [116] L. Zhang, On stability of traveling wave solutions in synaptically coupled neuronal networks, Diff. and Int. Eq., 16 (2003), pp. 513–536.
- [117] L. Zhang, Existence, uniqueness, and exponential stability of traveling wave solutions of some integral differential equations arising from neuronal networks, J. Diff. Eqn., 197 (2004), pp. 162–196.